Laser guide stars and turbulence profiling for extremely large telescopes

Timothy Butterley

Laser Guide Stars and Turbulence Profiling for Extremely Large Telescopes

Timothy Butterley

A thesis presented for the degree of

Doctor of Philosophy

Centre for Advanced Instrumentation

Department of Physics

University of Durham

England

December 2006

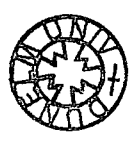

Laser Guide Stars and Turbulence Profiling for Extremely Large Telescopes

Timothy Butterley

Submitted for the degree of Doctor of Philosophy
December 2006

Abstract

The next generation of ground based telescopes, the so-called extremely large telescopes, will offer a significant leap in sensitivity and resolution compared to current telescopes. They also present a range of technical challenges. This thesis presents work on two important problems in implementing laser guide star adaptive optics on extremely large telescopes: focal anisoplanatism and turbulence profiling.

The SPLASH (Sky-Projected Laser Array Shack-Hartmann) laser guide star wavefront sensing technique is described. The technique is shown to offer reduced focal anisoplanatism compared to a conventional laser guide star for large telescopes. The technique may also offer advantages for larger apertures, including extremely large telescopes, but simulations were limited to 8 metre apertures by currently available computing capabilities.

A calibration method is presented for the SLODAR (Slope Detection and Ranging) turbulence profiling technique, along with an analysis of the effects of scintillation on SLODAR when the technique is applied on a small ($\sim$ 40 cm diameter) telescope.

A new variation on the SLODAR technique, SLOTDAR (Slope Detection and Ranging through a slot), is introduced, in which the spatial sampling can be optimised based on the brightness of the available reference stars.

Declaration

The work in this thesis is based on research carried out at the Centre for Advanced Instrumentation, the Department of Physics, the University of Durham, United Kingdom. No part of this thesis has been submitted elsewhere for any other degree or qualification and it is all my own work unless referenced to the contrary in the text.

Parts of this work have been published in the following:

Butterley, T., Love, G. D., Wilson, R. W., Myers, R. M., and Morris, T. J. (2006). A Shack-Hartmann wavefront sensor projected onto the sky with reduced focal anisoplanatism. *Mon. Not. R. Astron. Soc.*, 368:837–843.

Butterley, T., Wilson, R. W., and Sarazin, M. (2006). Determination of the profile of atmospheric optical turbulence strength from SLODAR data. *Mon. Not. R. Astron. Soc.*, 369:835–845.

Acknowledgments

First of all I'd like to sincerely thank my supervisors, Gordon Love and Richard Wilson, for guiding me through my PhD. Gordon has taught me to take a step back from time to time to think about the bigger picture, and encouraged me to explore unconventional approaches to solving problems. Thanks to Richard for being so generous with his time, for his seemingly endless patience and for arranging so many opportunities to visit observatories.

I would like to acknowledge financial support from the UK Particle Physics and Astronomy Research Council.

To my office-mates: Tim, Chris, Paul, Jason, Mark and James; thanks for many useful discussions and for providing suitable distractions when work was a little slow. Thanks also to Nigel, Nirmal, Ali, Francois, Gary and anyone else in the CfAI who lent a helping hand at any point. Thanks in particular to Richard M for getting me interested in adaptive optics in the first place.

To my housemates: Ciaran, Dave, Nic and Derek; thanks for putting up with me, for joining me in eating curry more frequently than strictly necessary, and for making sure I didn't work too hard. Thanks to the other members of Pedestrian Island, and all the musicians I've played with at the Durham sessions, for helping to keep me sane over the last three years.

Finally, I'd like to thank my parents and my brother for much support and encouragement over the years.

Contents

List of Figures

Acronyms

AO	adaptive optics
CCD	charge-coupled device
CTIO	Cerro Tololo Inter-American Observatory
DIMM	differential image motion monitor
DM	deformable mirror
ELT	extremely large telescope
EMCCD	electron multiplication charge-coupled device (see also L3CCD)
ESO	European Southern Observatory
FA	focal anisoplanatism
FFT	fast Fourier transform
FSM	fast steering mirror
GLAO	ground layer adaptive optics
GSM	generalized seeing monitor
L3CCD	low light level charge-coupled device (see also EMCCD)
LGS	laser guide star
LTAO	laser tomography adaptive optics
MAD	Multi-conjugate Adaptive Optics Demonstrator
MASS	multi-aperture scintillation sensor
MCAO	multi-conjugate adaptive optics
MOAO	multi-object adaptive optics
NGS	natural guide star
PSD	power spectral density
PSF	point spread function
SCIDAR	scintillation detection and ranging

SH	Shack-Hartmann
SLODAR	slope detection and ranging
SLOTDAR	slope detection and ranging through a slot
SOR	successive over-relaxation
SPLASH	sky-projected laser array Shack-Hartmann
SSS	single star SCIDAR
SVD	singular value decomposition
WFS	wavefront sensor
WHT	William Herschel Telescope

Chapter 1

Introduction

Ground based astronomy is a constantly developing field. Each generation of telescopes is larger than the last and this trend is set to continue, for now at least. The current generation of ground based telescopes have primary mirrors which are 8-10 metres in diameter. With the aid of adaptive optics to overcome image distortions due to atmospheric turbulence, these are allowing astronomers to observe fainter objects, and at higher resolution, than ever before.

However, even the most sophisticated adaptive optics systems currently operating are unable to reach the limit of resolution of 8 m class telescopes at visible wavelengths. In particular, high order correction over a wide field of view is an extremely difficult problem that can only be addressed by tomographic techniques such as multi-conjugate adaptive optics. Successful implementation of such techniques is reliant on a detailed knowledge of the distribution of atmospheric turbulence in altitude.

The next generation of ground based telescopes, the so-called "extremely large telescopes" (ELTs), represent a significant gain in resolution and sensitivity. They also represent a tremendous step in the technical difficulties involved in their construction. Aside from the obvious difficulties in the mechanical engineering of the support structures and the fabrication of the optical surfaces, adaptive optics on

such large apertures presents a huge challenge. High order adaptive optics on such a telescope will almost certainly involve multiple laser guide stars (LGSs) and, as yet, an effective LGS scheme for an ELT has yet to be designed.

Applying LGSs on an ELT scale presents a range of problems, of which one of the greatest is focal anisoplanatism (or the "cone effect") which renders a single LGS on an ELT effectively useless. Multiple LGSs can be used to compensate for focal anisoplanatism but the number and configuration of LGSs required depends on the type of adaptive optics correction desired and on the distribution of atmospheric turbulence with altitude. Perspective elongation of LGSs is also a much more severe problem on an ELT than on current telescopes, although several methods of compensating for this effect are under investigation. The necessity for multiple lasers introduces the problem of beam "fratricide", in which the light being imaged from one LGS is contaminated by stray light from other lasers. The optical design of an ELT will not be well-suited to focusing at relatively short distances so a wavefront sensor for a LGS at finite range must be able to cope with severe static aberrations.

ELTs present a further problem in that the secondary mirror will be at a higher altitude than a significant fraction of the ground layer of turbulence. As a result, a significant amount of turbulence may be present within the telescope itself, so the optical path may be aberrated by the same volume of turbulence two or three times. The magnitude of this problem can only be assessed with a detailed characterisation of the surface layer of turbulence which, currently, is not available.

Due to the high cost of building an ELT, only three ELTs are currently planned worldwide. The first is the European Southern Observatory's (ESO's) "European Extremely Large Telescope" (E-ELT). Formerly the "Overwhelmingly Large Telescope" (OWL), it was originally planned to be 100 metres in diameter but has recently been scaled down to $\sim$ 30-60 m. The second is the Thirty-Meter Telescope (TMT), formerly the California Extremely Large Telescope (CELT). The third is the Giant Magellan Telescope (GMT) which will consist of seven circular 8.4 m di-

ameter segments and have a resolving power equivalent to a 24.5 m telescope. Site testing campaigns are currently underway to identify suitable locations for all three telescopes.

This thesis attempts to address two of the main problems associated with deploying LGS adaptive optics on ELTs – focal anisoplanatism and detailed turbulence profiling. An analysis is presented of an alternative method of LGS wavefront sensing in which the effect of focal anisoplanatism is much reduced compared to conventional LGS wavefront sensing. A detailed calibration is presented of a technique for measuring the vertical profile of turbulence which is ideal both for supporting the design of multi-conjugate adaptive optics systems and for providing detailed measurements of the ground layer of turbulence. A new variation on this technique is also presented, in which the spatial resolution can be optimised based on the available light level and which allows the heights of individual turbulent layers to be measured more precisely.

1.1 Thesis synopsis

In the next two chapters I provide a background to my work. Chapter 2 covers the phenomenon of atmospheric turbulence, the mathematics used to describe it and several experimental methods of characterising it. In chapter 3 I describe the key components and operation of an astronomical adaptive optics system, including LGSs, and summarise some of the main types of adaptive optics system.

In chapter 4 I present a detailed analysis of SPLASH, a new LGS wavefront sensing technique which suffers less from focal anisoplanatism than a conventional LGS. The technique is suitable for current large (8 m class) telescopes and could potentially be suitable for use on an ELT.

In chapter 5 I present a method of calibrating the SLODAR turbulence profiling technique and an analysis of the effect of scintillation on SLODAR when the

technique is used on a small telescope.

In chapter 6 I present a new variation on the SLODAR technique, "SLOTDAR", in which the spatial resolution can be optimised (without reconfiguration of the optics) depending on the brightness of the target stars.

The final chapter, chapter 7, contains my conclusions.

Chapter 2

Atmospheric turbulence

In this chapter I briefly summarise the relevant theory relating to the effects of atmospheric turbulence on ground-based astronomical imaging and describe several methods of sensing turbulence.

2.1 Seeing

The fundamental resolution limit of an imaging telescope is the diffraction limit, defined by the angle (e.g. Hecht, 2002)

$$\theta_d = 1.22\frac{\lambda}{D} \tag{2.1}$$

where λ is the wavelength of the light, D is the diameter of the telescope aperture and θ_d is defined as the angular radius of the first dark ring in the Airy disk (see figure 2.1, first panel). Objects with an angular separation smaller than θ_d cannot be clearly resolved. In practice, ground-based telescopes with aperture diameters larger than a few inches are not diffraction limited due to the effects of atmospheric turbulence.

Atmospheric turbulence occurs as a result of mixing of air of different temperatures. Temperature variations result in air density variations, which in turn result

Figure 2.1: Example telescope PSFs. *Left*: diffraction limited, no aberrations (Airy disk); *centre*: large aperture, short exposure – note the "speckles"; *right*: large aperture, long exposure – speckles are averaged out. All 3 PSFs have the same image scale but the brightnesses are scaled independently. The aberrated PSFs were simulated with $D/r_0 = 10$ (see section 2.2 for definition of r_0).

in variations in the refractive index of air. Light passing through the atmosphere is aberrated by these refractive index fluctuations. When a star is imaged through the atmosphere by a telescope, the focused image is distorted as a result of the aberrations in the incoming wavefront. For a small aperture the aberrations are dominated by angle-of-arrival (tip/tilt) fluctations, resulting in motion of the instantaneous image without the point spread function (PSF) being significantly distorted. A long exposure will result in a significantly larger, blurred, image. For a larger aperture, phase fluctuations on smaller spatial scales also have a significant effect, resulting in the instantaneous image being broken up into sub-images known as "speckles" (figure 2.1, second panel). These speckles average out in a long exposure image, but the resulting PSF can be many times the width of the unaberrated PSF (figure 2.1, third panel). The phenomenon of telescope images being degraded by turbulence is known as "seeing". The seeing angle (i.e. the resolution limit due to seeing) typically varies between $\sim 0.5''$ and $\sim 2''$ at astronomical sites.

2.2 Kolmogorov turbulence

The most commonly used model for atmospheric turbulence was proposed by Kolmogorov (1941) and developed by Tatarski (1961). The results are summarised by, for example, Goodman (1985), Hardy (1998) and Dainty (2000), and are reproduced briefly here. The Kolmogorov model is a general model for turbulence in a fluid medium, in which it is assumed that energy is added to the medium in the form of large spatial scale disturbances which then break down into smaller and smaller structures as a result of turbulent flow. In the case of atmospheric turbulence, the large-scale source of energy is solar heating of the Earth's surface.

The model describes the behaviour of turbulence on spatial scales in the "inertial subrange" between the "outer scale", L_0, and the "inner scale", l_0. The outer scale is the largest spatial scale of the turbulence on which energy is introduced into the system. The inner scale is the length scale on which energy is dissipated as heat by viscous friction.

Refractive index fluctuations can be described by a structure function of the form

$$D_n(\Delta x) = \langle [n(\mathbf{x}) - n(\mathbf{x}')]^2 \rangle \tag{2.2}$$

where $n(\mathbf{x})$ and $n(\mathbf{x}')$ are the refractive index at points $\mathbf{x}$ and $\mathbf{x}'$ respectively (in three dimensional space), $\Delta x = |\mathbf{x} - \mathbf{x}'|$, and the triangular brackets represent an ensemble average over a large number of points. The refractive index structure function for Kolmogorov turbulence is

$$D_n(\Delta x) = C_n^2(h)\Delta x^{2/3} \qquad l_0 < \Delta x < L_0 \tag{2.3}$$

where $C_n^2(h)$ is the "refractive index structure constant", which represents the strength of atmospheric turbulence as a function of altitude, h.

The corresponding power spectral density (PSD) of the refractive index fluctua-

tions (within the inertial subrange) is

$$\Phi_n(\xi) = 0.033 C_n^2(h) \xi^{-11/3} \tag{2.4}$$

where $\xi = 2\pi/\Delta x$.

Rather than describing the effects of turbulence in terms of refractive index fluctuations $n(\mathbf{x})$, it is often more useful to consider the optical phase fluctuations $\phi(\mathbf{r})$ (where $\mathbf{r}$ is a two dimensional vector). The phase PSD and spatial structure function for Kolmogorov turbulence are

$$\Phi_\phi(\kappa) = \frac{0.023\kappa^{-11/3}}{r_0^{5/3}} \tag{2.5}$$

and

$$\begin{aligned} D_\phi(\mathbf{r}) &= 2.91 k^2 (\cos\gamma)^{-1} |\mathbf{r}|^{5/3} \int_0^\infty C_n^2(h) \mathrm{d}h \\ &= 6.88 \left(\frac{|\mathbf{r}|}{r_0}\right)^{\frac{5}{3}} \end{aligned} \tag{2.6}$$

where $\kappa = 2\pi/|\mathbf{r}|$, $k = 2\pi/\lambda$, γ is the zenith angle and r_0 is the Fried parameter (Fried, 1965). The Fried parameter describes the total strength of the atmospheric turbulence and is given by

$$r_0 = \left(\frac{2.91}{6.88} k^2 (\cos\gamma)^{-1} \int_0^\infty \mathrm{d}h C_n^2(h)\right)^{-\frac{3}{5}}. \tag{2.7}$$

It can be seen from this equation that r_0 varies with wavelength as $\lambda^{6/5}$. Thus a value of r_0 is defined for one particular wavelength – typically 500 nm is used. The value of r_0 at 500 nm typically ranges between ~ 5 cm for strong daytime turbulence and > 20 cm at night for an astronomical site with good seeing. Physically, r_0 can be interpreted as the size of an aperture with a diffraction limit equal to the limit

of resolution due to seeing, so the resolution limit for a given r_0 is (cf. equation 2.1)

$$\theta_{seeing} \sim \frac{\lambda}{r_0}. \tag{2.8}$$

An alternative physical interpretation is that r_0 defines an aperture size for which the mean square wavefront error is ~ 1 rad^2. The piston-subtracted phase variance due to atmospheric turbulence across a cirular aperture of diameter D is given by (Noll, 1976)

$$\sigma_\phi^2 = 1.0299(D/r_0)^{5/3}. \tag{2.9}$$

Although not explicitly used in this thesis, two other parameters that are often used to describe the seeing conditions are the isoplanatic angle, θ_0, and the coherence time, τ_0. The isoplanatic angle is, broadly speaking, an angle defining an area of sky from within which all incoming light has approximately the same phase aberration, and is given by

$$\theta_0 = 0.314(\cos\gamma)\frac{r_0}{\langle H\rangle} \tag{2.10}$$

where $\langle H\rangle$ is the "effective turbulence height" – a weighted average of the turbulence height, given by

$$\langle H\rangle = \left(\frac{\int \mathrm{d}h C_n^2(h) h^{5/3}}{\int \mathrm{d}h C_n^2(h)}\right)^{3/5}. \tag{2.11}$$

The coherence time is defined as the time after which the mean square phase excursion is 1 rad^2, and is given by

$$\tau_0 = 0.314(\cos\gamma)\frac{r_0}{\langle V\rangle} \tag{2.12}$$

where $\langle V\rangle$ is the effective wind speed and is given by

$$\langle V\rangle = \left(\frac{\int \mathrm{d}h C_n^2(h) v(h)^{5/3}}{\int \mathrm{d}h C_n^2(h)}\right)^{3/5}. \tag{2.13}$$

where $v(h)$ is the wind velocity as a function of altitude. Thus τ_0 depends on the

strength and translation velocity of the turbulence.

2.3 Non-Kolmogorov turbulence

While the Kolmogorov turbulence model is conveniently simple, it is often necessary to consider problems in which the relevant length scales are not constrained to the inertial subrange. In particular, the outer scale of turbulence, L_0, has been measured to be of the order of several metres or several tens of metres, i.e. of the same order as the aperture size of large astronomical telescopes. Assuming Kolmogorov turbulence to be valid up to these length scales would therefore be inappropriate. The von Karman power spectrum is a commonly-used modification of the Kolmogorov spectrum (with the same underlying power law) in which the outer scale is included by attenuating low spatial frequencies (von Kármàn, 1948). The PSD for the von Karman spectrum is

$$\Phi_\phi(\kappa) = 0.022883 r_0^{-5/3} \frac{L_0^{11/3}}{(1 + L_0^2\kappa^2)^{11/6}}. \tag{2.14}$$

The corresponding form for the spatial structure function of the phase is (Jenkins, 1998)

$$D_\phi(r) = 0.17253 \left(\frac{L_0}{r_0}\right)^{5/3} \left[1 - \frac{2\pi^{5/6}}{\Gamma(5/6)} \left(\frac{r}{L_0}\right)^{5/6} K_{5/6}\left(2\pi\frac{r}{L_0}\right)\right] \tag{2.15}$$

where K is a modified Bessel function of the second kind. Another variation of this spectrum, called the modified von Karman spectrum, includes the effects of the inner scale in addition to the outer scale. Inner scale effects are important when considering turbulence-induced intensity variations (known as scintillation – see section 2.4.3). The work in this thesis is concerned primarily with the effects of turbulence on phase, for which the outer scale is far more important than the inner scale, so the modified von Karman spectrum is not used.

Another alternative to the Kolmogorov model (which is less commonly used) is the generalized phase power spectrum devised by Nicholls et al. (1995). Unlike the von Karman model, the generalized power spectrum does *not* assume the same underlying power law as the Kolmogorov model. The PSD is given by

$$\Phi_\phi(\kappa) = \frac{A_\beta \kappa^{-\beta}}{\rho_0^{\beta-2}} \qquad (2 < \beta < 4), \tag{2.16}$$

where β is the power law exponent (11/3 in the case of Kolmogorov turbulence), ρ_0 is equivalent to r_0 and the constant A_β is chosen such that the piston-subtracted wavefront variance over a pupil diameter $D = \rho_0$ is equal to 1 rad^2. This differs from the Kolmogorov definition by about 3%, so the generalized power spectrum does not reduce exactly to the Kolmogorov form in the case where $\beta = 11/3$. The value of A_β is given by (Boreman and Dainty, 1996)

$$A_\beta = \frac{2^{\beta-2}[\Gamma(\frac{\beta+2}{2})]^2 \Gamma(\frac{\beta+4}{2}) \Gamma(\frac{\beta}{2}) \sin(\pi \frac{\beta-2}{2})}{\pi^\beta \Gamma(\beta+1)}. \tag{2.17}$$

The corresponding form for the phase structure function is:

$$D_\phi(r) = \gamma_\beta \left(\frac{r}{\rho_0}\right)^{\beta-2} \tag{2.18}$$

where γ_β is a constant that keeps consistency between the power spectrum and the structure function, given by (Rao et al., 2000):

$$\gamma_\beta = \frac{2^{\beta-1}[\Gamma(\frac{\beta+2}{2})]^2 \Gamma(\frac{\beta+4}{2})}{\Gamma(\frac{\beta}{2}) \Gamma(\beta+1)}. \tag{2.19}$$

2.4 Measuring $C_n^2(h)$

Measuring the strength of atmospheric turbulence, whether as a function of altitude or the total integrated C_n^2, is important for a number of reasons. The first is in site testing; when building a new telescope it is obviously desirable (amongst other

considerations e.g. weather, light pollution) to choose a site where there is as little atmospheric turbulence as possible (Schöck et al., 2003; Lawrence et al., 2004).

The second is in predicting the performance of proposed new AO systems. It is important that a new instrument should be able to fulfil its science goals without being unnecessarily expensive due to being over-specified. In the particular case of multi-conjugate AO systems (see section 3.3.2), $C_n^2(h)$ profiles are essential for optimising the conjugate altitudes of the deformable mirrors (Le Louarn et al., 2000). The wind velocity as a function of altitude is also important (for all types of AO), as this determines the frequency at which an AO system must update in order to provide adequate wavefront correction.

The third reason for $C_n^2(h)$ profiling is to support an observatory in its operation. Site monitoring instruments which continuously measure the seeing allow informed decisions to be made about appropriate science observations. Science targets can be chosen based on the predicted performance of AO systems in the current conditions in order to make optimal use of telescope time. In addition, the turbulence profile can be of use to astronomers, when analysing data collected with adaptive optics, as the profile at the time of an observation can be used to estimate the corrected PSF as a function of position in the field (Fusco et al., 2000; Wilson et al., 2003).

Below is a summary of some of the main techniques used for measuring atmospheric turbulence.

2.4.1 Balloon measurements

One of the longest-standing methods for measuring atmospheric turbulence is using microthermal sensors mounted on meteorological balloons (Vernin and Muñoz-Tuñón, 1992, 1994). The balloon is released and ascends to an altitude of $\sim$ 25 km, measuring temperature variations as a function of altitude. Thus, rather than measuring C_n^2 directly, this technique measures the temperature structure parameter C_T^2. C_n^2 is proportional to C_T^2 but depends also on temperature and pressure.

Balloon measurements are an effective method for site testing but this method is clearly unsuitable for long-term site monitoring. It should be noted, however, that microthermal sensors can be permanently installed on a mast to measure very low altitude turbulence at a site.

2.4.2 Differential Image Motion Monitor (DIMM)

The differential image motion monitor (DIMM) is an instrument used both for testing new potential observatory sites and as a site monitor at operating observatories (e.g. Sarazin and Roddier, 1990). The technique was first proposed by Stock and Keller (1960) and has more recently been refined by Tokovinin (2002). The instrument is typically implemented on a small telescope ($D \sim 25$ cm) and operated robotically. The telescope pupil is covered by a mask containing two subapertures, and the differential motion of two images of a single star, formed through the two subapertures, is measured. Differential image motion is used because image motion common to the two subapertures must be subtracted to remove the (significant) effects of telescope shake.

By assuming the Kolmogorov model of turbulence, the differentical image motion data can be used to derive the Fried parameter, r_0. DIMM only measures the total turbulence strength – it does not provide information about the strength of turbulence as a function of altitude.

2.4.3 Scintillation Detection and Ranging (SCIDAR)

"Scintillation" refers to the development of intensity variations (sometimes referred to as "shadow patterns") in the optical field as aberrated light continues to propagate. The degree to which the light entering the pupil of a telescope is scintillated depends on the strength and altitude of the atmospheric turbulence – if the turbulence is higher or stronger there will be more scintillation. The amount of scintillation in the optical field is measured by the scintillation index, defined as (e.g. Beran

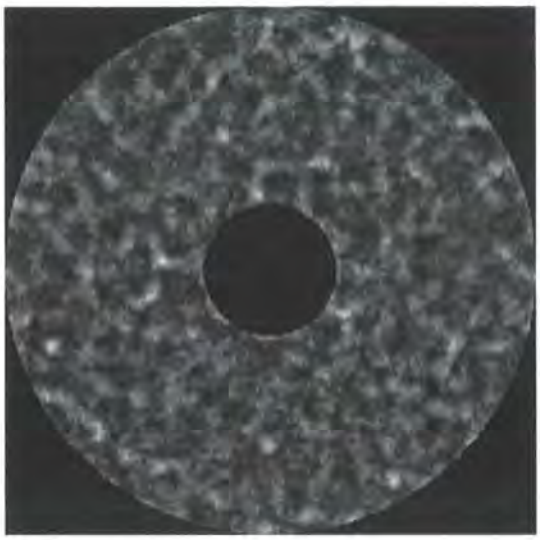

Figure 2.2: Simulated intensity fluctuations in a telescope pupil due to scintillation (scintillation index = 0.2).

and Whitman, 1988)

$$\sigma_I^2 = \frac{< I^2 > - < I >^2}{< I >^2} \tag{2.20}$$

where the brackets represent an ensemble average over realizations of the turbulent field and I is the intensity in any realization. An example of a scintillated pupil image is shown in figure 2.2.

Scintillation detection and ranging (SCIDAR) (Azouit et al., 1978) is a technique in which scintillation is used to triangulate the altitude of turbulence using a binary star. Images of the telescope pupil are autocorrelated, and both $C_n^2(h)$ and the velocities of turbulent layers can be retrieved from the autocorrelation data. This technique is typically applied on relatively large telescopes (1 m in diameter or larger), and has been very successfully used for site characterisation (e.g. Vernin and Muñoz-Tuñón, 1994). The main weakness of "classical SCIDAR" is that it is insensitive to turbulence close to the ground.

This drawback was addressed by the development of "generalized SCIDAR", in which the detector is conjugated to an altitude below (or above) the telescope pupil, thus providing a longer propagation distance for scintillation due to low layer turbulence to develop (Fuchs et al., 1998; Klückers et al., 1998). Generalized SCIDAR

allows $C_n^2(h)$ to be measured for the whole atmosphere.

A more recent development of SCIDAR is Single Star SCIDAR (SSS) (Garnier et al., 2005) which aims to address the issue of the limited number of binary targets in the sky. $C_n^2(h)$ is still retrieved from the autocorrelation of the pupil scintillation pattern, but this is measured at multiple conjugate altitudes in order to better constrain the problem. Unlike classical or generalized SCIDAR, SSS can be applied on a small telescope.

Another variation on SCIDAR, LOLAS (low layer SCIDAR), has been proposed by Avila and Chun (2004) for measuring low layer turbulence using a small aperture (eg. 40 cm) telescope and a relatively wide (3 arcminute) binary star.

2.4.4 Multiple Aperture Scintillation Sensor (MASS)

The multiple aperture scintillation sensor (MASS) (Tokovinin, 1998) is a low resolution but low cost turbulence profiler. It uses a small (14 cm, unobscured) telescope observing a single star to measure scintillation through a series of concentric annular apertures, with a circular central aperture. For each aperture the incident intensity is measured and the scintillation index is calculated. Differential scintillation indices between apertures are also calculated. The turbulence profile can then be retrieved with relatively coarse resolution, e.g. 6 altitude points for 4 apertures.

As with SCIDAR, if the apertures are conjugated to the telescope pupil then MASS is insensitive to low altitude turbulence. By conjugating some of the apertures to a non-zero altitude the complete profile can be obtained, but saturation of the scintillation can become a problem. Alternatively, a MASS instrument can readily be combined with a DIMM into a hybrid (MASS-DIMM) instrument that is a versatile site monitor. By differencing the total C_n^2 measured by MASS and DIMM, the strength of the ground layer can be estimated.

2.4.5 Slope Detection and Ranging (SLODAR)

The slope detection and ranging (SLODAR) technique was proposed and demonstrated by Wilson (2002), although similar techniques were suggested prior to this by Welsh (1992) and Bally et al. (1996). The SLODAR technique involves the measurement of $C_n^2(h)$ via triangulation, by observing a binary star using a Shack-Hartmann wavefront sensor. Further information about SLODAR is not included here as the technique will be described in some detail in chapter 5.

2.4.6 Sonic Detection and Ranging (SODAR)

Doppler sonic detection and ranging (SODAR) is an acoustic radar technique that is used to measure turbulence in the lower atmosphere. Doppler SODAR is used in several areas outside astronomy (e.g. to detect turbulence at airports). A review of different kinds of SODAR can be found in e.g. Crescenti (1997). A SODAR instrument consists of a phased array of transducers which is used to transmit sonic pulses into the atmosphere and then receive echoes reflected by thermal inhomogeneities in the air. Like techniques based on microthermal probes, SODAR measures C_T^2 rather than C_n^2. Calibration of SODAR to retrieve C_T^2 (and thus C_n^2) accurately is difficult but some success has been achieved (Travouillon, 2006).

2.5 Measuring the outer scale

As mentioned in section 2.3, the outer scale of turbulence, L_0, has been measured to be of a similar order of magnitude to the aperture size of a large astronomical telescope. As a result, less image motion (i.e. angle-of-arrival or tip/tilt variance) is observed in the image plane of such a telescope than is predicted by the Kolmogorov model, although additional image motion can be introduced by telescope shake. In the case of an ELT (where possibly $D > L_0$) this effect will extend to higher spatial frequencies and less wavefront variance will be observed in other low-order modes

than would be expected in the Kolmogorov case (Winker, 1991). Thus a good knowledge of the outer scale is important for designing adaptive optics systems for large telescopes.

One method for measuring the outer scale is via direct sensing of the wavefront on different length scales and fitting a model to the observations. This method is used by the generalized seeing monitor (GSM) (Martin et al., 1998; Ziad et al., 2004), which essentially consists of several separately mounted 10 cm telescopes pointing at the same star, which each measure the local wavefront gradient. A similar effect is achieved by deploying a Shack-Hartmann wavefront sensor on a large telescope (St-Jacques et al., 1997; Wilson et al., 1999).

Other methods for measuring L_0 include balloon measurements, as mentioned in section 2.4.1, (Abahamid et al., 2004a,b) and interferometric techniques (Maire et al., 2006).

It is difficult to determine L_0 with great precision because most methods have a maximum baseline that is smaller than L_0. A wavefront sensor on a telescope so large that $D >> L_0$ would be able to measure the outer scale much more precisely.

Chapter 3

Adaptive optics

In this chapter I describe the basic components and operation of an astronomical adaptive optics system, including laser guide stars, and briefly introduce some of the different types of adaptive optics system.

3.1 Components of an adaptive optics system

An adaptive optics (AO) system typically consists of at least one each of a wavefront sensor (WFS), a wavefront corrector and a reconstructor (figure 3.1). The purpose of each of these components is described below. Examples of specific types are given, but these are by no means exhaustive.

3.1.1 Wavefront sensor

A WFS collects light from a reference source and measures it in such a way as to allow the shape of the wavefront to be determined. The wavefront aberrations are continuously measured at a sufficiently rapid rate to allow wavefront correction to be applied in real time. In astronomy, the reference source can be either a real star, usually referred to as a natural guide star (NGS), or an artificially-created laser guide star (LGS).

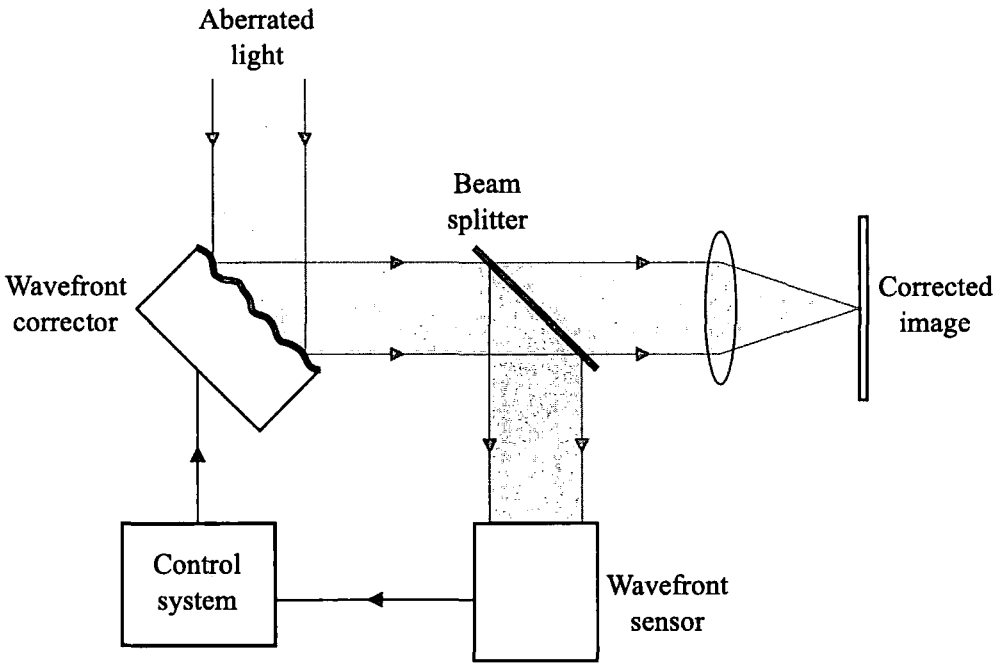

Figure 3.1: Overview of an adaptive optics system.

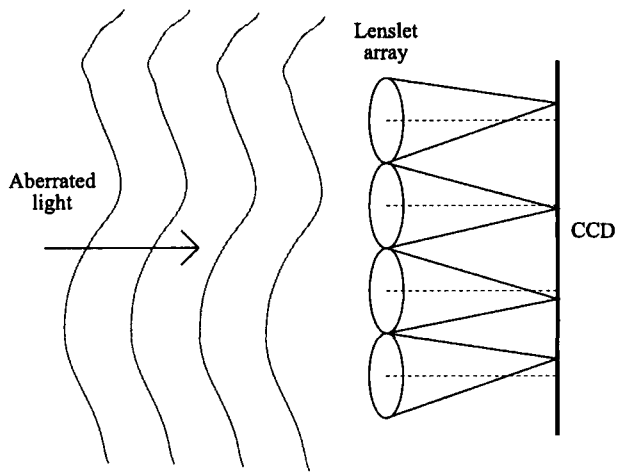

Figure 3.2: A Shack-Hartmann wavefront sensor. The telescope pupil is separated into "subapertures" by a lenslet array which images the light into an array of spots. The spots are displaced according to the local wavefront slope.

The most common type of WFS, and the one of most relevance here, is the Shack-Hartmann (SH) WFS (figure 3.2). In a SH WFS the telescope pupil is divided into an array of smaller subapertures and the light from each subaperture is focused through a lenslet (a small lens). The resulting array of spots is imaged using a CCD camera. As the overall wavefront gradient across a subaperture varies, the position of the corresponding spot changes. The spot positions are measured using a centroid (centre of gravity) algorithm. The displacements of the spots are a measure of the wavefront gradient at each point in the SH array.

3.1.2 Wavefront corrector

The purpose of a wavefront corrector is to alter the shape of a wavefront in order to remove aberrations. Most astronomical AO systems separate global tip/tilt (angle-of-arrival) correction from higher-order correction. Tip/tilt corrections are made using a "fast steering mirror" (FSM) – a flat mirror that can be tilted in the x and y directions to compensate for image motion.

Higher order aberrations are corrected using a deformable mirror (DM), of which there are several different types. Two of the types most commonly used in astronomical AO are described below. Other types of wavefront correctors exist, such as liquid crystal devices, but these are not currently used in astronomical AO.

Segmented deformable mirror

A segmented DM, as its name suggests, is a mirror made up of many smaller flat mirror segments. Each segment is mounted on one or more "actuators" which allow the segment to be moved. Depending on the mirror, each mirror segment can be moved in one, two or three degrees of freedom: (i) piston only, (ii) tip and tilt, or (iii) piston, tip and tilt. Segmented DMs with three degrees of freedom provide the closest approximation to a smooth wavefront shape.

The NAOMI AO system on the 4.2 metre William Herschel Telescope uses a seg-

mented DM with 76 square segments, each capable of piston, tip and tilt correction (Benn et al., 2004).

Facesheet deformable mirror

A facesheet DM is a continuous mirror made of a thin sheet of material (or a composite of different materials). Piston actuators of some form are attached to the back of the facesheet, allowing the overall shape of the sheet to be altered. Examples include those made by Xinetics Inc.[1]

The DM in the Altair AO system on the 8 metre Gemini North telescope is a facesheet DM with 177 actuators (Herriot et al., 1998).

3.1.3 Wavefront reconstruction and AO control

AO systems generally make use of "closed loop" control systems. The WFS comes *after* the wavefront corrector in the optical path of the light, so the sensed aberration is the residual error after the wavefront has been corrected. This means the reconstruction problem can be assumed to be linear.

Normally the reconstruction of a wavefront from the WFS signals and the subsequent determination of the control signals required for the corrective element(s) to compensate are combined into a single operation. This is described by the matrix operation

$$\mathbf{x} = \mathbf{M}\mathbf{s} \tag{3.1}$$

where $\mathbf{s}$ is the vector of WFS measurements, $\mathbf{x}$ is the vector of DM control signals and $\mathbf{M}$ is the "control matrix". The simplest method of generating a control matrix, for an SH WFS and a facesheet DM, is from a "poke matrix", $\mathbf{B}$, which satisfies the equation

$$\mathbf{s} = \mathbf{B}\mathbf{x}. \tag{3.2}$$

[1]Xinetics Inc., 115 Jackson Road, Devens, MA 01432, USA.

The poke matrix is constructed by "poking" each of the DM's actuators in turn, in the absence of turbulence (i.e. using a calibration light source), and assembling the resulting WFS centroid vectors into a matrix. The most basic control matrix is simply the least squares inverse (or pseudo-inverse) of the poke matrix,

$$\mathbf{M} = (\mathbf{B}^T\mathbf{B})^{-1}\mathbf{B}^T. \tag{3.3}$$

In practice a reconstruction matrix of this form is usually calculated via a singular value decomposition (SVD) of the poke matrix. The poke matrix is "decomposed" into system eigenmodes and eigenvectors. Typically there will be a number of poorly sensed modes which have a detrimental effect on system performance, so these modes can be "conditioned" out of the matrix by setting the corresponding eigenvalues to zero.

There are other, more sophisticated, control algorithms such as the *maximum a posteriori* (MAP) algorithm (e.g. Roggeman and Welsh, 1996; Le Louarn, 2002). This algorithm still uses a linear reconstruction operation (equation 3.1) but the control matrix incorporates information about wavefront sensor noise and turbulence statistics to achieve better reconstruction.

3.2 Laser guide stars

Laser guide stars (LGSs) were proposed (in non-military AO) by Foy and Labeyrie (1985) as a means of increasing the sky coverage of adaptive optics systems, and also of increasing the number of photons available for wavefront sensing. The basic principle is that a laser beam is projected into the sky, usually from a separate "launch" telescope, to form a bright beacon close to the science target. There are two different types of LGS – Rayleigh and sodium.

A Rayleigh LGS is so-called because it depends on the Rayleigh scattering mechanism (scattering of photons by molecules – air molecules in this case). The laser

is focused at a point in the atmosphere above the telescope, typically at an altitude of 10–20 km, and the backscattered photons are collected by the telescope and fed into the WFS. Some form of range gating is necessary to ensure only photons backscattered from a range of altitudes close to the focus altitude are seen by the WFS, meaning that Rayleigh lasers need to be pulsed. Due to the drop-off in laser power with altitude, beacon heights of greater than $\sim$ 20 km are impractical.

A sodium LGS takes advantage of a $\sim$ 10 km thick layer of sodium ions in the atmosphere at an altitude of $\sim$ 90 km. A laser beam with a wavelength of 589 nm is directed into the atmosphere and causes excitation of these ions, resulting in bright re-emission. The high altitude of a sodium LGS means it suffers less from focal anisoplanatism (see section 3.2.2) than a Rayleigh LGS and the finite thickness of the sodium layer removes the need for range gating, so a continuous wave (CW) laser can be used instead of a pulsed laser. However, Rayleigh backscatter from low altitudes still needs to be controlled – for example, by launching the laser from behind the secondary mirror so that the mirror obscures most of the Rayleigh plume.

3.2.1 Tip/tilt correction

An LGS does not provide a useful measurement of the global tip/tilt aberration. As the laser beam passes upwards through the atmosphere it picks up a tip/tilt error, resulting in an uncertainty in the position of the beacon on the sky. A second tip/tilt error is then picked up as the light is scattered back down through the atmosphere, so the WFS imaging the LGS measures the combined upwards and downwards tip/tilt errors. Schemes for compensating for this effect have been suggested (e.g. McCullough et al., 1992) but generally an LGS AO system still requires at least one NGS for tip/tilt correction. However, tip/tilt can be measured using a low order WFS (i.e. with fewer, larger subapertures) or even the full telescope aperture, so the NGS light level requirement for tip/tilt correction is much lower than for full AO correction. Thus the improvement in sky coverage given by the use of LGSs is

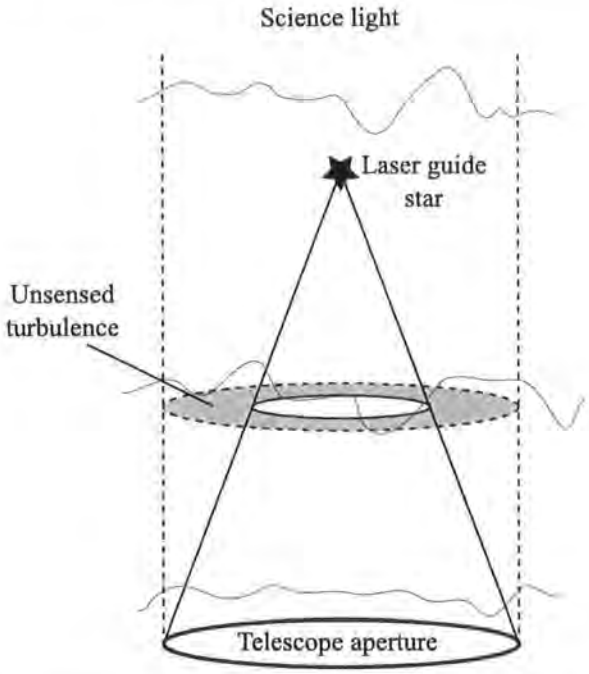

Figure 3.3: Focal anisoplanatism – the light from a laser guide star (solid lines) samples a cone of turbulence whereas light from the science target (dashed lines) samples a cylinder.

still tremendous.

3.2.2 Focal anisoplanatism

The most notable limitation of the LGS is focal anisoplanatism (FA) or the "cone effect" (Parenti and Sasiela, 1994), as shown in figure 3.3. The volume of atmosphere sampled by the light from an LGS differs from that sampled by an NGS – an NGS samples a cylinder (because the light is essentially plane by the time it reaches the Earth) whereas an LGS samples a cone, because the light is diverging from a point at finite range. The severity of FA depends on the altitude of the laser beacon, the turbulence profile and the size of the telescope aperture – lower beacon altitude, higher altitude turbulence and larger telescope sizes all result in more severe FA.

3.2.3 Perspective elongation

Another limitation of LGSs is perspective elongation. Ideally a laser beacon would be a point source but in reality it is an extended column of light in the atmosphere. When observed from a point some distance from the laser launch axis, the beacon is visibly elongated. Thus, if the laser is launched from behind the secondary mirror of the telescope, the WFS images for subapertures close to the edge of the telescope tend to appear elongated. Spot elongation is a problem which increases in severity with the diameter of the telescope, and is worse for lower altitude beacons. Sodium beacons, being at a much higher altitude, suffer considerably less from spot elongation than Rayleigh beacons. However, the aperture of an ELT would be large enough that perspective elongation would be a problem even for a sodium beacon.

The simplest approach to limiting spot elongation is simply to use a shorter range gate, although this results in a corresponding reduction in the backscattered light, meaning either that the laser power must be increased or the beacon altitude lowered. A more sophisticated solution is dynamic refocusing – a fast-moving mirror can be used to track each laser pulse as it travels through the atmosphere (Angel, 2001; Baranec et al., 2005). Alternatively, Ribak and Ragazzoni (2004) have proposed a method of reducing laser spot elongation by launching multiple weak beams from around the outside of the telescope aperture. These beams all focus and combine at the same height making a single beacon that suffers less from elongation then a beacon formed by a single beam.

3.2.4 Novel LGS designs

A number of alternatives to "conventional" LGS wavefront sensing have been suggested. One such alternative is the shearing interferometer, demonstrated by Sandler et al. (1994), in which light collected from the LGS is split with a beam splitter and recombined with a shear, producing interference fringes from which the wavefront can be reconstructed. A variation on this technique, involving a parallel laser launch

from the primary mirror of the telescope, is under consideration by ESO as a possible method for ELTs (Bonaccini Calia et al., 2004).

Baharav et al. (1994, 1996) proposed the creation of a fringe pattern in the atmosphere which would be analysed by an SH WFS.

Buscher et al. (2002) proposed a technique called P^4 (Projected Pupil Plane Patterns) in a which a laser beam is expanded to fill the telescope pupil and then projected from the primary mirror as a parallel beam. The wavefront becomes aberrated on the upward path and intensity variations develop as the beam propagates. The cross-section of the beam is imaged at different altitudes and the wavefront aberration reconstructed from the evolution of the intensity distribution.

Love et al. (2004) proposed SPLASH (Sky-Projected Laser Array Shack-Hartmann) which is described in detail in chapter 4. As with P^4, SPLASH senses the atmosphere on the upward path of the laser light.

Kellner et al. (2004a,b) proposed "pseudo-inverse guide stars" (PIGS), an alternative method of LGS wavefront in which the LGS is treated as from a source at infinite distance, thus overcoming some of the difficulties of using a reference source at finite range.

3.3 More complex AO systems

A "classical" NGS AO system consists of a single WFS and a separate tip/tilt mirror and DM. An LGS AO system necessitates a second WFS (albeit a low-order one) to measure tip/tilt from an NGS while higher order aberrations are measured by the LGS WFS. More sophisticated configurations have been proposed to provide better performance, involving multiple WFSs and DMs. Two such configurations are described below, although others exist such as laser tomography AO (LTAO), in which single conjugate correction is applied using multiple LGSs to overcome focal anisoplanatism, and multi-object AO (MOAO), in which several DMs are used to

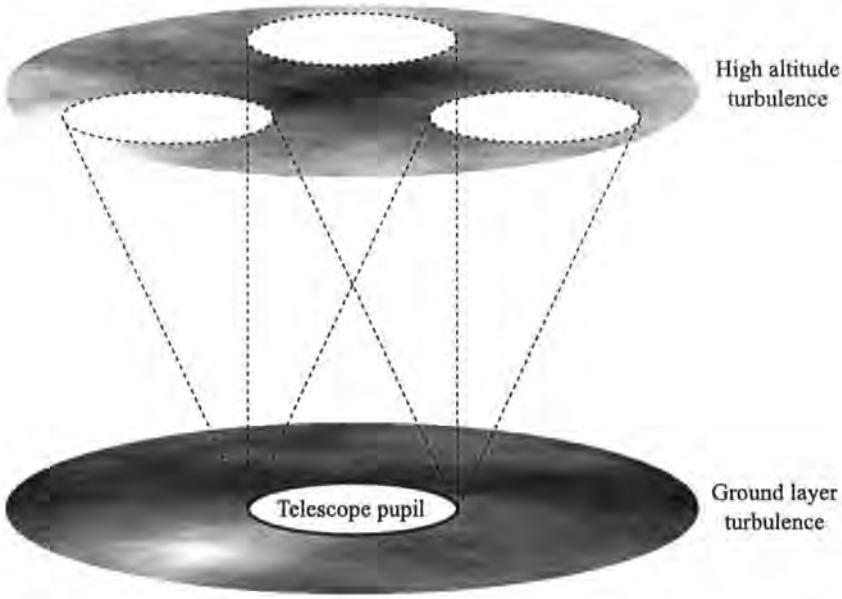

Figure 3.4: Guide star configuration for ground layer adaptive optics. Light from the guide stars samples the same aberration close to the ground but different aberrations at high altitude. The WFS measurements for the guide stars are averaged resulting in correction that is weighted towards the ground.

simultaneously correct several separate narrow fields of view.

3.3.1 Ground layer adaptive optics

One of the simplest variations on a classical AO system is a ground layer AO (GLAO) system (e.g. Rigaut, 2002; Tokovinin, 2004). Such a system is designed to sense and correct only the lowest layer of atmospheric turbulence. This gives poorer on-axis performance than a classical system, but results in a significantly larger corrected field of view.

There are several ways in which a GLAO system can be implemented. The simplest is to use a number (4 or 5) of NGSs scattered around the edges of the science field, and observe each with a separate WFS. The light from the guide stars passes through the same turbulence very close to the ground, but each star samples different high altitude turbulence (see figure 3.4). The signals from the WFSs are averaged (either before or after reconstruction) resulting in the high-layer turbulence averaging out but the common, ground layer, signal being preserved.

An obvious progression is to replace the NGSs with a constellation of LGSs – a multiple-LGS GLAO system is proposed for one of the GEMINI telescopes (Szeto et al., 2006; Andersen et al., 2006). As in the classical AO case, this solves the problem of needing suitable guide stars and allows the stars to be positioned in any arrangement desired. At least one NGS is still required for tip/tilt correction, however. A variation on the constellation of LGSs has been proposed in which a single LGS is scanned rapidly in a circle around the field of view once each WFS integration (Morris and Myers, 2006).

3.3.2 Multi-conjugate adaptive optics

A more complicated development of classical AO is multi-conjugate AO (MCAO) (Beckers, 1988; Tallon et al., 1992), in which multiple DMs are used as well as multiple guide stars and WFSs. Rather than measuring the wavefront error in a single direction, it is measured in multiple directions (using multiple LGSs or NGSs) and is then reconstructed in three dimensions – the altitudes as well as the shapes of the optical aberrations are measured. The DMs are conjugated to different altitudes, and an aberration at a given altitude is corrected with the most appropriately-conjugated DM (see figure 3.5).

MCAO compensates for angular anisoplanatism and thus offers high order correction (considerably higher than GLAO) over a wide field of view. LGS-based MCAO systems can at least partially overcome FA because the LGSs can be positioned so as to "overlap" up to some altitude, thus sampling the areas of turbulence not measured by a single-LGS AO system.

While offering better performance than a GLAO system, wavefront reconstruction in an MCAO system is a difficult problem and the performance of such a system depends crucially on the C_n^2 profile and the conjugation of the DMs. The inability of LGSs to correctly sense tip/tilt presents an additional problem for MCAO in that, when relying on multiple LGSs to reconstruct the turbulence at multiple altitudes,

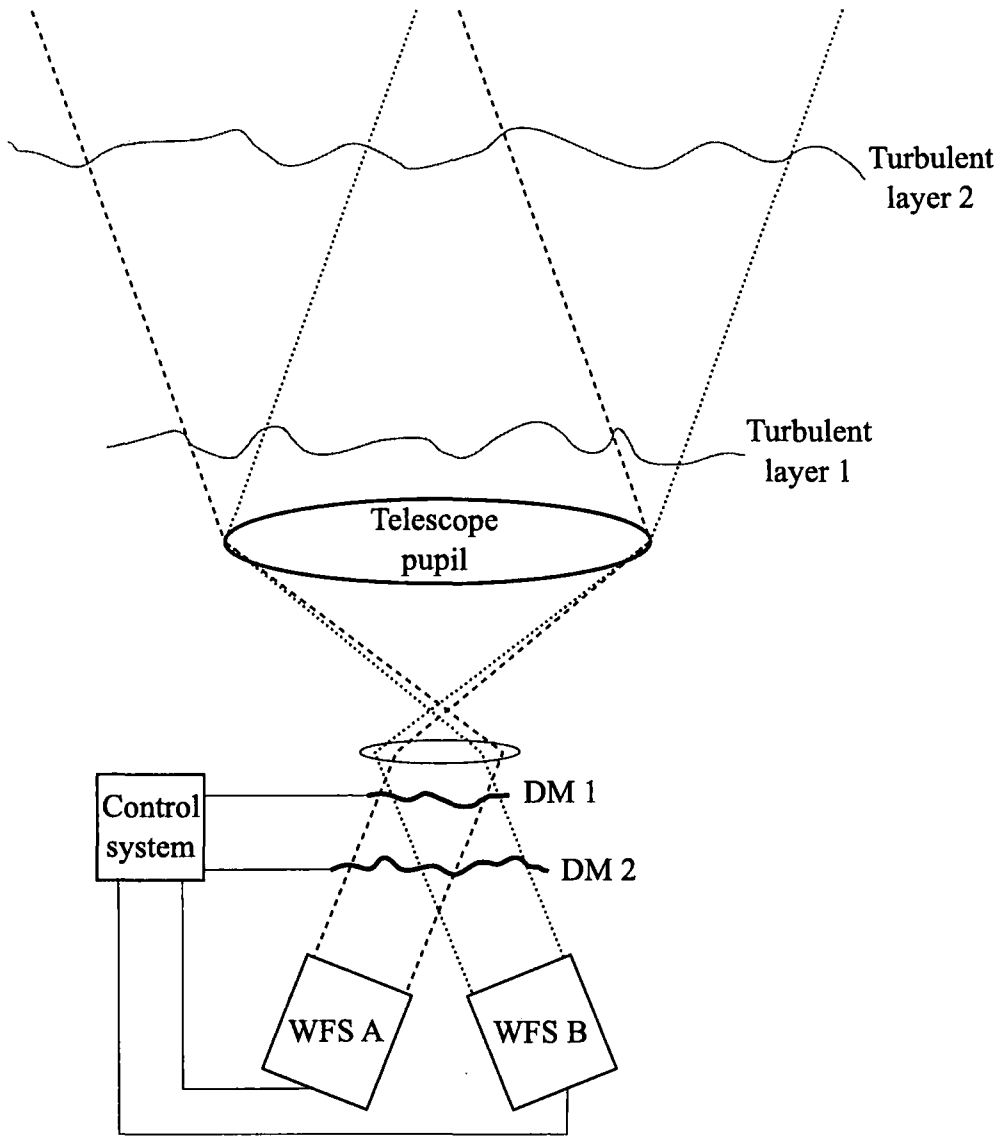

Figure 3.5: Overview of a multi-conjugate adaptive optics system. Two WFSs observe two guide stars (broken lines and dotted lines). Aberrations at different altitudes are seen with different shifts by the two WFSs. Wavefront correction is applied by two DMs conjugated to different altitudes.

the conjugate altitude of some modes such as focus can not be correctly determined. It is therefore necessary to measure more than just tip/tilt from NGSs.

No facility MCAO systems are currently operational on astronomical telescopes, but ESO's Multi-conjugate Adaptive Optics Demonstrator (MAD) (Marchetti et al., 2003, 2004) has been extensively lab-tested and will be tested on-sky on the VLT, Paranal, in the coming months. A facility MCAO system is due to be installed at Gemini South within the next year[2].

[2]http://www.gemini.edu/sciops/instruments/adaptiveOptics/MCAO.html

Chapter 4

Laser guide star wavefront sensing with reduced focal anisoplanatism

In this chapter I examine a new LGS technique, SPLASH (Sky-Projected Laser Array Shack-Hartmann), proposed as a solution to FA (the "cone effect") and, by theory and simulation, compare the performance of this technique to that of a conventional LGS AO system. Most of this work has been published in Butterley et al. (2006a).

The basic concept of SPLASH was first presented in Love et al. (2004), but has much in common with Tscherning aberrometry – a technique used in ophthalmology to measure optical aberrations in the human eye. This was first described by Tscherning (1894) and has become more widely adopted in recent years (e.g. Mrochen et al., 2001). Here I present results of a theoretical analysis and a closed-loop numerical simulation to validate the SPLASH technique. Section 4.1 outlines the concept and describe the advantages and problems associated with the technique. I present a theoretical analysis and its results in section 4.2, and a description of my numerical model and its results in section 4.3. In section 4.4 I summarise my results and outline the remaining problems not yet addressed.

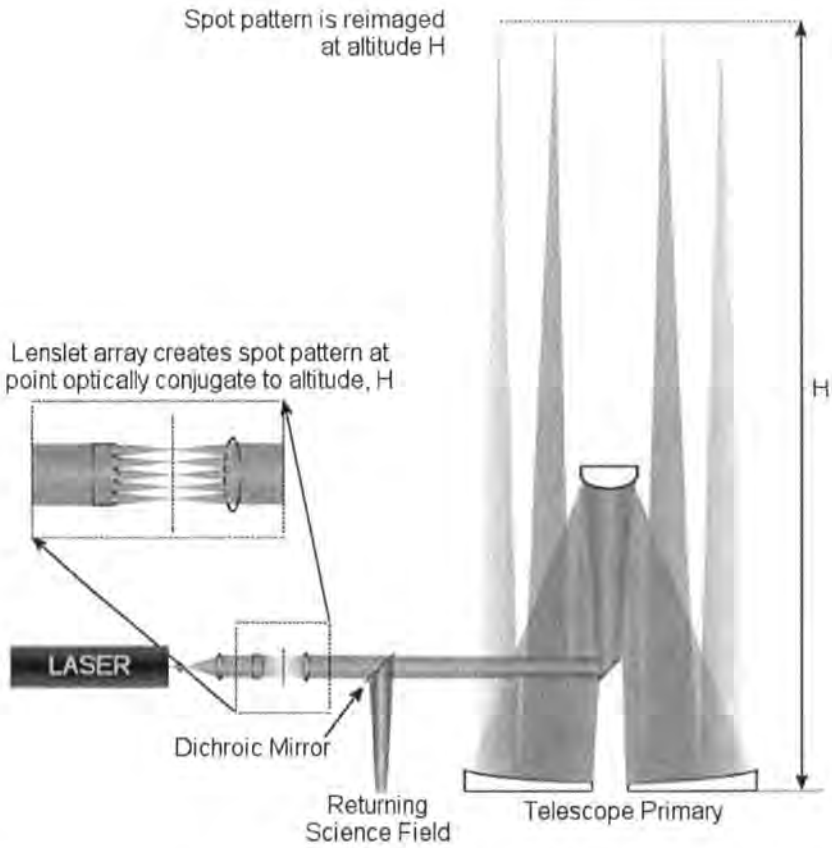

Figure 4.1: Concept of SPLASH, showing the upward passage of the beams. A possible optical implementation is shown whereby the laser is launched via a lenslet array. This is only a conceptual diagram and not a formal optical design – practical implementation may require a rather different approach for reasons discussed in the main text. The size of each of the converging beams is $\sim r_0$ although only four are shown here for clarity. Furthermore, the beams are shown as converging to a point, whereas in reality they would be broadened by diffraction. See text for more discussion. *Diagram by T.J. Morris.*

4.1 Description of SPLASH

This section describes the key principles of the SPLASH technique of wavefront sensing and outlines the advantages and disadvantages associated with the technique.

4.1.1 SPLASH concept

SPLASH wavefront sensing is a pseudo-inverse of conventional LGS/Shack-Hartmann wavefront sensing in which the atmosphere is sensed on the upward path of the laser

beam instead of the return path. The basic premise, illustrated in figure 4.1, is to project an array of converging laser beams, each of size $\sim r_0$ (where r_0 is the Fried parameter), from the primary mirror of the telescope to form an array of spots on the sky. The position of each spot on the sky depends on the local (subaperture) wavefront gradient. The spots are imaged through the full telescope aperture, so the position of the final image of each spot will be altered by the global (full aperture) tilt. Hence the position of each spot image gives a measure of the local tilt minus the global tilt – exactly the same quantity as is measured in a conventional Shack-Hartmann wavefront sensor (WFS) when used with a laser beacon. This assumes that the angular size of the spot pattern on the sky is smaller than the isokinetic patch (the angle over which the wavefront tilt is isoplanatic).

The technique could be implemented with either a Rayleigh or a sodium beacon, although implementation of a sodium layer SPLASH system presents more of a challenge in focusing the beams than the Rayleigh version, due to the extremely long focal length. Range gating is essential, for both the Rayleigh and sodium versions of SPLASH, in order to allow the beacons to be imaged without being swamped by backscattered light from lower altitudes.

4.1.2 Focal anisoplanatism

The main proposed advantage of a SPLASH LGS is that it suffers considerably less from FA than a conventional LGS. However, it is still affected by FA and, as a result of the unusual configuration, the FA effects are manifested in a different way to that seen in a conventional LGS/Shack-Hartmann WFS combination.

SPLASH is affected by FA twice, on the upward and downward paths of the light. On the upward path, where the wavefront is sensed, the local gradient measured by each beam will have a slight error due to FA – see figure 4.2. As each spot is then imaged from a different position in the sky, the return paths of the light from the spots each sample the atmosphere differently so that the global tilt on each

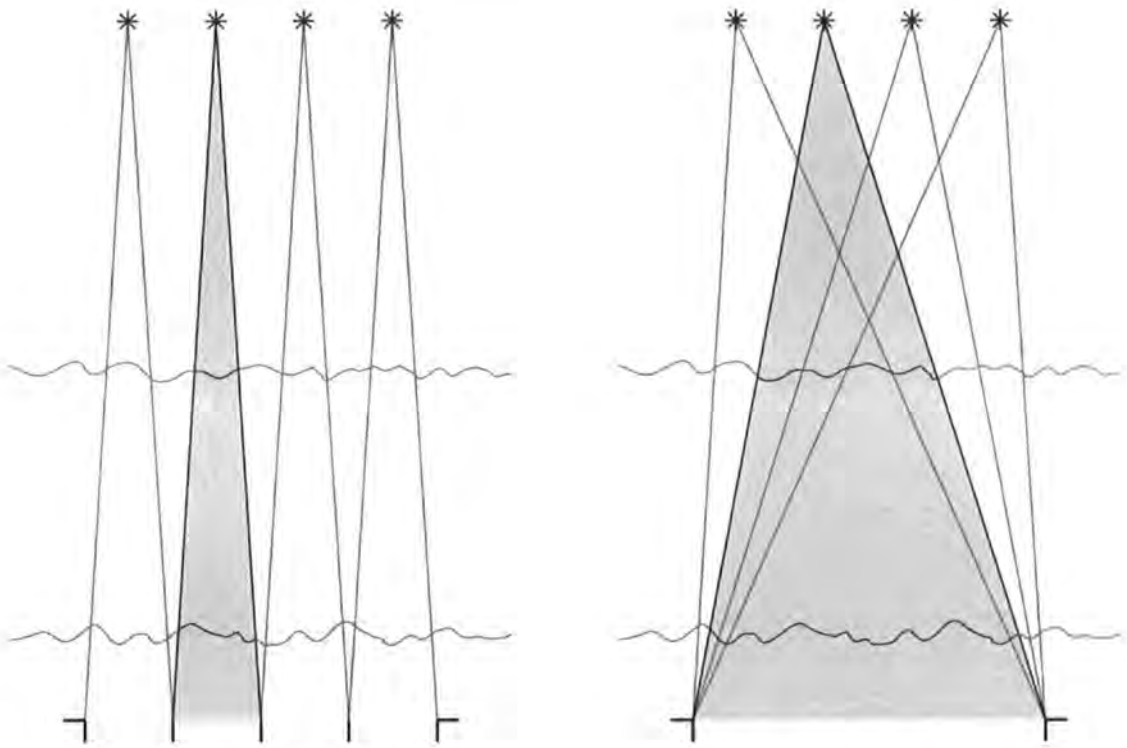

Figure 4.2: *Left:* The upward paths followed by the beams. Each beam samples the atmosphere above its own subaperture, and each beam is affected separately by focal anisoplanatism. *Right:* The downward paths taken by the light from each spot. The spots are observed through the full telescope aperture so the light does not pass through the same section of atmosphere as the upward-propagating (wavefront sensing) beams. The upward-propagating beams are affected by the local wavefront gradient, and the downward beams by the global gradient (corrupted by focal and angular anisoplanatism). The paths from one subaperture are darkened to show the regions of the atmosphere encountered by light from that subaperture. The horizontal lines indicate turbulent layers.

subaperture centroid is separately corrupted by a combination of focal and angular anisoplanatism.

There is an additional error on the upward path due to a "lever arm effect". The distance a spot moves due to a local wavefront tilt depends on the altitude at which the tilt is applied – a ground layer tilt will cause a larger spot motion than a tilt of the same magnitude applied higher up. This is not expected to be a significant problem for closed loop operation, especially for a sodium LGS system, although it will have the effect of slightly reducing the system bandwidth.

4.1.3 Effect of diffraction on SPLASH

Figures 4.1 and 4.2 assume geometrical optics but in reality the SPLASH beams will be affected by diffraction, resulting in a finite spot size on the sky. The minimum size of the spots depends on the size of the launch subapertures, the laser wavelength, the laser beam intensity distribution and the beacon altitude, with the seeing resulting in a further increase in the size of the spots. Thus the spots could potentially overlap on the sky making centroiding difficult or impossible. For the sodium beacon case the longer beam propagation distance will result in larger sky spots than in the Rayleigh beacon case, worsening the problem of overlapping spots.

For beams with a Gaussian intensity profile, minimum spot size on sky would be achieved by launching the beams from subapertures of size $\sim$ 2–3 r_0 (r_0 defined at 500 nm). This would limit the wavefront sampling, meaning that SPLASH would be unsuitable for high-order wavefront sensing. However, such a system would be ideal for AO in the infrared. Launching Gaussian beams would not be possible using the approach illustrated in figure 4.1 but could be achieved using, for example, holographic techniques.

The problem of overlapping spots could also be reduced by implementing a method of time-interleaving the subapertures such that only a subset of the beams would be launched at any given time. All of the spots would be projected and

imaged in each complete cycle of the system, but the wavefront-sensing would be divided into sub-cycles with each sub-cycle involving a combination of subapertures chosen to avoid overlapping of the spots.

Aside from the issue of overlapping spots, diffraction effects may serve to partially remove the effects of FA on the upward paths of the beams. The broadened beams will sample higher-altitude turbulent layers more fully than the idealised geometrical-optics "cones" shown in figures 4.1 and 4.2.

4.1.4 Effect of turbulence on return path

Return path tip/tilt has already been discussed but some consideration needs to be given to higher order aberrations. The subapertures in a conventional Shack-Hartmann WFS are of similar size to the SPLASH launch subapertures, i.e. $\sim r_0$. Thus the wavefront aberration across each subaperture is dominated by low spatial frequencies and the subaperture images are generally not speckled. In SPLASH the sky spots are imaged through the full telescope aperture (with a many-r_0 diameter) and the turbulence-induced aberrations on the downward path can contain significant high spatial frequency aberrations. As a result the PSFs could become speckled, and as the amount of speckling increases the centroid of the PSF can be expected to become poorly correlated with the local wavefront tilt. This effect is known as "centroid anisoplanatism" (Yura and Tavis, 1985; Churnside et al., 1985), and becomes significant for values of D/r_0 greater than about 10.

The speckling effect could be reduced by masking off a large portion of the aperture so that the spot pattern would be imaged through a much smaller aperture. This is not really a viable solution, however, because it would lead to an increase in tip/tilt anisoplanatism (i.e. differences in global tip/tilt on the return paths from the sky spots).

In a closed-loop system the return-path aberrations would be removed by the wavefront corrector, so only the residual wavefront error would contribute to centroid

anisoplantism. However, if the spots were too badly speckled to begin with it might be impossible to close the loop.

4.1.5 Laser power requirements

No formal laser power calculations are presented here, however the power requirements of a SPLASH system can be expected to be comparable to those of a conventional single-LGS system. In a traditional LGS system the light from a single beacon is split between many WFS subapertures. In a SPLASH system, although a separate beacon is launched from each subaperture, each beacon is imaged through the full telescope aperture and the brightness of the beacons can be reduced accordingly. Therefore, providing the beams launched from the different subapertures all have the same intensity, the increase in collecting area balances the increase in the number of beacons. Launch methods in which the beam brightness varies between subapertures, such as that illustrated in figure 4.1, will require higher laser power.

The laser power requirements of SPLASH are favourable in comparison with many other advanced LGS techniques. MCAO, for example, requires a considerable increase in total LGS power compared to single conjugate AO.

I now present a theoretical analysis of SPLASH, taking into account the effect of FA on the upward path but neglecting the effects of diffraction and return path turbulence.

4.2 Theoretical estimate of the effect of FA on SPLASH

This section describes a modal analysis of a SPLASH WFS, giving an estimate of the effect of FA on the upward (wavefront-sensing) path of the light. The effects of turbulence on the return path are excluded (but are considered later in section 4.3).

Zernike polynomials are a convenient basis set for a modal analysis of wavefront

correction on a circular aperture. The same conventions for normalisation and numbering of Zernike modes are used here as described by Noll (1976). The polynomials are defined by

$$\left.\begin{aligned} Z_{even\,j} &= \sqrt{n+1}\mathcal{R}_n^m(r)\sqrt{2}\cos m\theta \\ Z_{odd\,j} &= \sqrt{n+1}\mathcal{R}_n^m(r)\sqrt{2}\sin m\theta \end{aligned}\right\} \quad m \neq 0$$
$$Z_j = \sqrt{n+1}\mathcal{R}_n^0(r), \qquad m = 0 \tag{4.1}$$

where

$$\mathcal{R}_n^m(r) = \sum_{s=0}^{(n-m)/2} \frac{(-1)^s(n-s)!}{s![(n+m)/2-s]![(n-m)/2-s]!} r^{n-2s}. \tag{4.2}$$

The phase distortion, $\phi(R\mathbf{r})$, across a circular aperture can be expressed in terms of Zernike polynomials as

$$\phi(R\mathbf{r}) = \sum_{j=1}^{\infty} a_j Z_j(\mathbf{r}), \tag{4.3}$$

where R is the radius of the aperture, $\mathbf{r}$ is the spatial coordinate normalised to unit radius and a_j are the Zernike coefficients, given by

$$a_j = \int \phi(R\mathbf{r}) Z_j(\mathbf{r}) W(\mathbf{r}) \mathrm{d}\mathbf{r}, \tag{4.4}$$

where $W(\mathbf{r})$ is the pupil function. The aperture-averaged phase (piston) is explicitly excluded from the summation in equation 4.3. If the first N Zernike modes could be perfectly corrected, the residual wavefront distortion would then be

$$\phi(R\mathbf{r}) = \sum_{N+1}^{\infty} a_j Z_j(\mathbf{r}). \tag{4.5}$$

Providing the Zernike modes are normalised as described by Noll (1976), the mean square residual phase error across the aperture can be written as

$$\sigma_\phi^2 = \langle \phi^2 \rangle - \sum_{j=1}^{N} \langle |a_j|^2 \rangle. \tag{4.6}$$

A wavefront sensor gives estimates b_j of the first N Zernike coefficients a_j. If these modes were corrected as accurately as they could be measured, the residual phase variance would be

$$\begin{aligned}
\sigma_\phi^2 &= \sum_{j=1}^{N}\langle|a_j - b_j|^2\rangle + \sum_{j=N+1}^{\infty}\langle a_j^2\rangle \\
&= \sum_{j=1}^{N}\langle|a_j^2 + b_j^2 - 2a_jb_j|\rangle + \sum_{j=N+1}^{\infty}\langle a_j^2\rangle \\
&= \sum_{j=1}^{\infty}\langle a_j^2\rangle + \sum_{j=1}^{N}\left(\langle b_j^2 - 2a_jb_j\rangle\right) \\
&= \sum_{j=1}^{\infty}\langle a_j^2\rangle + \sum_{j=1}^{N}\langle b_j^2\rangle - 2\sum_{j=1}^{N}\langle a_jb_j\rangle. \qquad (4.7)
\end{aligned}$$

For Kolmogorov turbulence, the variances of the modal coefficients $\langle a_j^2\rangle$ are given by the leading diagonal of Noll's Zernike covariance matrix. Thus to predict the performance of the WFS, one needs to know the variances of the estimated modal coefficients $\langle b_j^2\rangle$ and the covariances between the estimated modal coefficients and the actual modal coefficients $\langle a_jb_j\rangle$. These variances can be calculated for a WFS with an NGS using techniques described by Wilson and Jenkins (1996) and Cubalchini (1979).

The phase gradient averaged over subaperture i of a Shack-Hartmann WFS is given by

$$g_i = \frac{\lambda}{\pi D}\sum_{j=1}^{\infty} a_j \int_{\text{subaperture } i} \nabla Z_j(\mathbf{r})\mathrm{d}\mathbf{r} \qquad (4.8)$$

where D is the telescope aperture diameter and λ is the wavelength (the factor $\lambda/\pi D$ scales the phase tilt from units of radians of phase per telescope radius to radians of angle). There are two orthogonal phase gradients for each subaperture (commonly referred to as tip and tilt). This equation can be written in matrix form as

$$\mathbf{g} = \frac{\lambda}{\pi D}\mathscr{D}^{\infty}\mathbf{a} \qquad (4.9)$$

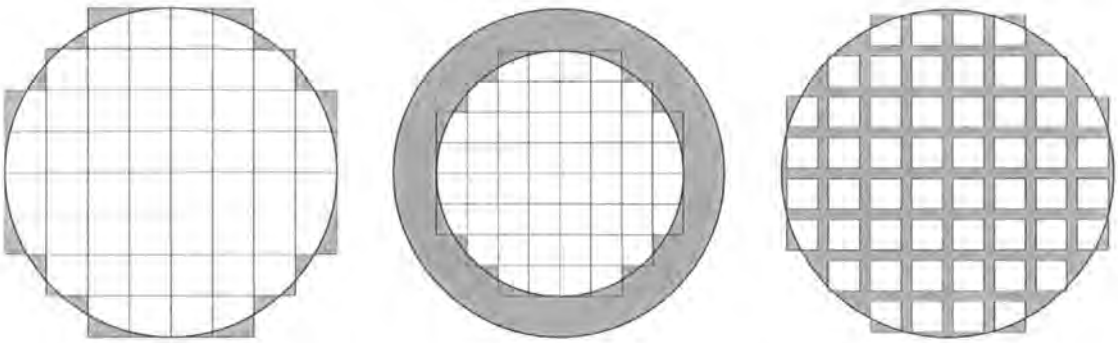

Figure 4.3: Illustration of how the telescope pupil is projected onto a turbulent layer at height $h = H/4$. Areas shaded grey are not sensed. *Left:* Natural guide star – light is parallel so the pupil is fully sampled at all altitudes; *Middle:* Conventional LGS – as a result of FA, the entire pupil is projected onto a smaller circle as altitude increases; *Right:* SPLASH – each subaperture is projected onto a smaller square with increasing altitude as a result of FA, but the spacing of the subapertures remains the same.

where $\mathbf{g}$ and $\mathbf{a}$ are the vectors of subaperture gradients and modal coefficients respectively and $\mathscr{D}^{\infty}$ is the matrix of (x and y) subaperture-averaged derivatives of a large number of Zernike functions. Note that, due to the Zernike normalisation used, the elements of $\mathscr{D}^{\infty}$ are in units of radians of phase per telescope radius. The modal coefficient estimates $\mathbf{b}$ are usually found using

$$\mathbf{b} = \frac{\pi D}{\lambda} \mathscr{D}^{-1} \mathbf{g} \tag{4.10}$$

where $\mathscr{D}^{-1}$ is the least squares inverse of a $\mathscr{D}$-matrix containing a small number of Zernike modes (only as many as the WFS is of sufficiently high order to measure). The modal covariance matrix for the WFS is given by

$$\mathbf{C} = \left(\frac{\pi D}{\lambda}\right)^2 \mathscr{D}^{-1} \mathbf{G} (\mathscr{D}^{-1})^T \tag{4.11}$$

where $\mathbf{G}$ is a matrix of tip and tilt covariances between subapertures (i.e. $\mathbf{G}_{il} = \langle g_i g_l \rangle$). Each element of the matrix $\mathbf{C}$ is a covariance between two Zernike modes, i.e. $\mathbf{C}_{jk} = \langle b_j b_k \rangle$. For a perfect wavefront sensor the matrix $\mathbf{C}$ would be equal to Noll's matrix (i.e. $\langle b_j b_k \rangle = \langle a_j a_k \rangle$).

Up to this point the analysis described has been for a Shack-Hartmann WFS viewing an NGS (equivalent to a conventional LGS or SPLASH system with turbulence only at the ground, i.e. with no FA). We are interested in the effect of FA on the performance of a SPLASH WFS, so this is now introduced into the analysis.

Consider an atmosphere consisting of just one turbulent layer (although extending the analysis to include multiple layers is straightforward). The height of the layer above the ground is taken to be h and the beacon height to be H. Figure 4.3 shows how FA affects the sampling of an atmospheric layer. Define b'_j to be the SPLASH estimate of Zernike coefficient a_j in the presence of FA (note that b_j still represents the estimate a_j in the absence of FA). Thus, with reference to equation 4.7, the residual phase variance is now given by

$$\sigma_\phi^2 = \sum_{j=1}^{\infty} \langle a_j^2 \rangle + \sum_{j=1}^{N} \langle b_j'^2 \rangle - 2 \sum_{j=1}^{N} \langle a_j b'_j \rangle. \tag{4.12}$$

Define g'_i to be the phase gradient averaged over the projection of subaperture i onto the turbulent layer, given by

$$g'_i = \frac{\lambda}{\pi D} \sum_{j=1}^{\infty} a_j \int_{\text{subaperture } i \text{ with FA}} \nabla Z_j(\mathbf{r}) \mathrm{d}\mathbf{r}. \tag{4.13}$$

Then $\mathbf{g}'$ is the vector of FA-affected subaperture gradients, given by

$$\mathbf{g}' = \frac{\lambda}{\pi D} \mathscr{D}'^{\infty} \mathbf{a} \tag{4.14}$$

where $\mathscr{D}'^{\infty}$ is the matrix of a large number of Zernike functions averaged over FA-projected subapertures (see Figure 4.3). Two more modal covariance matrices can now be calculated:

$$\mathbf{C}' = \left(\frac{\pi D}{\lambda}\right)^2 \mathscr{D}'^{-1} \mathbf{G}' (\mathscr{D}^{-1})^T \tag{4.15}$$

$$\mathbf{C}'' = \left(\frac{\pi D}{\lambda}\right)^2 \mathscr{D}'^{-1} \mathbf{G}'' (\mathscr{D}'^{-1})^T \tag{4.16}$$

where the elements of these **G**- and **C**-matrices are

$$\mathbf{G}'_{il} = \langle g_i g'_l \rangle \tag{4.17}$$

$$\mathbf{G}''_{il} = \langle g'_i g'_l \rangle \tag{4.18}$$

$$\mathbf{C}'_{jk} = \langle b_j b'_k \rangle \tag{4.19}$$

$$\mathbf{C}''_{jk} = \langle b'_j b'_k \rangle. \tag{4.20}$$

It is assumed that the performance of the wavefront sensor is essentially perfect in the absence of FA, i.e. $a_j = b_j$. Since we are interested in investigating the effect of FA on SPLASH this is a reasonable assumption, providing that the number of reconstructed modes is limited sufficiently to avoid significant fitting error. Thus the diagonals of the matrices $\mathbf{C}'$ and $\mathbf{C}''$ are equal to the values $\langle a_j b'_j \rangle$ and $\langle b'^2_j \rangle$ respectively, which are the unknowns required in equation 4.12.

The matrices **G**, $\mathbf{G}'$ and $\mathbf{G}''$ are constructed by mapping tilt covariances for pairs of apertures with appropriate spatial separations into square arrays which use the same subaperture geometry along both axes as the subaperture axis of the $\mathscr{D}$-matrices. An efficient method of calculating the tilt covariance between two spatially separated spatial apertures has been described by Assémat (2004). The tip/tilt covariances between subapertures i and l are given by

$$\langle g_{i,x} g_{l,x} \rangle = \frac{1}{2d^2} \left[\frac{\partial^2 D_\varphi}{\partial x^2}(x,y) \otimes I_{il}(x,y) \right] \tag{4.21}$$

$$\langle g_{i,x} g_{l,y} \rangle = \frac{1}{2d^2} \left[\frac{\partial^2 D_\varphi}{\partial x \partial y}(x,y) \otimes I_{il}(x,y) \right] \tag{4.22}$$

where the x and y subscripts indicate the direction of the tilts. $I_{il}(x,y)$ is the intercorrelation of the two aperture functions, defined by

$$I_{il}(x,y) = \iint \Pi\left(\frac{u+x}{d}, \frac{v+y}{d}\right) \Pi\left(\frac{u}{d}, \frac{v}{d}\right) \mathrm{d}u\mathrm{d}v \tag{4.23}$$

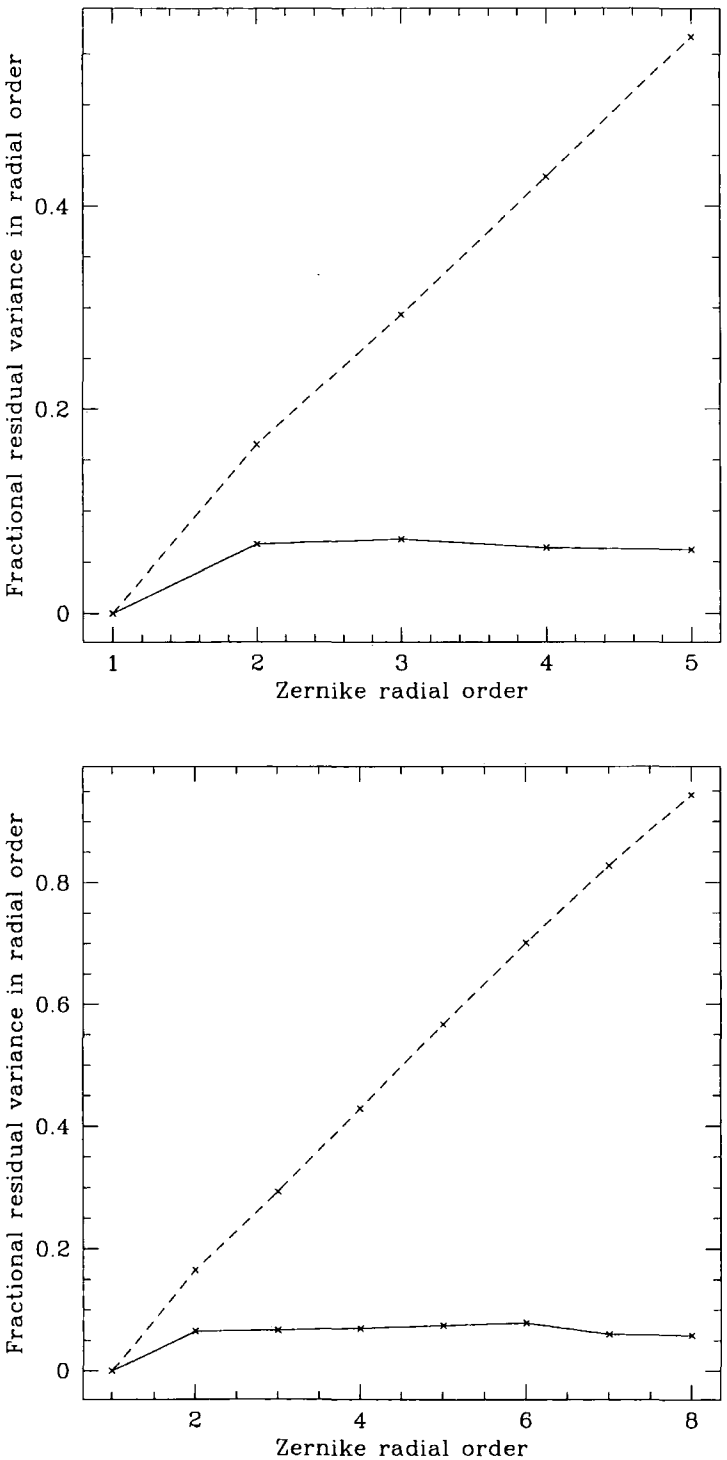

Figure 4.4: Theoretical prediction of SPLASH performance (solid line) as compared with an equivalent conventional LGS/Shack-Hartmann wavefront sensor system (broken line). Results show residual wavefront variance as a fraction of uncorrected variance in each radial order of Zernikes, for a single atmospheric layer at 1/4 of the beacon altitude. *Upper:* 8×8 array of subapertures; *Lower:* 12×12 array of subapertures.

where d is the subaperture size and $\Pi(x, y)$ is the aperture function, given by

$$\begin{aligned} \Pi(x,y) &= 1 \quad |x| < 1/2 \text{ and } |y| < 1/2 \\ &= 0 \quad \text{otherwise.} \end{aligned} \tag{4.24}$$

D_φ is the phase structure function which, assuming Kolmogorov turbulence, is given by

$$D_\varphi(x,y) = 6.88 r_0^{-5/3}(x^2+y^2)^{5/6}. \tag{4.25}$$

When one or both of the subapertures are affected by FA, one of the following equations is used:

$$I'_{il}(x,y) = \iint \Pi\left(\frac{u+x}{d}, \frac{v+y}{d}\right) \Pi\left(\frac{u}{\beta d}, \frac{v}{\beta d}\right) \mathrm{d}u\mathrm{d}v \tag{4.26}$$

$$I''_{il}(x,y) = \iint \Pi\left(\frac{u+\beta x}{\beta d}, \frac{v+\beta y}{\beta d}\right) \Pi\left(\frac{u}{\beta d}, \frac{v}{\beta d}\right) \mathrm{d}u\mathrm{d}v \tag{4.27}$$

where β is an FA factor, defined by

$$\beta = 1 - \frac{h}{H}. \tag{4.28}$$

Thus we have all the information required to predict the residual wavefront variance for a given number of corrected Zernike modes. I have assumed the cone geometry shown in figure 4.1, and that the system is capable of perfectly correcting Zernike modes to the degree that they can be sensed. I also assume that tip and tilt across the full telescope aperture can be perfectly sensed, since these modes would be sensed using an NGS rather than the laser beacon.

The results of the theoretical analysis of SPLASH are shown in figure 4.4. The benefits of the better sampling of the wavefront provided by SPLASH can clearly be seen in the plot. The fractional residual variance in each mode (i.e. the proportion of the variance in each mode that cannot be sensed and corrected) is roughly constant at each spatial scale for SPLASH, whereas the effect of FA on a conventional LGS

becomes more severe as the spatial frequency of the aberrations increases. The results indicate that a SPLASH system could be expected to perform significantly better than an equivalent system using a conventional LGS with a Shack-Hartmann WFS, and that the benefits are greater for larger telescope apertures.

It is important to remember that the effects of atmospheric aberrations on the downward path of the light from the focused spots have been ignored. These effects are included in the numerical simulation described in the next section.

4.3 Closed loop simulation

A closed-loop semi-geometrical Monte Carlo simulation of SPLASH has been implemented. This includes the effects of aberrations on the return path of the light through the atmosphere in addition to the upward-path FA considered in the theoretical analysis.

For the purposes of the simulation a uniform intensity distribution was assumed for the laser beams, with each beam being focused onto the sky by a lens. The beacons were assumed to be sufficiently bright to ignore the effects of photon noise and CCD read noise.

The simulation assumes the diffraction-free geometry illustrated in figure 4.2 for the purposes of identifying the sections of atmosphere intersected by the beams, but far-field diffraction is included in the PSF calculations. For each sky spot, and at each time step, the phase aberration induced on the upward path is calculated and the on-sky PSF is calculated as a two dimensional fast Fourier transform (FFT) of the complex amplitude across the subaperture. Similarly, the phase aberration on the downward path is projected onto the full telescope aperture and the downward-propagation PSF is calculated as the FFT of the complex amplitude across the telescope aperture. The total PSF (the LGS PSF imaged through the atmosphere) is calculated by convolving the upward and downward PSFs.

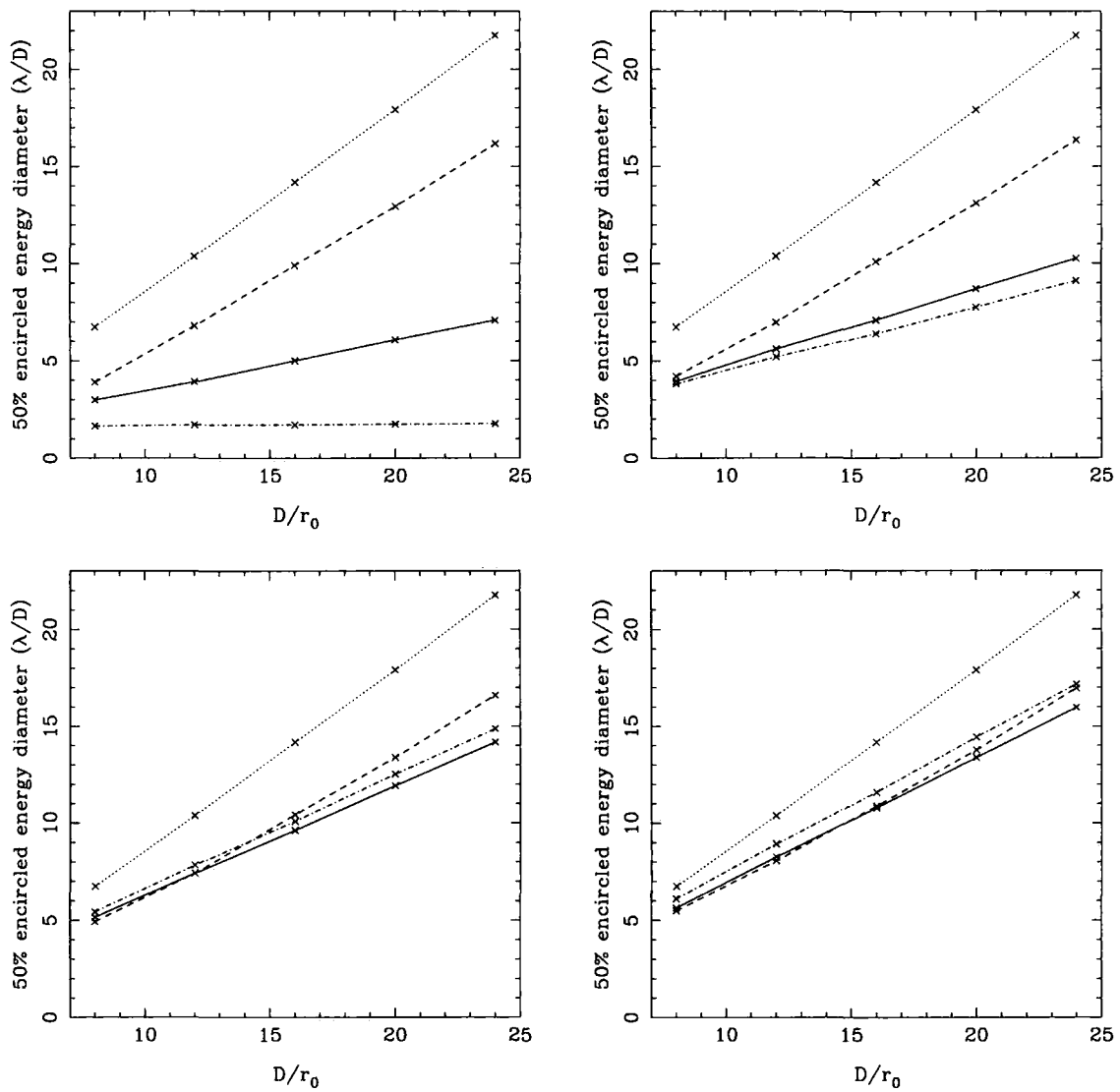

Figure 4.5: Numerical simulation results: Science PSF 50% encircled energy diameters (in units of λ/D) for a SPLASH LGS AO system (solid line), an equivalent conventional LGS AO system (broken line) and an equivalent NGS AO system (dot-dashed line). The dotted line shows the case with only tip-tilt correction. *Top left:* performance on-axis; *top right:* off-axis angle $\theta = 1.94r_0/H$; *bottom left:* $\theta = 3.88r_0/H$; *bottom right:* $\theta = 5.82r_0/H$. r_0 is the Fried parameter and H is the altitude of the laser beacons. Error bars are not shown as they are narrower than the data points.

The simulated spots are centroided separately – they are not "stitched" together into a complete spot pattern. It is assumed that if the combination of the size and motion of the spots is sufficient to cause cross-contamination, this can be avoided by time-interleaving the spots.

The wavefront corrector used is an idealised segmented DM consisting of square segments each capable of correcting piston, tip and tilt. Each mirror segment is aligned perfectly with a SPLASH subaperture. The DM segment tip and tilt values correspond directly to the corresponding spot x and y centroids, and the subaperture piston values across the DM are reconstructed from the centroids using a successive over-relaxation (SOR) algorithm (Southwell, 1980). As in the previous section, perfect (NGS) global tip/tilt correction is assumed.

The atmosphere is modelled using periodic Kolmogorov phase screens which are generated by spatially filtering simulated noise as described by Ellerbroek and Cochran (2002). For each phase screen, a two dimensional array of Rayleigh-distributed random numbers is generated, multiplied by the square root of the Kolmogorov PSD and the result converted into optical phase errors via a two dimensional FFT. The resulting phase screens are made to be several times the size of the telescope pupil so as to minimise outer scale effects imposed by the finite array size.

The atmosphere model consisted of three phase screens at the ground (i.e. zero altitude), at $H/4$ and at $H/2$ (where H is the beacon altitude), with the relative strengths of the turbulence at these altitudes being 50%, 40% and 10% respectively. A range of different D/r_0 values were simulated and for each one, the number of subapertures was matched to D/r_0, i.e. for $D/r_0 = 8$, an 8×8 subaperture WFS (and DM) was used.

A conventional LGS AO system with the same DM, atmosphere model, beacon altitude, tip/tilt correction etc. was also simulated to allow an objective comparison with SPLASH, and an equivalent NGS AO system (i.e. with no FA) was simulated

to demonstrate the (single-conjugate) "best case scenario".

The simulations were carried out on a Cray XD1 supercomputer with 12 Opteron processors running SuSE linux. This machine features field programmable gate arrays (FPGAs) for hardware acceleration of numerically intensive processing, but the current version of the SPLASH simulation code does not take advantage of these. Future versions are expected to do so (Basden et al., 2005).

The control loop was successfully closed for all the D/r_0 values simulated and the results are shown in figure 4.5 in the form of 50% encircled energy diameters (the angular diameter within which 50% of the total energy in the long-exposure science PSF is contained). The top-left panel in figure 4.5 shows the on-axis performance of SPLASH to be considerably better than a conventional LGS system across the full range of D/r_0 values that were simulated. While FA is significantly reduced in the SPLASH technique compared to a conventional LGS, the on-axis performance falls short of that of an NGS system due to the remaining FA.

The remaining panels in figure 4.5 compare the off-axis performance of the 3 systems. The off-axis angles are defined in terms of the beacon altitude, H, and the Fried parameter, r_0, so as to keep the results as general as possible. For example, for observing at $\lambda \sim 2\mu$m with $H = 20$ km and $r_0 = 50$ cm (a reasonable value at this wavelength) the top-right, bottom-left and bottom-right panels correspond to off-axis angles of 10, 20 and 30 arcseconds respectively. In the top-right panel, the NGS performance can be seen to have degraded considerably while the performance of SPLASH degrades only slightly (and is still noticeably better than the conventional LGS). For larger off-axis angles the 3 methods (NGS, conventional LGS and SPLASH LGS) have comparably poor performance as would be expected due to the high degree of angular anisoplanatism. SPLASH has a small advantage over an NGS system for small off-axis angles because it samples lower turbulent layers better than higher layers. Layers closer to the ground are thus corrected more completely than higher layers (the same effect used in GLAO) resulting in a larger corrected field of

view.

The simulation results show that the technique could be suitable for use on existing telescopes – for example the results for $D/r_0 = 24$ correspond to observing on an 8 m telescope at $\lambda = 1\mu$m with $r_0 = 33$ cm (defined at 1μm – equivalent to $r_0 = 14.5$ cm defined at 500 nm).

As D/r_0 increases further (beyond the range of values presented here), the residual wavefront error will worsen and centroid anisoplanatism become more noticeable. However, due to current limitations in computer power it has not been feasible to extend simulations to significantly larger apertures. For sufficiently large D/r_0 the residual wavefront error can be expected to prevent effective wavefront sensing, although the regime in which this occurs will be sensitive to the distribution of turbulence in the atmosphere. Further simulations to higher D/r_0 values (and with a range of atmosphere models) would be required to confidently assess the applicability of the SPLASH technique to ELTs.

4.4 Conclusion

I have described a new method of LGS wavefront sensing, SPLASH, in which an array of Shack-Hartmann spots are projected onto the sky and then imaged through the telescope.

I have shown theoretically that, in the absence of any return-path wavefront aberrations, and assuming purely geometrical optics, such a system can be expected to suffer considerably less from focal anisoplanatism than an equivalent conventional LGS system.

I have further demonstrated the validity of the technique using a semi-geometrical closed-loop simulation with a realistic atmosphere model, in which return-path aberrations were included in addition to upward-path turbulence. This simulation demonstrates the improvement in performance over a conventional single-LGS AO

system for a range of D/r_0 values up to those approximately consistent with an 8 m class telescope.

Useful steps which could be taken in the future to advance this work would be further numerical simulations for larger aperture sizes to investigate the feasibility of the SPLASH technique for ELTs and experimental verification of the technique on-sky on an existing 4 or 8 m class telescope.

Chapter 5

Calibration of SLODAR

In this chapter I present work, most of which is published in Butterley et al. (2006b), describing how to calibrate accurately the SLODAR turbulence profiling technique. Sections 5.2 and 5.3 describe work carried out collaboratively with Richard Wilson. Sections 5.3.2-5.3.4 briefly describe work carried out by Richard Wilson but are included here for completeness.

5.1 Description of the SLODAR technique

Slope Detection and Ranging (SLODAR) was proposed by Wilson (2002) and is a method for measuring the strength of atmospheric turbulence as a function of altitude ($C_n^2(h)$). The technique is based on triangulation of turbulence using a binary star. The binary star is observed using a Shack-Hartmann WFS and the WFS subaperture image centroids from the two stars are cross-correlated. The resulting cross-correlation is equal to the turbulence profile convolved with a response function. The turbulence profile is recovered by deconvolving or fitting to this response function.

In addition to $C_n^2(h)$, the Fried parameter, r_0, can be measured, for example, by decomposing the measured wavefronts into Zernike polynomials and fitting to the known Zernike variances for Kolmogorov turbulence. The velocities of the turbulent

layers can also be measured via cross-correlations of sets of WFS centroids with different temporal offsets.

The SLODAR technique was first demonstrated on the 4.2 m William Herschel Telescope (WHT) on La Palma, using a 12 × 12 subaperture WFS based on a relatively low-specification firewire CCD camera (Wilson and Saunter, 2003). A similar SLODAR instrument with a 10 × 10 WFS was then deployed on the nearby 1 m Mercator telescope on La Palma for several months (Wilson et al., 2004b).

A prototype "relocatable" system was developed for ESO (Wilson et al., 2004a) using a 40 cm Meade telescope and an 8 × 8 subaperture WFS based on an Andor L3CCD camera. Zero read noise L3CCD technology was essential to cope with the low photon counts and high frame rates required to operate with such small (5 cm) subapertures. This system was tested at ING, La Palma and at CTIO, Chile (Sarazin et al., 2005) and has since been used extensively at ESO's Paranal observatory in Chile. A virtually identical version of this system has recently been deployed on the roof of the University of Hawaii 88-inch telescope Coudé building to carry out a campaign of ground-layer turbulence profiling for the GEMINI GLAO project. A robotic version of the system is currently in development for permanent installation at ESO Paranal in 2007.

5.2 The theoretical impulse response for SLODAR

A SLODAR instrument measures the spatial covariance of the gradient of the optical phase aberration observed at ground level. The turbulence altitude profile is found via triangulation, as shown in figure 5.1. A layer at altitude H produces a peak in the cross-covariance function at a spatial offset equal to $H\theta$. If the 'impulse response' of the system – the shape of the covariance for a thin layer at a given altitude – is known, then the turbulence profile can be recovered via a fit to the measured cross-covariance function.

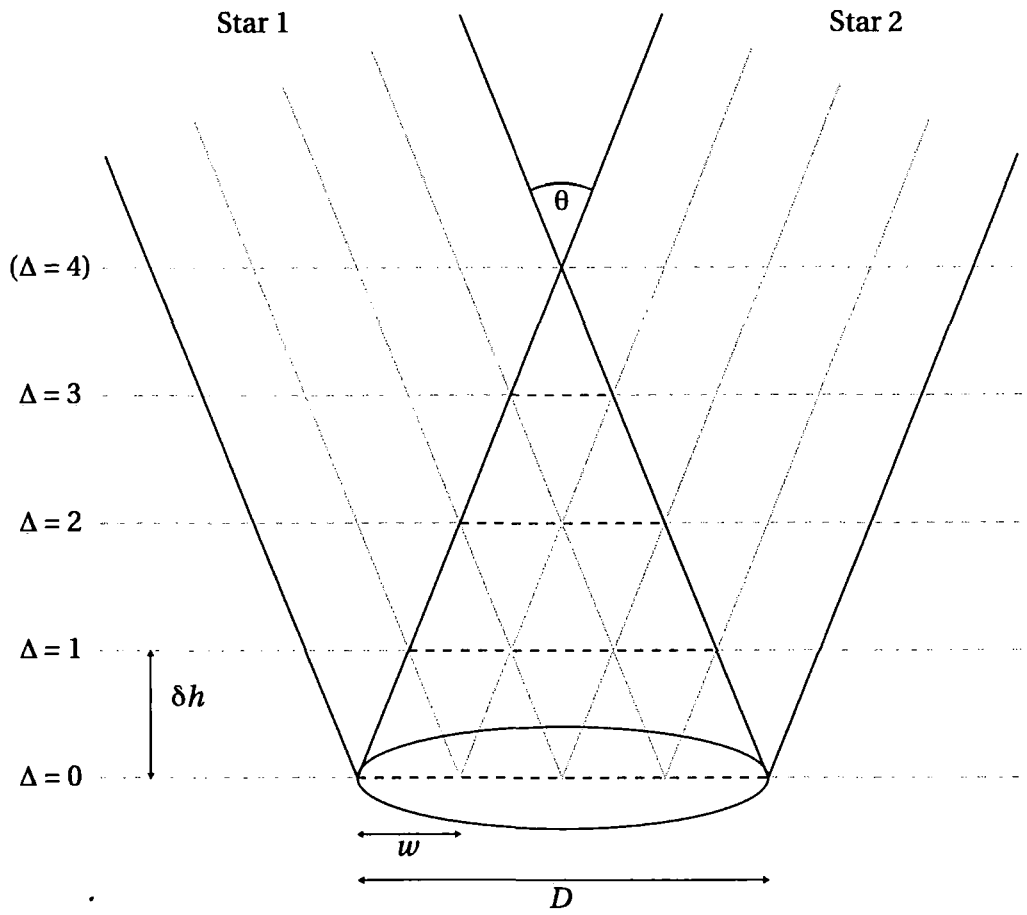

Figure 5.1: Overview of the SLODAR method geometry. θ is the angular separation of the double star target. D is the diameter of the telescope pupil and w the width of a single subaperture in the Shack-Hartmann array. The centres of the sampling bins in altitude are given by $\Delta\delta h$.

The fit yields an estimate of the integrated turbulence strength in the altitude bins corresponding to each of the spatial offsets in the measured slope covariance function. The width of the bins is given by:

$$\delta h = \frac{w}{\theta} \tag{5.1}$$

where w is the width of a WFS subaperture and θ is the angular separation of the target double star. If the WFS optics are collimated so that the lenslet array is at the optical conjugate of the telescope entrance aperture, then the point in the covariance function for zero spatial offset will correspond to a range of altitudes of width δh centred at the telescope. The remaining bins, of equal size, will be centred at altitudes $i\delta h, i = 1, \ldots, (N-1)$ where N is the number of WFS subapertures across the telescope pupil.

Hence the resolution in altitude of a SLODAR system is determined by the width of the WFS subapertures and the angular separation of the target. For a given resolution δh the maximum altitude for direct sensing of the turbulence profile is simply δh multiplied by the number of subapertures across the WFS.

For a system based on a small telescope the lowest altitude layers may be examined in detail by choosing targets with large separations. The main application of the ESO portable SLODAR system is characterization of the ground layer turbulence, typically with a resolution of 150 m to a maximum altitude of approximately 1 km. Low resolution ($\delta h \sim 2$ km) profiles up to high altitudes can also be measured. For a WFS with, for example, 80×80 subapertures deployed on an 8 m telescope, profiles with a resolution of 200 m could be determined to a maximum altitude of 16 km. For any SLODAR system the total optical turbulence strength for the whole atmosphere is also measured. Hence the integrated turbulence at all altitudes greater than the maximum altitude for direct sensing is determined as the difference of the total turbulence strength and the sum of the directly measured profile.

I now determine theoretical expressions for the SLODAR cross-covariance as a function of the turbulence altitude. The centroid data for the Shack-Hartmann wavefront sensor are a measure of the slope of the wavefront over each subaperture. $s_{i,j}^{x[1]}(t)$ is the slope in the x direction for the subaperture $[i,j]$ for the first star, where i and j index the position of a subaperture in the SH array horizontal (x) and vertical (y) directions at time t, for the first star. Similarly $s_{i,j}^{x[2]}(t)$ for the second star.

$$s_{i,j}^{x[1]} = \int \phi(w\mathbf{r}_{i,j}^{[1]}) F_x(\mathbf{r}_{i,j}^{[1]}) W(\mathbf{r}_{i,j}^{[1]}) \mathrm{d}\mathbf{r}_{i,j}^{[1]} \tag{5.2}$$

where $\mathbf{r}_{i,j}^{[1]}$ is a spatial coordinate, defined in units of the subaperture width w, with its origin at the centre of subaperture $[i,j]$ for star 1 (similarly $\mathbf{r}_{i',j'}^{[2]}$ for subaperture $[i',j']$, star 2). $\phi(w\mathbf{r}_{i,j}^{[1]})$ is the optical phase in the plane of the aperture. $W(\mathbf{r})$ is the subaperture pupil function:

$$\begin{aligned} W(\mathbf{r}) &= 1 \text{ for } |x|, |y| < 1/2 \\ &= 0 \text{ otherwise,} \end{aligned} \tag{5.3}$$

and F_x is the linear slope function in the relevant direction, normalised such that

$$\int F_x^2(\mathbf{r}) W(\mathbf{r}) \mathrm{d}\mathbf{r} = 1. \tag{5.4}$$

The cross-covariance of the slopes for two subapertures is:

$$C_{i,j,i',j'}^{x} = \left\langle s_{i,j}^{x[1]} s_{i',j'}^{x[2]} \right\rangle \tag{5.5}$$

for the slope in the x direction between subapertures $[i,j]$ for star 1 and $[i',j']$ for star 2. Similarly for the y direction. The spatial offset between the subapertures in units of w is $(\delta i, \delta j) = (i'-i, j'-j)$. The angle brackets denote averaging over a large number of independent realisations of the turbulent distortions over the telescope.

The spatial covariance of angle-of-arrival fluctuations has previously been calcu-

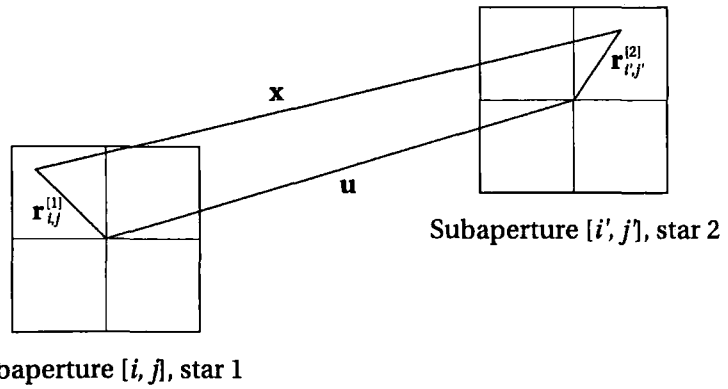

Figure 5.2: Geometry for the calculation of the covariance of wavefront slopes across WFS subapertures.

lated analytically for the von Karman spectrum, for circular apertures, by Conan et al. (2000). However, the same approach is unsuitable here – SH WFS subapertures are square and it is desirable to keep the solution applicable to any turbulence power spectrum.

If the orientation of the double star target is assumed to be aligned along the axis of the WFS in the x direction, then covariance functions can be considered for the tilts in the directions longitudinal (L) and transverse (T) to the spatial offset. The L covariance for a pair of subapertures is given by:

$$C^{x}_{i,j,i',j'} = \iint \left\langle \phi^{[1]}_{i,j}(w\mathbf{r}^{[1]}_{i,j})\phi^{[2]}_{i',j'}(w\mathbf{r}^{[2]}_{i',j'}) \right\rangle F_x(\mathbf{r}^{[1]}_{i,j})F_x(\mathbf{r}^{[2]}_{i',j'}) \times W(\mathbf{r}^{[1]}_{i,j})W(\mathbf{r}^{[2]}_{i',j'})\mathrm{d}\mathbf{r}^{[1]}_{i,j}\mathrm{d}\mathbf{r}^{[2]}_{i',j'} \tag{5.6}$$

The mean phase over the whole of the telescope aperture (the "piston" term) does not affect the measurement of wavefront slopes. The integral can therefore be expressed in terms of the covariance of the phases *relative to the aperture means.* Divergence of the calculation resulting from the pole at the origin of the spatial power spectra of the phase aberrations is then avoided. The covariance of the slopes across two subapertures can be found via a numerical integral involving the spatial

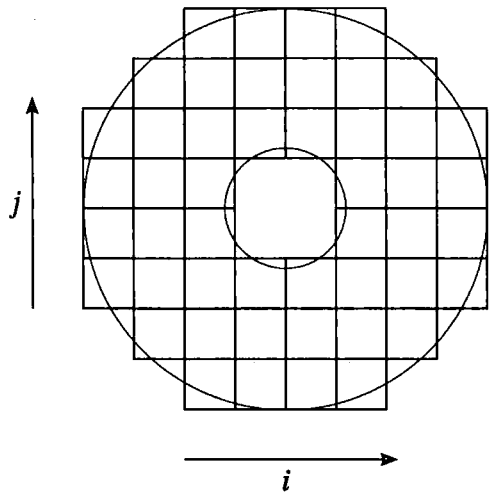

Figure 5.3: Pupil geometry for the 8×8 subaperture ESO portable SLODAR system, showing the mapping of the square wavefront sensor subapertures on to the annular aperture function of the Meade LX200 telescope.

structure function, $D_\phi(w\mathbf{x})$, of the phase aberrations (Wilson and Jenkins, 1996):

$$\begin{aligned}\left\langle \Phi^{[1]}_{i,j}(w\mathbf{r}^{[1]}_{i,j})\Phi^{[2]}_{i',j'}(w\mathbf{r}^{[2]}_{i',j'})\right\rangle &= -\frac{1}{2}D_\phi(w\mathbf{x}) \\ &+\frac{1}{2}\int W(\mathbf{r}^{[1]}_{i,j})D_\phi(w\mathbf{x})\mathrm{d}\mathbf{r}^{[1]}_{i,j} \\ &+\frac{1}{2}\int W(\mathbf{r}^{[2]}_{i',j'})D_\phi(w\mathbf{x})\mathrm{d}\mathbf{r}^{[2]}_{i',j'} \\ &-\frac{1}{2}\iint W(\mathbf{r}^{[1]}_{i,j})W(\mathbf{r}^{[2]}_{i',j'})D_\phi(w\mathbf{x})\mathrm{d}\mathbf{r}^{[1]}_{i,j}\mathrm{d}\mathbf{r}^{[2]}_{i',j'} \end{aligned} \tag{5.7}$$

where $\Phi^{[1]}_{i,j}(w\mathbf{r}^{[1]}_{i,j})$ is the phase relative to the aperture mean,

$$\mathbf{x} = \mathbf{u} + \mathbf{r}^{[2]}_{i',j'} - \mathbf{r}^{[1]}_{i,j} \tag{5.8}$$

and $\mathbf{u}$ is the vector separation of the subapertures in units of the subaperture width w (see figure 5.2), and is given by

$$\mathbf{u} = (i' - i + \Delta, j' - j). \tag{5.9}$$

To remove the effect of common motions induced by telescope guiding errors and wind-shake, the mean slope for all subapertures is subtracted from the instantaneous slopes at each subaperture. The global tilt subtraction is carried out separately for stars 1 and 2. This introduces a dependence of the subaperture covariances on the altitude of the turbulence. For a turbulent layer at an altitude H, corresponding to an offset of $\Delta = H\theta/w$ in the x direction (in units of w) between the projections of the telescope pupil onto the turbulent layer for the two stars, the covariance of the slopes for two subapertures after global tilt subtraction is

$$\begin{aligned} C'^{x}_{i,j,i',j'}(\Delta) &= \left\langle (s^{[1]}_{i,j} - \overline{s^{[1]}})(s^{[2]}_{i'+\Delta_i,j'} - \overline{s^{[2]}}) \right\rangle \\ &= \left\langle s^{[1]}_{i,j} s^{[2]}_{i'+\Delta,j'} \right\rangle - \left\langle s^{[1]}_{i,j} \overline{s^{[2]}} \right\rangle \\ &\quad - \left\langle \overline{s^{[1]}} s^{[2]}_{i'+\Delta,j'} \right\rangle + \left\langle \overline{s^{[1]}}\, \overline{s^{[2]}} \right\rangle \end{aligned} \tag{5.10}$$

where $\overline{s^{[1]}}$ is the slope for star 1 averaged over all subapertures, e.g.

$$\overline{s^{[1]}} = \frac{1}{N_{sub}} \sum_{\text{valid } i,j} s^{[1]}_{i,j} \tag{5.11}$$

$$\left\langle \overline{s^{[1]}} s^{[2]}_{i'+\Delta,j'} \right\rangle = \frac{1}{N_{sub}} \sum_{\text{valid } i,j} \left\langle s^{[1]}_{i,j} s^{[2]}_{i'+\Delta,j'} \right\rangle \tag{5.12}$$

where N_{sub} is the total number of subapertures and "valid i,j" indicates all values of i and j for which the corresponding subaperture is not vignetted (dependent on WFS/pupil geometry, e.g. see figure 5.3).

For SLODAR the slope covariance is averaged over all overlapping subaperture pairs for a given spatial separation $(\delta i, \delta j)$, taking into account the projection of the telescope pupil function onto the subaperture array. The response of SLODAR to a turbulent layer at altitude H is therefore described by

$$X_L(\Delta, \delta i, \delta j) = \frac{1}{N_{cross}} \sum_{\text{valid } i,j,i',j'} C'^{x}_{i,j,i',j'}(\Delta) \tag{5.13}$$

where valid i, j, i', j' refers to all values of i, j, i' and j' such that subapertures $[i, j]$ and $[i', j']$ both exist, remembering that $(i', j') = (i+\delta i, j+\delta j)$. N_{cross} is the number of such existing subaperture pairs for a given $(\delta i, \delta j)$.

The impulse response functions are 2-dimensional. However, 2-dimensional information is only required if the velocities of the turbulent layers are to be measured. Velocity information can be obtained by introducing a temporal offset between the centroid data being correlated for the two stars and observing the resulting spatial offset of the peaks in the two dimensional cross-covariance function. If only the turbulence strength as a function of altitude is required, all of the necessary information is contained in a cut through the two dimensional covariance function in the x direction, at $y = 0$. Hence setting $j = j'$ in equation 5.13 yields a set of 1-dimensional response functions:

$$X_L(\Delta, \delta i) = \frac{1}{N_{cross}} \sum_{\text{valid } i,j,i'} C'^{x}_{i,j,i',j}(\Delta). \tag{5.14}$$

The shape of the slope covariance function depends on the underlying power law describing the spatial fluctuations of the phase. For the standard Kolmogorov model of atmospheric turbulence, the spatial spectrum of aberrations at the ground follows a power law with exponent $-11/3$. Here two alternative models for the spatial power spectrum are also explored – the von Karman spectrum and the generalized spectrum (both introduced in section 2.3).

For a given WFS and telescope pupil geometry the individual subaperture tilt covariances (with global tilt correction) can now be calculated from equations 5.6 and 5.7 via numerical integration. The SLODAR impulse response functions are then found from equation 5.14 by averaging over all overlapping subaperture pairs for each offset δi.

Figures 5.4 and 5.5 plot the resulting normalised impulse response functions for the case of the 8×8 subaperture system with the geometry shown in figure 5.3.

The ratio of the telescope aperture size to the diameter of central obscuration in this case is identical to that for the 40 cm Meade LX200 telescope employed for the ESO portable SLODAR system. The shape of the response functions for this case will be correct for any system with the same WFS/pupil geometry, regardless of the telescope aperture size. Subapertures that are less than 70% illuminated are excluded from the analysis. The plots in figure 5.4 show the longitudinal and transverse response functions for the von Karman power spectrum with $L_0 = 1$, 2 and 10 times the telescope aperture diameter. The plots in figure 5.5 show the response functions for the generalized power spectrum with $\beta = 9/3$, $10/3$ and $11/3$. In each plot the response functions are normalised to the value of the covariance for $\delta_i = 0$ and $\Delta = 0$.

For the von Karman spectrum and a given value of L_0, the impulse response functions scale as $r_0^{-5/3}$. For the generalised spectrum they scale as $\rho_0^{2-\beta}$.

Strictly, equation 5.2 refers to the Zernike tilt ("Z-tilt") of the wavefront across the subaperture. This differs slightly from the mean or gradient tilt ("G-tilt") of the wavefront (see e.g. Tokovinin (2002)). The actual gradient measured will be closer to the Z-tilt or G-tilt depending on the details of the image centring algorithm used. The classical centroid, or centre of mass, yields the G-tilt. However if the images are strongly thresholded or are fitted to a Gaussian then the measured tilt will be closer to the Z-tilt. A Monte-Carlo simulation of the SLODAR wavefront sensor, based on translating random phase screens with the required spatial structure function of aberrations, was used to provide an independent check on the form of the impulse response functions and to investigate any possible effect resulting from the details of the centroiding algorithm. The centroiding algorithm employed in the simulation was identical to that used for analysis of real SLODAR data. A threshold was applied to the image data before calculation of the centre of mass to remove the influence of detector read-out noise on the centroids. The results for the simulation matched the numerical results shown in figures 5.4 and 5.5 to within the statistical

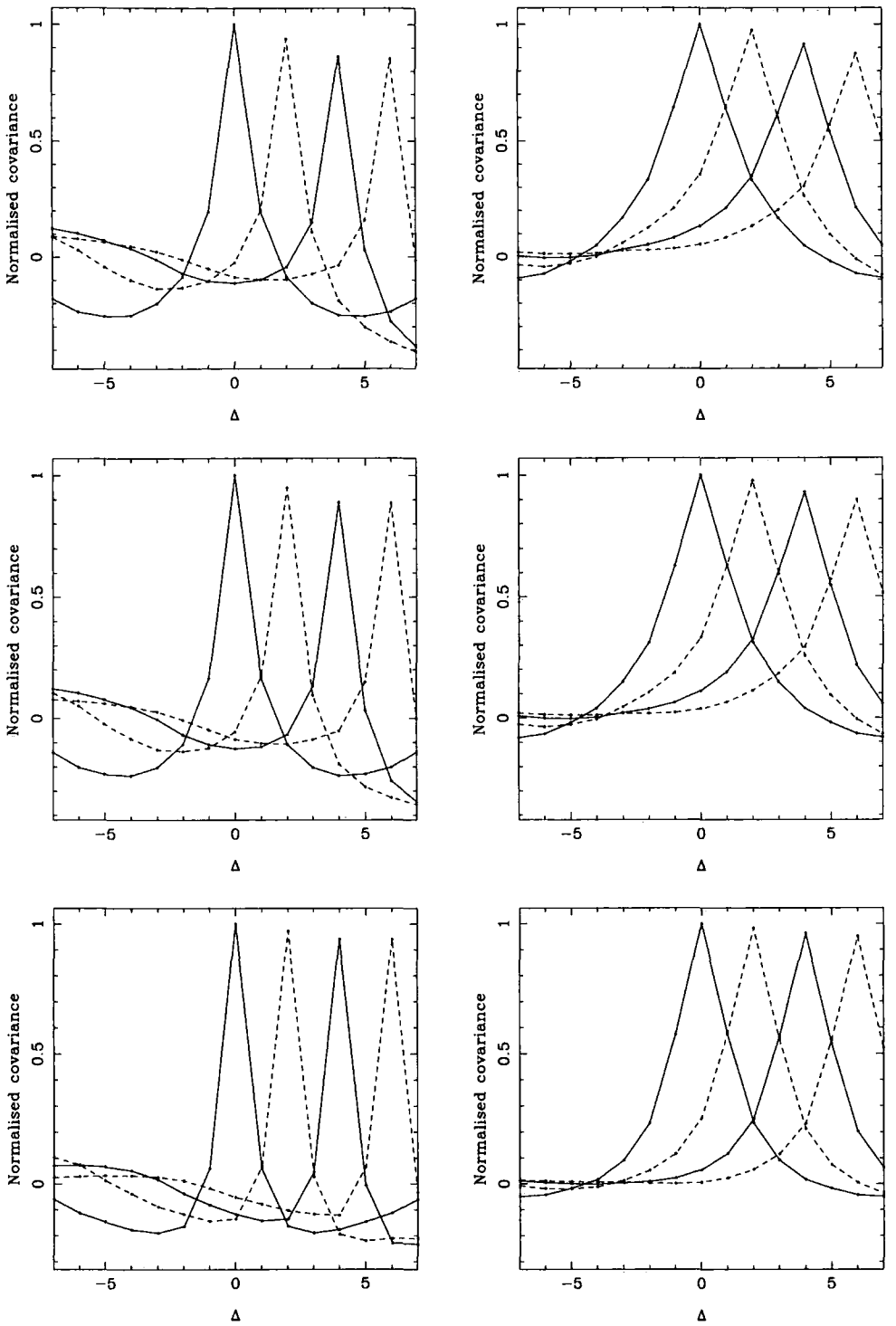

Figure 5.4: Normalised SLODAR theoretical impulse response functions for the von Karman spectrum of turbulence and the 8 by 8 wavefront sensor geometry shown in figure 5.3. *Left:* longitudinal (L), *right*: transverse (T) covariance. From top to bottom, L_0 = 10, 2 and 1 times the telescope aperture diameter. Each plot shows response functions for $\Delta = 0$ (peak at $\delta i = 0$), 2, 4 and 6, corresponding to increasing layer altitudes above the telescope. In each panel, the covariance values are normalised relative to the value for $\delta i = 0$ and $\Delta = 0$.

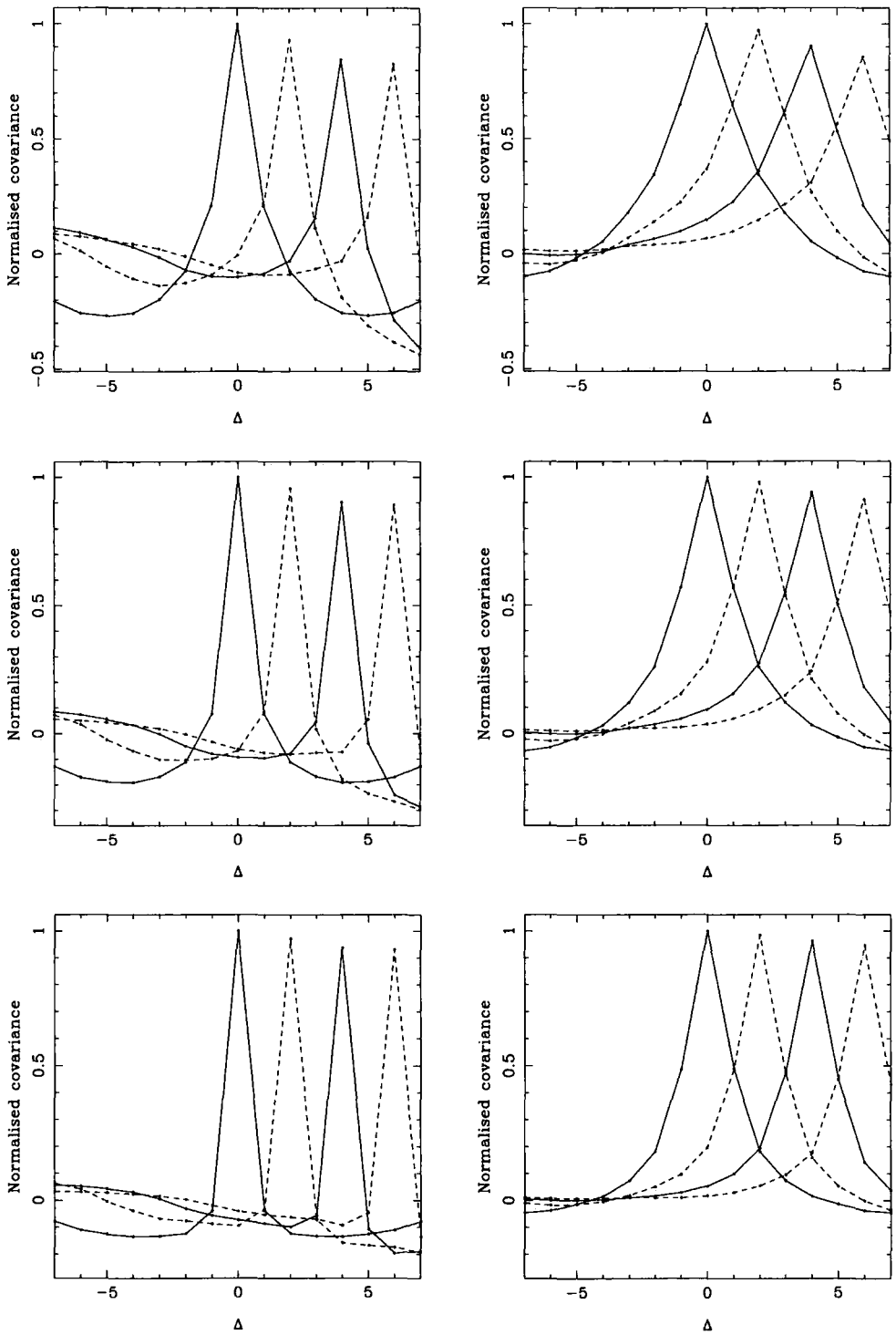

Figure 5.5: Normalised SLODAR theoretical impulse response functions for generalized spectrum, for the wavefront sensor geometry shown in figure 5.3. *Left:* longitudinal (L), *right:* transverse (T) covariance. From top to bottom, $\beta = 11/3$, 10/3, 9/3. Each plot shows response functions for $\Delta = 0$ (peak at $\delta i = 0$), 2, 4 and 6, corresponding to increasing layer altitudes above the telescope. In each panel, the covariance values are normalised relative to the value for $\delta i = 0$ and $\Delta = 0$.

uncertainty of the simulation approach.

From figures 5.4 and 5.5 it can be seen that the width of the covariance function in the longitudinal direction drops more rapidly with increasing spatial offset than for the transverse direction. Furthermore the difference between the L and T functions increases as the outer scale decreases or as the power law coefficient β decreases – as the power spectrum deviates from the Kolmogorov case, the width of the L functions decreases more rapidly than for the T functions. Similar sets of covariance functions can be produced for the von Karman and generalized spectra by adjusting the values of β and L_0. Hence in practice it may be difficult to distinguish which of the two models is more applicable.

The calculated impulse response functions are for the high light level case (zero centroid measurement noise). Centroiding noise resulting from shot noise and detector read-out noise in the WFS images will produce a small, but not always negligible, bias of the measured cross-covariance. Before subtraction of the mean slope the cross-covariance functions are not biased by shot noise, since the noise is statistically independent for different subapertures and reference stars. Subtracting the mean tilt adds a constant bias to the cross-covariance, equal to the centroid noise variance for a single subaperture divided by the number of valid subapertures in the WFS array. In typical conditions the noise variance is of the order 10% of the total centroid variance, so that the bias on the cross-covariance is $\sim$ 0.2% of the total centroid variance for the Meade-based SLODAR system. The centroid noise variance and hence the cross-covariance bias level can be estimated from the shape of the auto-covariance function (see section 5.3.4).

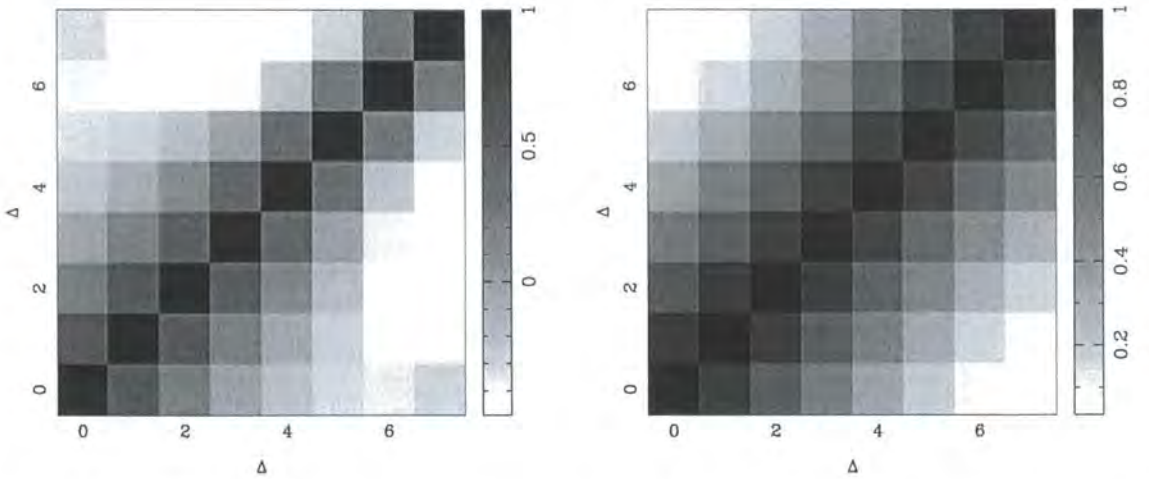

Figure 5.6: SLODAR theoretical impulse response function orthogonality plots for Kolmogorov turbulence. *Left:* longitudinal (L), *right:* transverse (T).

5.3 Estimation of the turbulence profile

5.3.1 Profile fitting

The impulse response functions that have been determined above are close to orthogonal (see figure 5.6). Thus, assuming the spatial power spectrum of the turbulence does not vary as a function of altitude, the vertical profile can be estimated by multiplying the generalized (least squares) inverse of the matrix of response functions by the measured centroid cross-covariance.

In the event that the turbulence power spectrum varies significantly with altitude, a simple least squares fit does not work. If a single turbulent layer is characterised by a different power spectrum to that of the rest of the turbulence, assuming a global power spectrum means that fitting of that layer introduces errors into adjacent altitude bins. For example if the single layer has relatively more power on shorter spatial scales than the other turbulent layers (i.e. a smaller outer scale, L_0, or a smaller value for β, depending on the model being used) the "true" impulse response function for the layer will be narrower than that used for the fit. As a result, less turbulence will be measured in the bins immediately above and below the one containing the layer – indeed, if these bins contain little or no turbulence, unphysical

negative values ("side-lobes") for C_n^2 can be observed. Conversely, if a single layer should exist with a larger outer scale (or larger value for β) than the rest of the atmosphere, the fitted response function for that layer will be too narrow and the layer's C_n^2 will be "smeared" into the adjacent altitude bins.

A very high order SLODAR system (e.g. a 30×30 subaperture WFS on a large telescope) could be used to simultaneously measure both the turbulence strength and spatial power spectrum as a function of altitude. The high spatial resolution would allow the turbulent layers to be resolved well enough that each peak in the cross-covariance could be fitted with a separate value for L_0 (or β). The ESO portable (8×8) system does not have sufficient resolution for this technique to be applied, so a single global value is assumed for L_0 or β (with this value being determined by a fit to the centroid auto-covariance for one of the stars – see section 5.3.4) and the profile fitted by the inverse matrix multiplication method mentioned above. Strong layers with significant negative C_n^2 values in adjacent altitude bins have been observed, indicating that variations in the power spectrum with altitude are not uncommon.

Examples of data recorded with the ESO portable SLODAR system (8×8 subapertures on a 40 cm telescope) and with a SLODAR system at the 4.2m William Herschel telescope (12×12 subapertures) are shown in figure 5.7. The generalized power spectrum was used to fit the data. Best-fit lines are shown for the auto-covariance and cross-covariance (section 5.3.4 explains the apparent discrepancy in the auto-covariance fits at $\Delta = 0$). For the ESO system example the best fit was obtained for $\beta = 3.33$. For the WHT example the broken line shows the best fit obtained when the value of β was assumed to be the same for all altitudes, yielding a best-fit value of $\beta = 3.45$. In this case an improved fit could be obtained, for the same resulting turbulence profile, by reducing the value of β for the profile bin centred at zero altitude *only* to 3.25. Hence in this case there is evidence that the lowest altitude turbulence (including surface-layer turbulence and any dome and mirror turbulence) is characterised by a spatial spectrum with a shallower slope

than for the higher altitude turbulence.

Error bars show the statistical uncertainties estimated by dividing each data set into ten sub-samples and measuring the resulting standard error of the scatter of the covariance and fitted turbulence profile values.

5.3.2 Statistical uncertainty of the measured profile

The statistical uncertainty on the C_n^2 profile measurements depends on the number of independent samples of the turbulence. Providing the C_n^2 profile changes over considerably longer timescales than the timescale of a single profile measurement, the uncertainty is expected to decrease as the square root of the number of independent samples. The number of "independent samples" in a given series of WFS measurements of a certain layer depends on the velocity of the layer – a high velocity layer will result in a smaller uncertainty on the measurement of its strength than a low velocity layer measured for the same length of time.

The uncertainty is larger for the higher-altitude bins because a smaller number of subapertures are included in the cross-covariance calculation. For example, for the pupil geometry illustrated in figure 5.3, the lowest-altitude bin ($\Delta = 0$) is sampled by all 48 subapertures but the highest-altitude bin ($\Delta = 7$) is effectively sampled by only 4 subapertures.

A more detailed discussion (and example simulations) can be found in Butterley et al. (2006b).

5.3.3 Altitude resolution

The altitude resolution of SLODAR is essentially limited by the number of subapertures, as described in section 5.1. The maximum sensing altitude is roughly D/θ (where D is the telescope pupil diameter and θ is the separation of the binary) and the number of altitude bins between the ground and the maximum sensing altitude is equal to the number of subapertures across the pupil (refer to figure 5.1 for il-

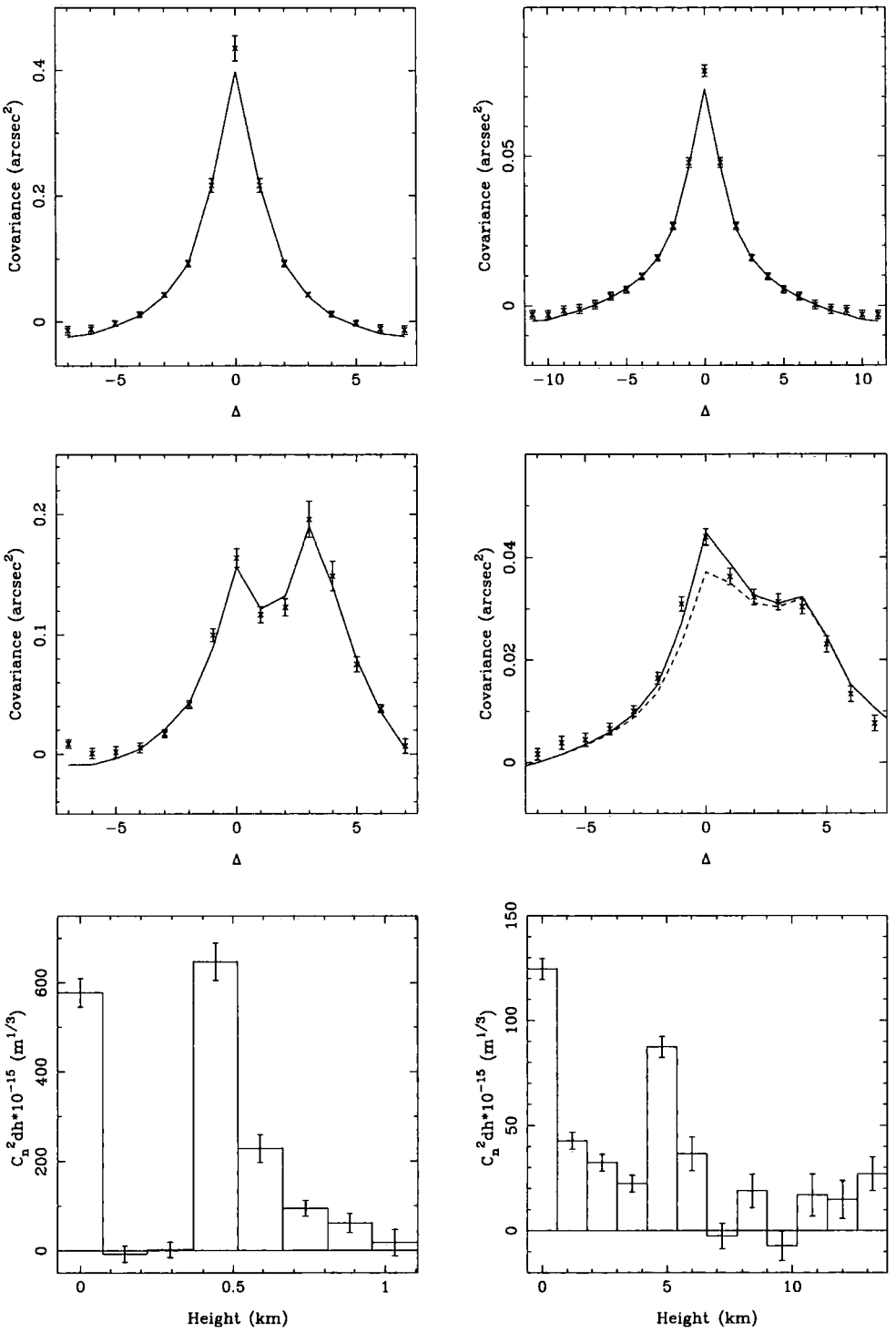

Figure 5.7: Example measured auto-covariance (top panels) and cross-covariance functions (middle panels) with the ESO portable SLODAR system at Cerro Paranal (left) and a SLODAR system at the William Herschel telescope. Solid and broken lines show fits of the theoretical covariance functions (see section 5.3.1).The bottom panels show the optical turbulence profile estimate in each case. The data correspond to a single WFS sample sequence in each case, of duration 15 seconds for the ESO system and 30 seconds for the WHT example.

lustration). The first altitude bin is centred at the ground and so has an effective thickness of $\delta h/2$ rather than δh.

In the absence of statistical noise (i.e. when a measurement is based on a very large number of turbulence measurements) a thin turbulent layer at the centre of an altitude bin is measured by SLODAR as being entirely contained within that bin. For example, a single layer at an altitude of $2\delta h$ will produce a C_n^2 profile that is positive in the $\Delta = 2$ bin but is zero everywhere else.

A layer that is above or below the centre of an altitude bin will be observed to "spill over" into the bin above or below, respectively, depending on how far from the centre of the bin it is. A layer at the interface between two altitude bins will produce a profile in which that layer's C_n^2 is equally divided between the two bins. For example, a profile consisting of a single turbulent layer at an altitude of $2.5\,\delta h$ produces a profile with equal positive C_n^2 values (each equal to 1/2 the C_n^2 in the layer) in the $\Delta = 2$ and $\Delta = 3$ bins and zero values in the other bins.

Thus for two thin turbulent layers to be completely resolved, it is necessary that they be separated in altitude by at least $2\delta h$.

5.3.4 Noise

As mentioned earlier, the SLODAR technique is relatively insensitive to photon noise. The information used to derive the turbulence profile all consists of either cross-covariances between centroid measurements from different subapertures or between centroid measurements of different star images formed through the same subaperture. The photon noise in an image of a particular star formed through a particular subaperture is statistically independent of the photon noise in images of different stars or those formed through different subapertures. If global tip and tilt were not subtracted, the cross-covariance function would be entirely independent of photon noise. Since tip/tilt subtraction is carried out, a constant bias is introduced into the cross-covariance but this is at a very low level – typically $\sim 0.2\%$ for the

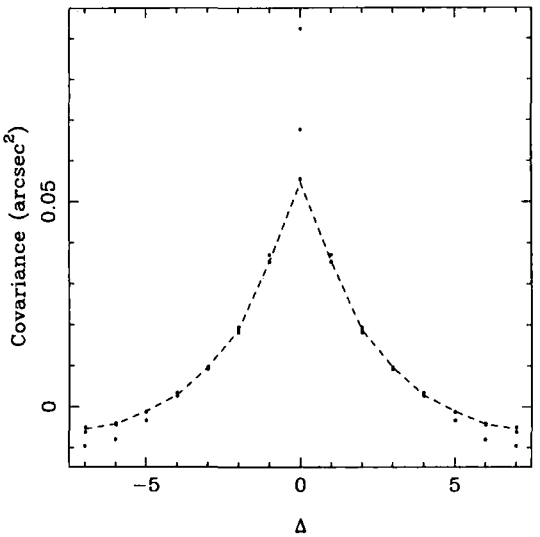

Figure 5.8: Demonstration of the method for estimation of the atmospheric and measurement noise contributions to the centroid variance, for simulated data. The points show the measured centroid autocovariance for three different levels of photon noise. Only the central point is significantly affected by the noise level.

Meade-based 8 × 8 subaperture system.

If the total atmospheric turbulence is to be measured from a SLODAR system in addition to the turbulence profile then the photon noise needs to be measured. This can be achieved by a method similar to that suggested by Nicholls et al. (1995) or Rao et al. (2002) for the generalized turbulence power spectrum. A theoretical autocorrelation function is fitted to the measured centroid autocorrelation for one of the stars, but excluding the central point (the only point affected by photon noise) from the fit, as shown in figure 5.8. The difference between the fitted and measured values for the central point is a measure of the centroid variance due to photon noise. For a more detailed discussion see Butterley et al. (2006b).

5.4 Effects of scintillation on SLODAR

On a large telescope ($\sim$ 1 m or larger) the WFS subaperture size in a SLODAR system is usually sufficiently large for scintillation effects to be averaged out (typically the intensity variance for 10 cm subapertures is $< 10\%$). However, when a small

WFS subaperture size is used, significant scintillation effects can be observed in the presence of strong high-altitude turbulence.

The ESO portable SLODAR is sensitive to scintillation, being an 8×8 subaperture WFS on a 40 cm telescope. In its usual mode of operation the instrument observes a wide binary with a separation of approximately 1 arcmin, thus profiling roughly the first kilometre of the atmosphere with 100–150 m resolution. The (sensed) turbulence in the first kilometre is too low to produce significant scintillation, although scintillation due to higher-altitude (unsensed) turbulence is still observed.

The instrument has an alternative mode of operation in which a close binary (with a separation of 6–7 arcmin) is observed, allowing the entire atmosphere to be profiled with much coarser altitude resolution. In this situation, any scintillation observed is the result of a turbulent layer that is also "directly" sensed via local wavefront slope measurements.

A physical optics propagation simulation was used to investigate the effects of scintillation on SLODAR. The simulation consists of an atmosphere model and a WFS model. The atmosphere is modelled as one or more Kolmogorov phase screens at specified altitudes, with the Fresnel propagator being used to simulate the propagation of light from the topmost layer down to the ground. The Fresnel propagation is implemented as described in Ellerbroek and Cochran (2002); the wave optics propagation between phase screens (and from the lowest phase screen to the ground) is modelled as the spatial filtering operation

$$U_{n+1}(\mathbf{x}) = \mathcal{F}\left[\exp(i\pi\kappa^2\lambda z)\mathcal{F}^{-1}[U_n(\mathbf{y})\exp(i\Phi_n(\mathbf{y}))]\right](\mathbf{x}). \tag{5.15}$$

Here U_n is the complex optical field immediately before interacting with the phase screen $\Phi_n(\mathbf{y})$, where n is the layer number; $n = 1$ is the highest layer. $\mathcal{F}$ represents a two-dimensional spatial Fourier transform, λ is the wavelength and z is the vertical

distance between layers n and $n+1$. The complex optical field U_n is

$$U_n(\mathbf{x}) = a_n(\mathbf{x}) \exp(i\phi_n(\mathbf{x})) \tag{5.16}$$

where $a_n(\mathbf{x})$ is the amplitude and $\phi_n(\mathbf{x})$ is the phase of the light. Care must be taken in implementing optical propagation simulations using equation 5.15 – it is important to ensure the optical field U_n has adequate spatial sampling (see e.g. Lawrence (1992)).

Two paths through the atmosphere are simulated for the binary target, and each path is modelled at several wavelengths (500, 550, 600 and 650 nm). The WFS is simulated by slicing the optical field at the telescope pupil into subapertures and generating a PSF for each subaperture via a 2-dimensional FFT. Photon noise and read noise are not included – the target binary is assumed to be bright. The subaperture PSFs for the four wavelengths are averaged (with equal weighting) and centroided, and the centroid autocovariance and cross-covariance are calculated. C_n^2 profiles are then fitted to the centroid cross-covariance as described in section 5.3.1.

A purely geometrical simulation (which was identical to the propagation simulation apart from the lack of physical optics propagation) was used to provide a baseline for comparison – this represents the "ideal" scintillation-free case which was the basis for the theoretical impulse response function derivation in section 5.2.

Two cases were simulated – firstly, a single turbulent layer with $r_0 = 20$ cm was simulated at different altitudes (thus with different amounts of scintillation) in order to determine the effect of scintillation induced by a layer on that layer's own impulse response function. Secondly, a series of 2-layer atmospheres were simulated in order to determine the effect of scintillation induced by a high layer on the measurement of a low layer. The first layer was placed at the ground and the altitude of the second layer was varied. A turbulence strength of $r_0 = 20$ cm was used for each layer (so $r_0 = 13.2$ cm for the two layers combined).

The results of the single layer geometrical and propagation simulations are shown

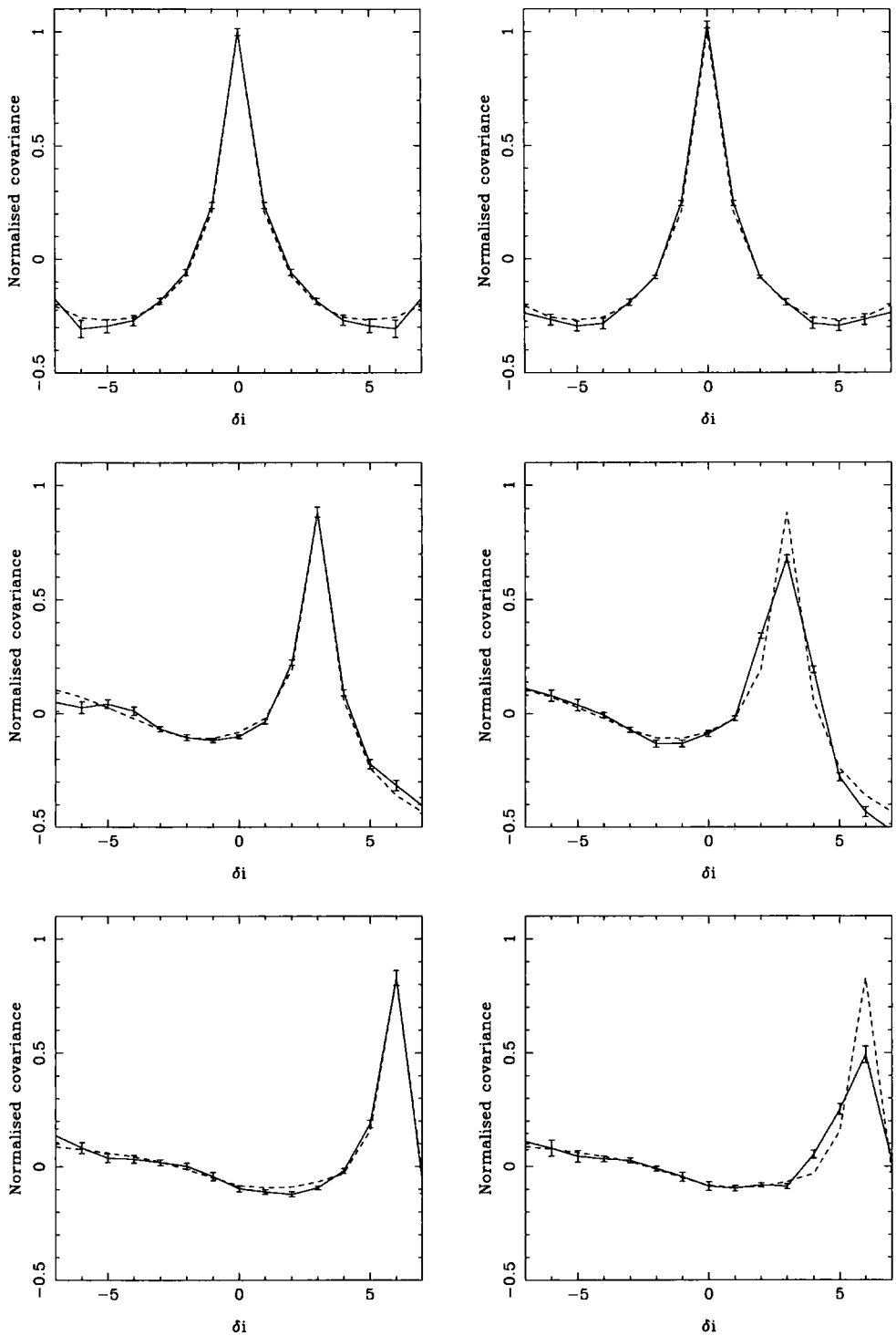

Figure 5.9: SLODAR longitudinal (L) centroid cross-correlations from (*left*) a geometrical simulation and (*right*) a propagation simulation for a single turbulent layer at (*from top to bottom*) 0 km, 6 km and 12 km. Theoretical response functions are also plotted (broken lines).

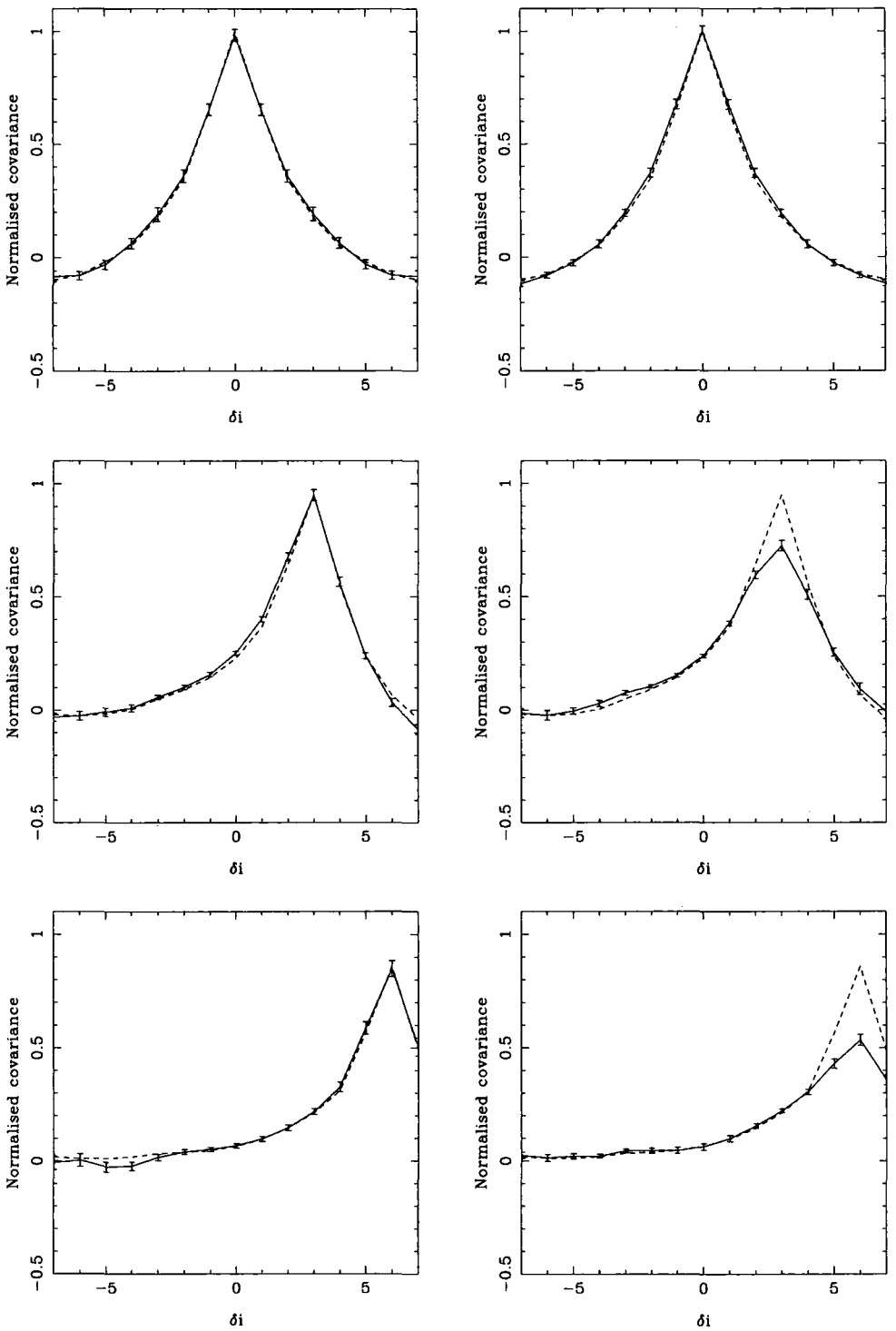

Figure 5.10: SLODAR transverse (T) centroid cross-correlations corresponding to the L cross-correlations plotted in figure 5.9.

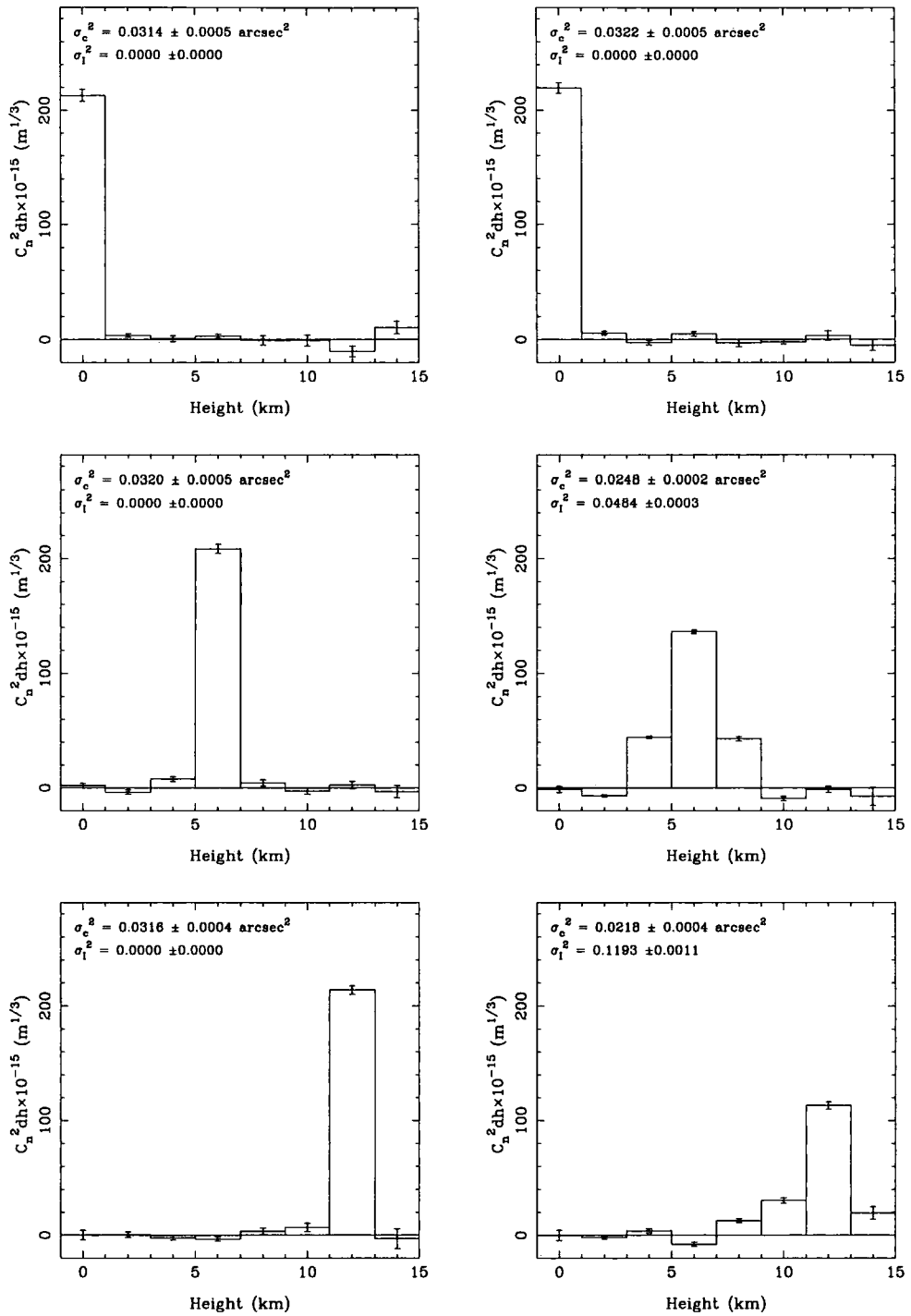

Figure 5.11: Simulated C_n^2 profiles from (*left*) a geometrical simulation and (*right*) a propagation simulation for a single turbulent layer, $r_0 = 20$ cm, at (*from top to bottom*) 0 km, 6 km and 12 km. The plots are labelled with the centroid variance, σ_c^2, and the scintillation index, σ_I^2, measured in each simulation.

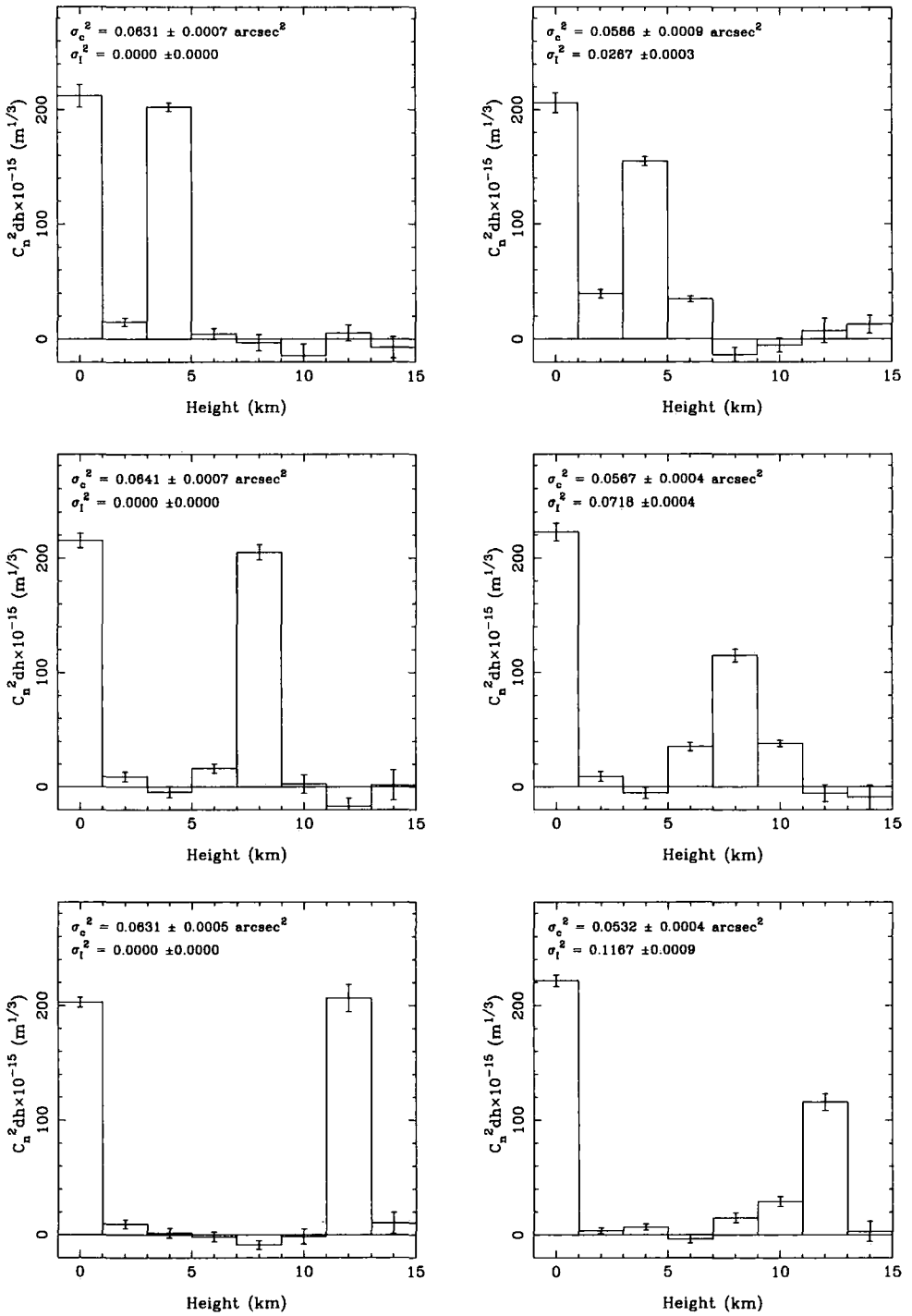

Figure 5.12: Simulated C_n^2 profiles from (*left*) a geometrical simulation and (*right*) a propagation simulation for two turbulent layers – one at the ground (0 km) and another at (*from top to bottom*) 4 km, 8 km and 12 km. r_0 for each layer is 20 cm; total r_0 = 13.2 cm. The plots are labelled with the centroid variance, σ_c^2, and the scintillation index, σ_I^2, measured in each simulation.

in figures 5.9 to 5.11. Figures 5.9 and 5.10 show the simulated centroid cross-covariances (L and T, respectively) resulting from a single turbulent layer at different altitudes. As would be expected, the cross-covariances from the geometrical simulation are in good agreement with the corresponding theoretical response functions for each altitude. The agreement is not perfect, however, and this is probably an effect of the outer scale introduced by the finite size of the phase screens in the simulation. The cross-covariances from the propagation simulation are also in good agreement for low altitude layers (with little scintillation) but the agreement deteriorates with increasing layer altitude. The response functions become broader and the amplitude of the peak smaller as the amount of scintillation increases.

The C_n^2 profiles fitted to the cross-covariances shown in figures 5.9 and 5.10 are plotted in figure 5.11. The C_n^2 profiles for the geometrical simulations have a single well-defined peak at the correct altitude and very little turbulence measured elsewhere. It should be noted that some of the non-zero turbulence values at other altitudes are slightly larger than the error bars – this is a result of the small unexplained discrepancies between the theoretical response functions and those measured from the geometrical simulation. The propagation simulation results are significantly different – low-level turbulence is correctly sensed but higher (scintillation-inducing) turbulence is "smeared" into neighbouring altitude bins. This is consistent with the scintillated response functions being broader than the theoretical functions as described above.

The observed centroid variance is seen to decrease as the scintillation index increases – this is a known effect (Tokovinin, 2002). As a result, the total turbulence strength (e.g. measured via Zernike fitting) will be underestimated.

Figure 5.12 shows the fitted C_n^2 profiles for the two-layer simulations. As before, the C_n^2 profiles for the geometrical simulation match the "true" profile apart from some minor discrepancies attributed to differences between the measured and theoretical response functions. In the profiles from the propagation simulation the high

layer is smeared into adjacent bins as in the single layer simulation. The ground layer, however, is fully measured in the correct bin, irrespective of the altitude of the higher layer. Thus the fact that the light sensing the ground layer is scintillated does not affect its measurement.

The results above show that scintillation only affects SLODAR turbulence profiling when the scintillation is induced by turbulence within the instrument's direct sensing range. Scintillation caused by turbulence above the instrument's range reduces the measured value of the total seeing, resulting in an underestimation of the unsensed turbulence, but does not affect the turbulence strength measured in each altitude bin. Thus it is reasonable to use a SLODAR instrument with small subapertures with a wide binary target to profile the ground layer of turbulence (below $\sim$1 km). Observing a narrow binary target to profile the whole atmosphere with such an instrument will not be a robust technique unless scintillation effects are taken into account.

It may be possible to develop a means of including subaperture intensity information in the data processing in order to correct for the effect of scintillation – the methods used for analysing SCIDAR data would be the starting point for this. However, the increase in complexity of the analysis could potentially compromise one of SLODAR's strengths – that the data can be analysed very quickly and the profile seen almost in "real time".

5.5 Conclusions

The response of a SLODAR (Shack-Hartmann) optical turbulence profiling system to a thin turbulent layer, in terms of the cross-covariance function of the wavefront slopes for a double star target, can be calculated as a function of the layer altitude and the spatial structure function of the phase aberrations. The theoretical response functions can be used to provide a robust determination of the optical turbulence

profile via a fit to the spatial cross-covariance of the measured centroid data.

A SLODAR system with small subapertures ($\lesssim$ 10 cm in typical conditions) is sensitive to scintillation. Providing the system's maximum sensing range is low enough that directly-sensed turbulent layers do not induce significant scintillation, such a system still measures $C_n^2(h)$ correctly within this range. However, scintillation due to turbulence at higher altitudes will cause the total turbulence strength to be under-estimated.

Chapter 6

SLODAR using a 1-dimensional wavefront sensor: "SLOTDAR"

In this chapter I describe a previously unpublished variation on the SLODAR technique which allows the altitude resolution to be optimised depending on the brightness of the target.

6.1 Introduction

In its simplest form, a SLODAR system would consist of a single row of subapertures aligned along the direction of the separation of the binary source. Such a system would be capable of sensing turbulence strength as a function of altitude but would not be able to sense the velocities of the turbulent flow unless the layers happened to be moving along the line of subapertures. In practice the subapertures of a SLODAR WFS usually populate the full (circular) telescope aperture to maximise the sampling efficiency and to allow two dimensional cross-covariances with temporal offsets to be used to measure the velocities of turbulent layers.

As described in chapter 5, the light level requirement of a SLODAR system is broadly that in each integration, each subaperture must collect enough photons for the subaperture image to be accurately centroided. As the configuration of a

system (subaperture size and, to some degree, exposure time) is typically fixed, this implies a limiting magnitude for the targets. Targets significantly brighter than the limiting magnitude deliver much higher photon counts than are necessary, thus the extra light is effectively wasted – if the system was reconfigurable then the spatial sampling could be optimised to achieve the best possible altitude resolution for a given light level.

The concept described in this chapter is a variation on the Shack-Hartmann based SLODAR technique which allows the system sampling to be optimised for photon noise. This is achieved using a one-dimensional wavefront sensor – i.e. a wavefront sensor that measures the wavefront gradient in only one direction.

6.2 Description of the SLOTDAR technique

The basic concept of SLOTDAR (Slope Detection and Ranging through a slot), first suggested by Wilson (2005), is illustrated in figure 6.1. A binary target is observed through a rectangular (slot-shaped) aperture, with the separation of the binary components aligned along the length of the slot. The target is imaged using a cylindrical lens positioned in a (demagnified) pupil plane, so that the images of the two stars will be a pair of fully separated (end-to-end) parallel lines on the CCD. Wavefront aberrations induce perpendicular deviations of the lines which can be measured by centroiding regions of the lines (in the transverse direction). The length of the region along which the line image is binned for centroiding, w, is chosen to be sufficient to overcome noise effects while maximising the spatial resolution. As in Shack-Hartmann based SLODAR, the spatial cross-covariance of the local centroid measurements is used to derive the turbulence profile.

Telescope apertures are usually circular and masking off most of a circular pupil to leave a rectangular slot is wasteful of light. However, the same method is easily applied to a full circular aperture in the same way as conventional SLODAR, by

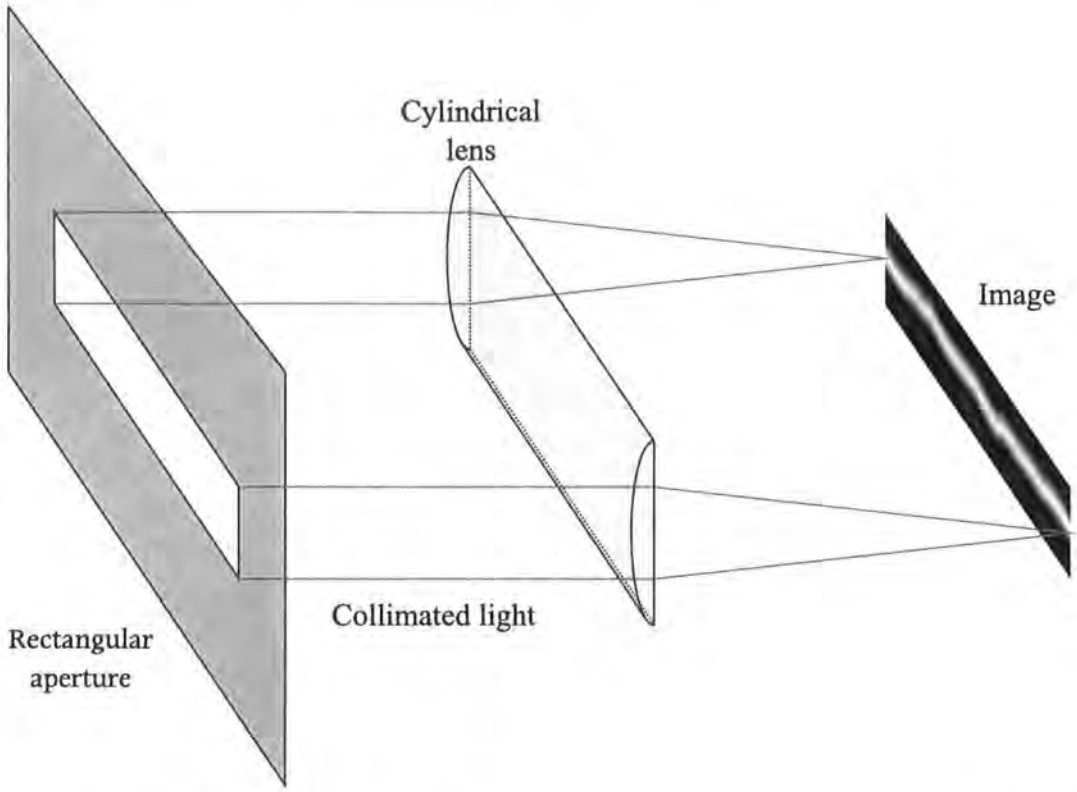

Figure 6.1: Simplified overview of the 1-dimensional wavefront sensor used for the SLOTDAR technique. Light is collected through a slot-shaped aperture and focused in the direction perpendicular to the orientation of the slot. In practice the slot would be the aperture of a telescope (with an appropriate pupil mask) and the cylindrical lens would be positioned at a telescope pupil image. The diagram only shows light from one star, although two stars need to be imaged with their separation oriented along the length of the slot. The separation of the stars must be sufficiently wide for the two images to be completely separated.

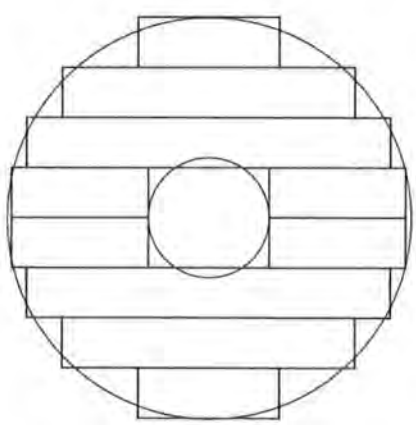

Figure 6.2: Pupil geometry for making full use of an annular telescope pupil with the SLOTDAR technique.

filling the pupil with an array of parallel slots as shown in figure 6.2, thus increasing the area of turbulence that is simultaneously sampled. This can be achieved by replacing the cylindrical lens with a cylindrical lenslet array (a series of parallel cylindrical micro-lenses) with an appropriate pitch. In addition to improved sampling, this configuration allows two-dimensional cross-covariances to be calculated, albeit with different spatial sampling in the x- and y-directions, allowing layer velocities to be measured. However, the work presented here is limited to the single-slot case in order to simplify the analysis.

In addition to the ability to tune the resolution of the instrument to the brightness of the target, SLOTDAR offers a further benefit. In conventional SLODAR the telescope pupil is effectively sliced into subapertures in both the x- and y-directions. In SLOTDAR, the pupil slicing is only "hard-wired" in the direction perpendicular to the separation of the binary. The averaging in the longitudinal (L) direction can be carried out in software so, rather than simply slicing the line into segments, it is possible to carry out a boxcar average along the line. Extra spatial information is thus obtained. In particular this allows the altitude of thin turbulent layers which are sufficiently well separated in altitude to be measured considerably more precisely than is possible with a SH WFS (see section 5.3.3).

The most notable disadvantage of the SLOTDAR technique as compared to conventional SLODAR is that local wavefront tilts are only measured in the direction transverse (T) to the separation of the binary target. As shown in figures 5.4 and 5.5, the peaks of the T impulse response functions are considerably broader than those of the L functions, thus the altitude resolution is expected to be considerably coarser than would be possible if the L functions were available.

One other minor drawback in the technique is in global tip/tilt subtraction. The global tilt in the T direction is subtracted simply by subtracting the average T centroid. In the L direction, however, global tilt has the effect of moving the entire line image longitudinally. It is important to know the precise longitudinal

positions of the lines for the two stars so that the cross-covariance is calculated with the correct zero point. In the presence of scintillation and/or photon noise there is inevitably some uncertainty in the L position of the lines, which is manifested as a "smearing" of the cross-covariance function (after averaging over many exposures), thus reducing the spatial resolution. In the case of a single slot (as in figure 6.1) only two points (the ends of the line) are available to locate each WFS image. For a fully populated pupil the entire pupil geometry can be used to impose tighter constraints on the L image position. In the case of the geometry shown in figure 6.2 there are 20 "line ends", so the reduction in the error in the position is likely to be of the order $\sqrt{10} \approx 3.2$.

6.3 The theoretical impulse response for SLOTDAR

The derivation of the theoretical impulse response functions for SLODAR in section 5.2 can be modified to calculate the equivalent functions for SLOTDAR. The main differences are that the tilt covariance calculations need to be generalized to non-square subapertures (to account for the variable binning width w) and the impulse response functions evaluated for subaperture separations which are not integer multiples of the subaperture size. Only the simplified single-slot geometry shown in figure 6.1 is considered here, so that only covariances between regions with a spatial offset in the x-direction need be considered. Extending the treatment to two dimensions for the full-pupil geometry (figure 6.2) is not difficult.

The Zernike tilt (or Z-tilt, cf. G-tilt) coefficient in the transverse/y-direction, for a rectangular aperture centred at u (viewing the first star), is given by

$$z_u = \int_{\frac{-w}{2}}^{\frac{w}{2}} \mathrm{d}x \int_{\frac{-d}{2}}^{\frac{d}{2}} \mathrm{d}y \phi(\mathbf{r}) \alpha y \tag{6.1}$$

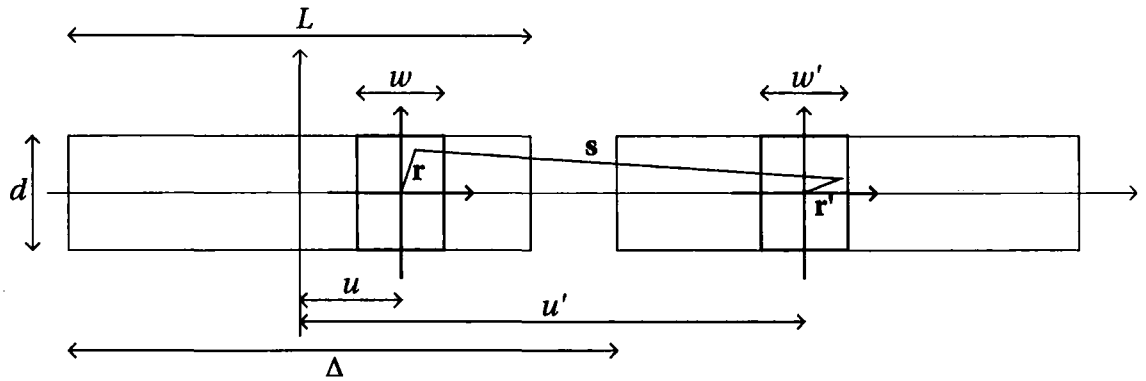

Figure 6.3: Geometry for the calculation of wavefront slope covariances in SLOTDAR. The projections of the two slots are shown as fully separated ($\Delta > L$) for clarity, but we are actually interested in the regime where $\Delta < L$.

where $\phi(\mathbf{r})$ is the wavefront phase aberration, $\mathbf{r} = (x, y)$ is a spatial coordinate with its origin at the centre the aperture and α is a constant defined such that

$$\int_{\frac{-w}{2}}^{\frac{w}{2}} \mathrm{d}x \int_{\frac{-d}{2}}^{\frac{d}{2}} \mathrm{d}y \phi(\mathbf{r}) \alpha^2 y^2 = 1, \tag{6.2}$$

hence

$$\alpha = \sqrt{\frac{12}{wd^3}}. \tag{6.3}$$

The tilt in radians is given by

$$g_u = \frac{\alpha\lambda}{2\pi} z_y. \tag{6.4}$$

So the (Zernike) tilt in radians is given by

$$g_u = \frac{6\lambda}{\pi w d^3} \int_{\frac{-w}{2}}^{\frac{w}{2}} \mathrm{d}x \int_{\frac{-d}{2}}^{\frac{d}{2}} \mathrm{d}y \phi(\mathbf{r}) y. \tag{6.5}$$

Similarly, the tilt for a second aperture centred at u' with the same height, d, but not necessarily of the same width, w', viewing the second star is

$$g_{u'} = \frac{6\lambda}{\pi w' d^3} \int_{\frac{-w'}{2}}^{\frac{w'}{2}} \mathrm{d}x' \int_{\frac{-d}{2}}^{\frac{d}{2}} \mathrm{d}y' \phi'(\mathbf{r}') y'. \tag{6.6}$$

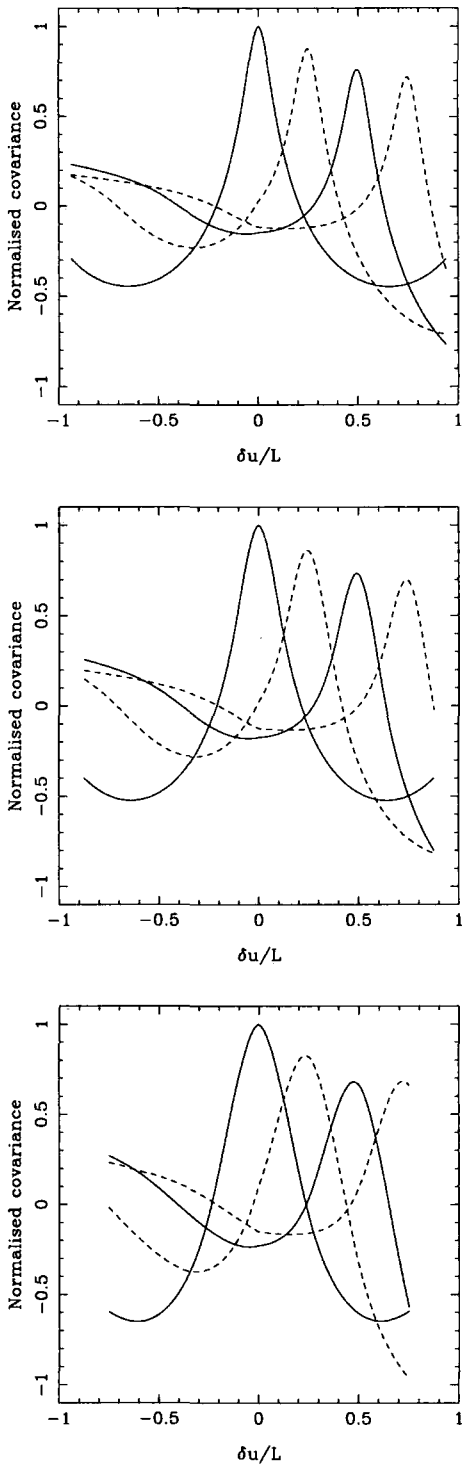

Figure 6.4: Normalised SLOTDAR theoretical impulse response functions for Kolmogorov turbulence and for a single-slot geometry as shown in figure 6.1. Slot width $d = L/8$. From top to bottom, $w = d/2$, $w = d$, $w = 2d$. Each plot shows response functions for $\Delta = 0$, $d/4$, $d/2$ and $3d/4$ corresponding to increasing layer altitudes above the telescope. In each panel, the covariance values are normalised relative to the value for $\delta x = 0$ and $\Delta x = 0$.

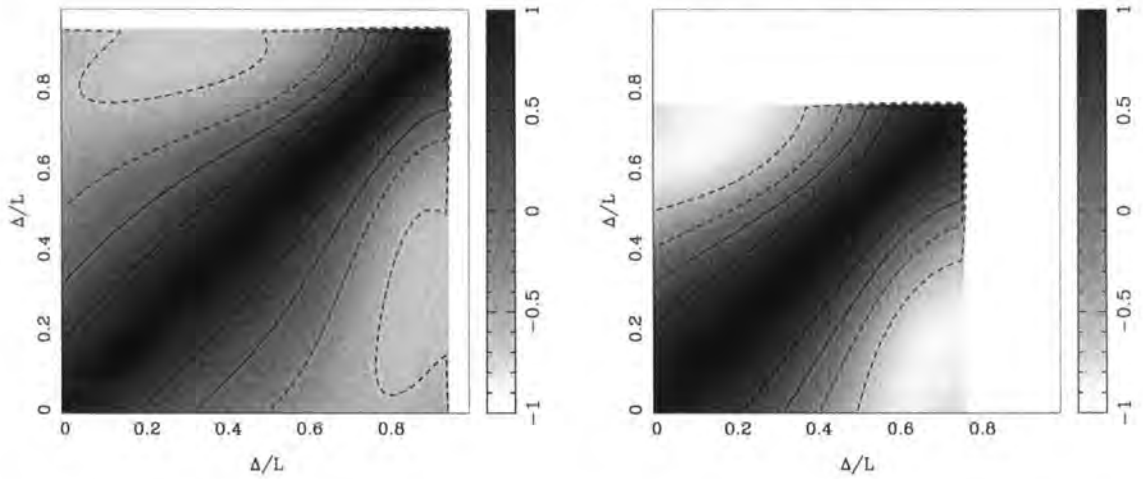

Figure 6.5: SLOTDAR impulse response function orthogonality plots. *Left:* $d = w/2$; *right:* $d = 2w$.

The tilt covariance between two such rectangular apertures is given by

$$C = \langle g_u g_{u'} \rangle \tag{6.7}$$

$$= \frac{36\lambda^2}{\pi^2 w w' d^6} \int_{\frac{-w}{2}}^{\frac{w}{2}} \mathrm{d}x \int_{\frac{-d}{2}}^{\frac{d}{2}} \mathrm{d}y \int_{\frac{-w'}{2}}^{\frac{w'}{2}} \mathrm{d}x' \int_{\frac{-d}{2}}^{\frac{d}{2}} \mathrm{d}y' \, \langle \phi(\mathbf{r})\phi'(\mathbf{r}') \rangle \, yy' \tag{6.8}$$

where $\langle \phi(\mathbf{r})\phi'(\mathbf{r}') \rangle$ is the piston-subtracted phase covariance and is given by

$$\langle \phi(\mathbf{r})\phi'(\mathbf{r}') \rangle = -\frac{1}{2} D_\phi(\rho)$$

$$+\frac{1}{2} \int_{\frac{-w}{2}}^{\frac{w}{2}} \mathrm{d}x \int_{\frac{-d}{2}}^{\frac{d}{2}} \mathrm{d}y D_\phi(\rho)$$

$$+\frac{1}{2} \int_{\frac{-w'}{2}}^{\frac{w'}{2}} \mathrm{d}x' \int_{\frac{-d}{2}}^{\frac{d}{2}} \mathrm{d}y' D_\phi(\rho)$$

$$-\frac{1}{2} \int_{\frac{-w}{2}}^{\frac{w}{2}} \mathrm{d}x \int_{\frac{-d}{2}}^{\frac{d}{2}} \mathrm{d}y \int_{\frac{-w'}{2}}^{\frac{w'}{2}} \mathrm{d}x' \int_{\frac{-d}{2}}^{\frac{d}{2}} \mathrm{d}y' D_\phi(\mathbf{s}) \tag{6.9}$$

where

$$\mathbf{s} = (u' - u + \Delta + x' - x, y' - y). \tag{6.10}$$

As in conventional SLODAR, the mean slope is subtracted from the local slope measurements to remove telescope guiding errors and wind-shake (separately for

stars 1 and 2), again introducing a dependence of the local slope covariances on the altitude of the turbulence. The global tilt subtraction differs from that for conventional SLODAR in that, instead of averaging the local centroid measurements, the entire WFS image can be stacked in the x-direction and centroided (i.e. setting the boxcar width to $w = L$). For a turbulent layer at an altitude h, corresponding to an offset of $\Delta = h\theta$ in the x direction between the projections of the telescope pupil onto the turbulent layer for the two stars (where Δ is in units of physical length), the covariance of the slopes for two local centroids after global tilt subtraction is

$$\begin{aligned} C_{u,u'}(\Delta) &= \langle (g_u - G_0)(g_{u'} - G_\Delta) \rangle \\ &= \langle g_u g_{u'} \rangle - \langle g_u G_\Delta \rangle - \langle G_0 g_{u'} \rangle + \langle G_0 G_\Delta \rangle \end{aligned} \tag{6.11}$$

where G_0 and G_Δ are the global slopes for stars 1 and 2 respectively. The response of SLOTDAR to a turbulent layer at altitude h is given by averaging over all pairs of subaperture positions u and u' for a given spatial separation $\delta u = u' - u$. Thus the impulse response functions are described by

$$X(\Delta, \delta u) = \frac{2}{2L - 2w - \Delta} \int_{(w-L)/2}^{(L-w-\Delta)/2} C_{u,u+\delta u}(\Delta) \mathrm{d}u. \tag{6.12}$$

Note that in reality the "subaperture" separations have discrete values due to the pixelisation of the WFS image, but the above expression (for a continuous range of subaperture separations) is accurate provided that the number of pixels in the image is large.

Example SLOTDAR impulse response functions for the Kolmogorov power spectrum are plotted in figure 6.4. Broadening of the response function peaks is observed as the boxcar length w is increased. Figure 6.5 shows plots of the orthogonality of the response functions for $w = d/2$ and $w = 2d$, demonstrating the modest improvement in altitude resolution to be gained by minimising the boxcar length in high light levels (cf. equivalent plot for SLODAR, figure 5.6).

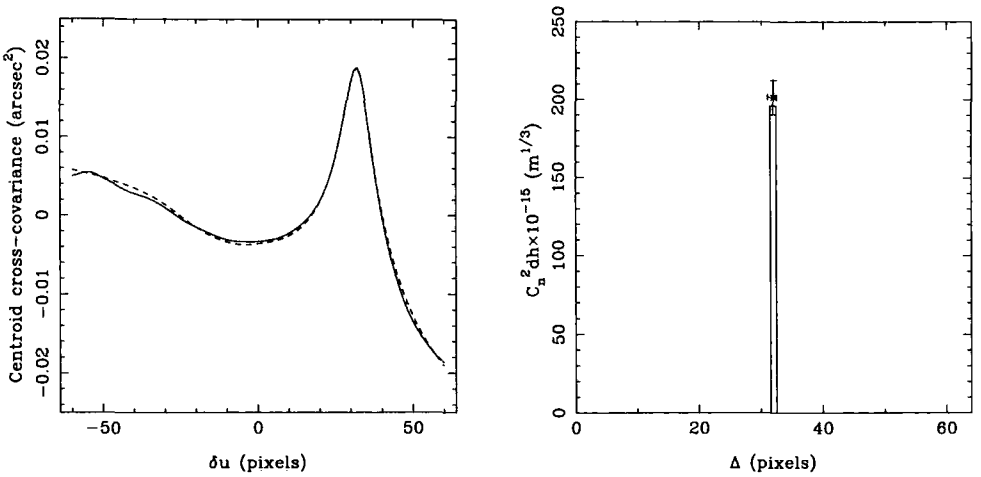

Figure 6.6: SLOTDAR simulation results for a single turbulent layer and high light level (no photon noise). *Left:* solid line: measured cross-covariance; broken line: fitted impulse response function. *Right*: C_n^2 profile. The bar indicates the "true" C_n^2. The error bars on the fitted C_n^2 show the change in the fitted parameters needed to increase the least squares difference by a factor of 2.

6.4 Geometrical simulation of SLOTDAR

A geometrical simulation of a SLOTDAR instrument has been implemented. In the simulation, the atmosphere is modelled as a series of thin Kolmogorov phase screens and the pupil phase calculated for each path through the atmosphere by summing the phase along each optical path. The WFS image is generated by carrying out a series of one-dimensional FFTs of the complex amplitude in the telescope pupil. Photon noise is then "sprayed" into the image, and a boxcar average taken in the x-direction to generate 1-dimensional PSFs which are then centroided. CCD read noise is not included in the simulation – it is assumed that an L3CCD device is used. Note that photon noise in an L3CCD device is different to photon noise in a conventional CCD – the noise level is effectively twice that in a conventional CCD as a result of the on-chip electron multiplication process (Basden et al., 2003). Since the simulation does not include physical optics propagation, the effects of scintillation are not included.

The theoretical impulse response functions derived in section 6.3 were compared to the simulation using a single-layer atmosphere and considering the high light level

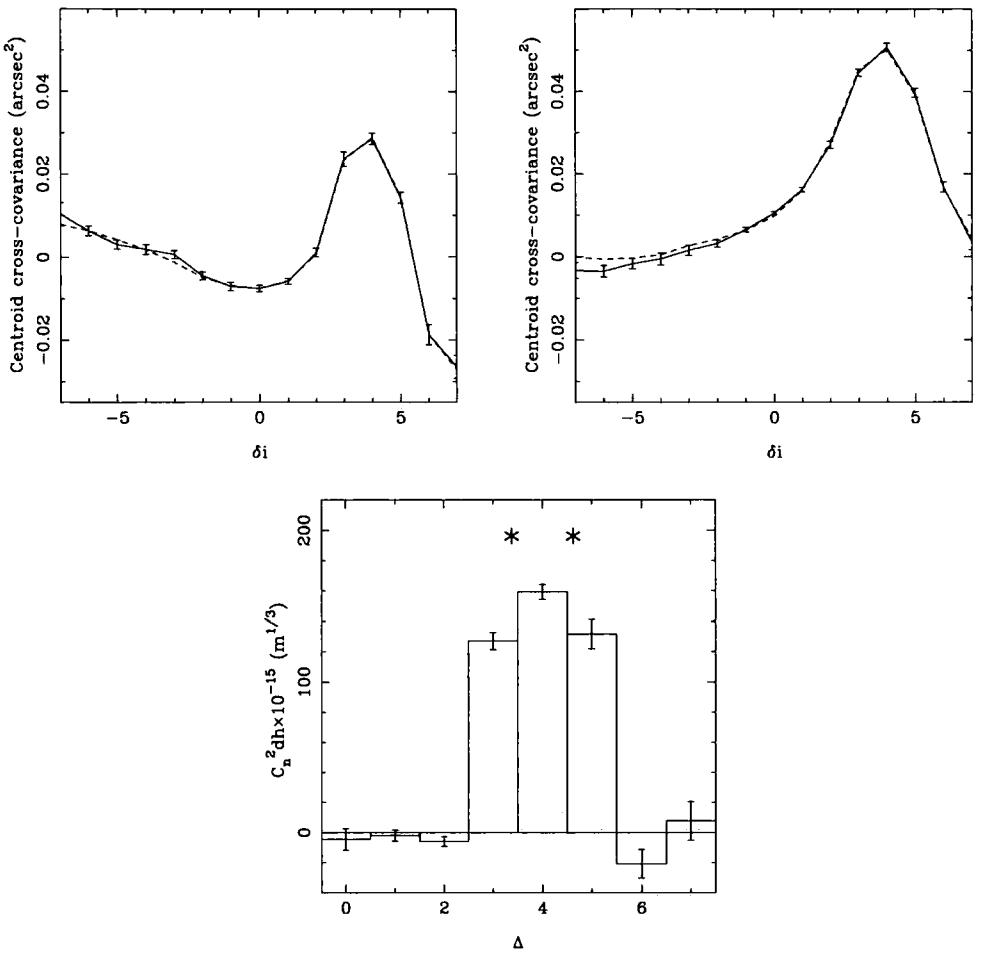

Figure 6.7: Conventional SLODAR 2-layer simulation results. High light level. *Top:* fits to cross-covariance (left: L, right: T). *Bottom:* C_n^2 profile. The stars on the C_n^2 indicate the actual altitudes and strengths of the turbulent layers.

case (i.e. no photon noise). The simulated centroid cross-covariances were found to be in good agreement with the impulse response functions. Figure 6.6 shows a sample cross-covariance measurement and the results of a least squares fit to the cross-covariance. The fit was constrained to a single layer, so two variables were included in the fit – the strength of the layer and Δ, corresponding to the layer altitude. The bar on the C_n^2 plot represents the true profile, and both the altitude and strength of the layer are within the estimated uncertainties on the fitted C_n^2.

The potential gain in altitude resolution of SLOTDAR over SLODAR was demonstrated by making a comparison between 2-layer simulations of both techniques in which the altitudes of the turbulent layers were chosen such that conventional SLO-

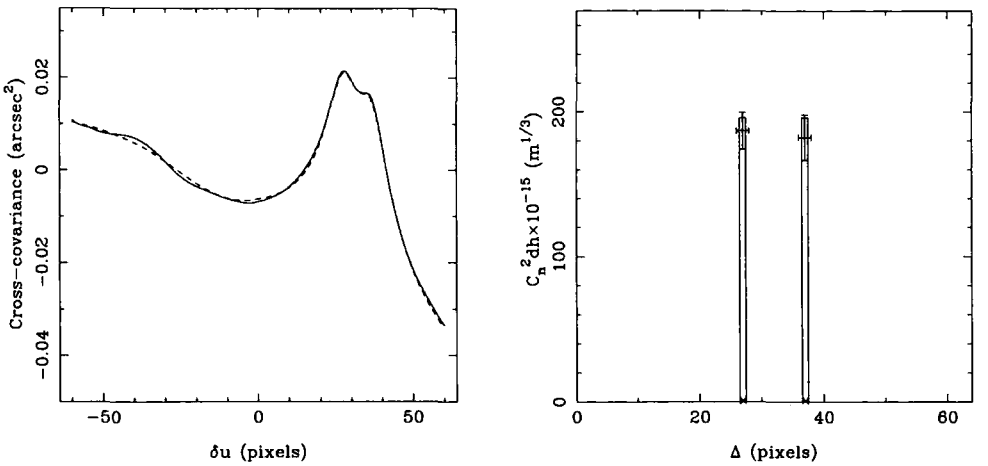

Figure 6.8: SLOTDAR in the high light level case. $w = d/2$, no photon noise. *Left:* measured cross-covariance (solid line) and fit (broken line). *Right:* fitted profile. The error bars on the fitted C_n^2 show the change in the fitted parameters needed to increase the least squares difference by a factor of 2.

DAR was not able to fully resolve them. The results of the conventional SLODAR simulation are shown in figure 6.7. The separation of the two layers is 1.25 $\times$ the width of the altitude bins, which is insufficient to produce two distinct peaks in the L or T cross-covariance functions. The turbulence strength (fitted as described in section 5.3.1) is seen to be distributed across 3 altitude bins, and it is not possible to say whether this is due to two or more thin layers or a single thick turbulent layer.

The results of the equivalent high light level case for SLOTDAR are shown in figure 6.8. The two turbulent layers are seen as distinct peaks in the centroid cross-covariance. The plotted C_n^2 profile was retrieved by making a least squares fit of a two layer atmosphere (4 parameters in total – Δ and C_n^2 for each layer). The problem of retrieving C_n^2 profiles without prior knowledge of the number of turbulent layers is not treated here. The profile fitted to the simulation results is in good agreement with the true profile.

The effect of photon noise on SLOTDAR is demonstrated in figure 6.9. The same atmosphere model was used as for the high light level case, but photon noise was included – the light level was set to 160 photons per WFS integration for each star. For a boxcar width of $w = d/2$ the 2 layers are still resolved, but the uncertainty

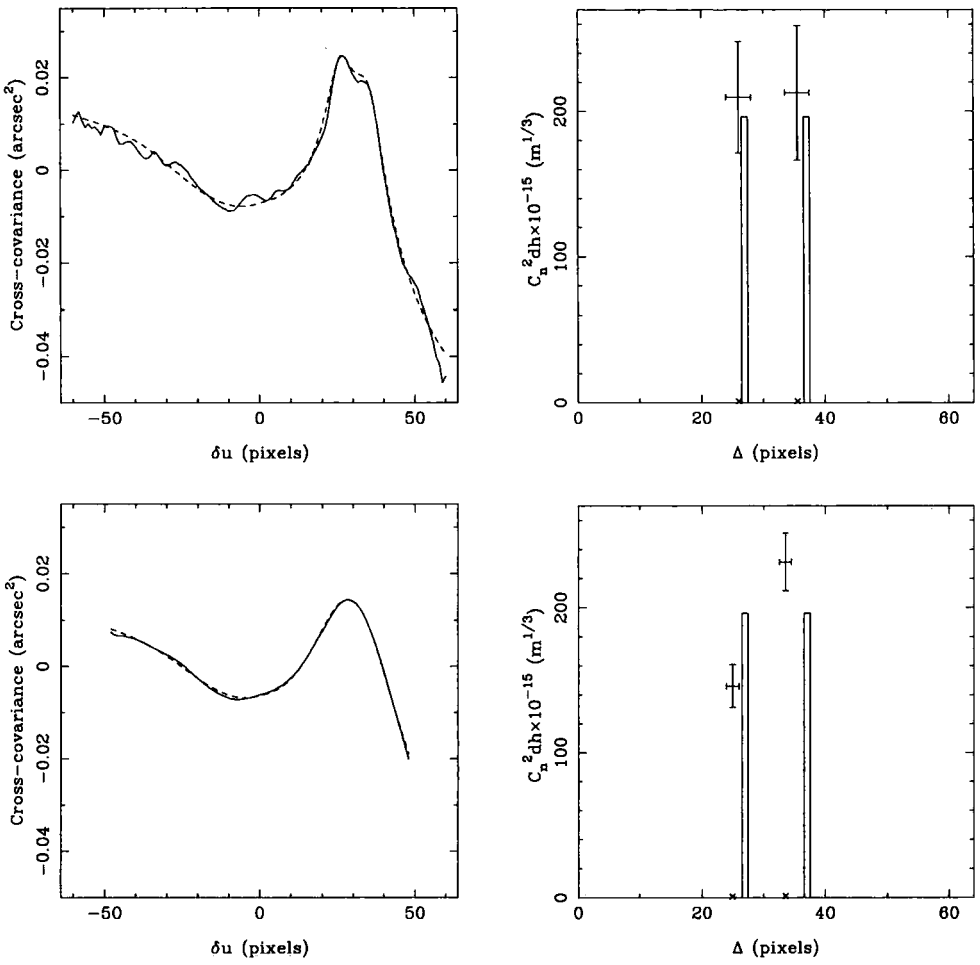

Figure 6.9: SLOTDAR with 160 photons per integration. Plots on the left show measured cross-covariance (solid line) and 2 layer fit (broken line). Plots on the right show the fitted profiles. *Top:* $w = d/2$; *bottom:* $w = 2d$. The error bars on the fitted C_n^2 show the change in the fitted parameters needed to increase the least squares difference by a factor of 2.

on the fit is larger than for the high light level case. For a boxcar width of $w = 2d$, although the effects of photon noise are reduced, the layers are no longer resolved – separate peaks are not observed in the cross-covariance. The fitted values for the layers are not in good agreement with the true profile, within the estimated uncertainties. For $w = d/2$ the impulse response functions for this layer separation are close to orthogonal, whereas for $w = 2d$ they are not (see figure 6.5). Hence for the $w = 2d$ case, the measured cross-covariance would be more appropriately fitted by a single-layer model since the data cannot support a 2-layer model.

6.5 Future work

The potential advantages of the SLOTDAR technique over conventional SLODAR have been demonstrated, but further research is needed before a practically useful SLOTDAR instrument can be implemented. In particular, considerable work is required on the extraction of the turbulence profile from the measured centroid cross-covariance. The method used for conventional SLODAR (section 5.3.1) cannot be used because the cross-covariance is sampled at much higher resolution. Hence the impulse response functions for each sampled offset are not orthogonal. Techniques exist in astronomy for deconvolution of spatially varying PSFs from AO-corrected images (Thiébaut and Conan, 1995; Conan et al., 1998; Flicker and Rigaut, 2005). Such techniques, modified for the one dimensional case, could be used as the basis for deconvolution of SLOTDAR profiles.

With the exception of the derivation of the theoretical expressions for the impulse response functions, it has been assumed here that the WFS images for the two stars would be centroided with the same boxcar length w. It is quite common in SLODAR for there to be a significant difference in the brightness of the stars in the binary target, so it would be useful to investigate the implications/benefits of using different boxcar lengths for the two stars.

The effects of scintillation on SLOTDAR can, in general, be expected to be similar to those for conventional SLODAR (section 5.4). An evaluation of the magnitude of the error in locating the WFS images in the longitudinal direction is important – this effect imposes an additional limit on the altitude resolution of the technique.

6.6 Conclusions

SLOTDAR is a variation on the SLODAR technique which allows its spatial sampling to be optimised depending on the brightness of the target binary star, without the optics being physically reconfigured. In addition, the technique allows the altitude of well-resolved turbulent layers to be estimated more accurately than is possible with conventional (Shack-Hartmann) SLODAR. In principle, the velocities of turbulent layers can also be measured as in conventional SLODAR, by using a cylindrical lenslet array instead of a single slot. Before the SLOTDAR technique can be implemented in the form of a working instrument, further work is needed on the retrieval of C_n^2 profiles from the measured centroid cross-covariances.

Chapter 7

Conclusions

The work described in this thesis addresses two important issues in implementing laser guide star adaptive optics on ELTs: focal anisoplanatism and atmospheric turbulence profiling. In this chapter I summarise the results of my work and discuss the directions future work is likely to take.

7.1 SPLASH wavefront sensing

SPLASH (Sky-Projected Laser Array Shack-Hartmann) is a laser guide star wavefront sensing technique in which the wavefront is sensed on the upward path of the light.

- The upward (wavefront sensing) path of the SPLASH laser beams has been shown theoretically to suffer considerably less from focal anisoplanatism than a conventional single-LGS arrangement.
- The performance of a SPLASH-based closed-loop AO system has been shown, by simulation, to outperform an equivalent system based on a single conventional LGS for an 8 m class telescope.
- The performance of a SPLASH system on an ELT is uncertain because an ELT-scale simulation is not currently possible due to limitations in computer

processing power. However, it is known that return-path aberrations become more significant as the aperture size is increased so a point will eventually be reached where the method fails. It is important to identify the scale at which this occurs before SPLASH can be seriously considered for use on an ELT.

7.2 Calibration of SLODAR

SLODAR (Slope Detection and Ranging) is a turbulence profiling method using a Shack-Hartmann wavefront sensor.

- The response of a SLODAR system to a turbulent layer at a given altitude has been calculated theoretically (assuming geometrical wavefront propagation) and is a function of the layer altitude and the turbulence spatial structure function.
- The C_n^2 profile can be recovered from the spatial cross-covariance of the measured centroids by multiplying with the generalized inverse of the theoretical impulse response functions.
- When implemented on a small telescope (with subaperture size $\lesssim$ 10 cm) the SLODAR technique has been shown by simulation to be susceptible to scintillation. Turbulent layers above the maximum sensing range of such a system do not bias the results but scintillation due to layers that are directly sensed prevents accurate recovery of the C_n^2 profile.

7.3 SLOTDAR

SLOTDAR (Slope Detection and Ranging through a slot) is a variation on SLODAR in which the spatial sampling can be optimised without reconfiguration of the optics.

- The "subaperture" size can be varied, according to the brightness of the target stars, to maximise the resolution in altitude while maintaining an adequate

signal-noise ratio. Unlike conventional SLODAR, spatial covariance information is only measured for image motion in the direction transverse to the separation of the binary target. The centroids are calculated using a boxcar average so that extra spatial information is measured, allowing the altitudes of well-resolved turbulent layers to be measured more accurately than in conventional SLODAR.

- As for conventional SLODAR, the theoretical response of a SLOTDAR system to a turbulent layer at a given altitude has been calculated as a function of the layer altitude and the turbulence spatial structure function.

- Due to the non-orthogonality of the response functions for small layer separations (in altitude), reconstruction of $C_n^2(h)$ from SLOTDAR data is more difficult than for conventional SLODAR data.

7.4 Future work

If SPLASH should prove to be an effective LGS technique for ELTs, the advantages it provides are most significant for single-conjugate AO. While single-conjugate AO will undoubtedly have its place in ELT astronomy, the need for high order, wide field correction will also necessitate the construction of MCAO and MOAO systems. LGS schemes for such systems currently look more likely to rely on a large number of conventional laser beacons, although other techniques such as shearing interferometry should not be discounted.

The SLODAR technique is potentially extremely useful for developing adaptive optics for ELTs. When implemented on a large (4–8 m) telescope with a large number of subapertures, SLODAR will provide a detailed measurement of the strength and power spectrum of atmospheric turbulence as a function of altitude. A campaign of observations with such a system would provide a wealth of information including the thickness of the surface layer and how closely real turbulence follows

the Kolmogorov model, which would prove invaluable in designing AO systems for ELTs.

A SLODAR system on a small telescope (< 1 m) is an ideal permanent surface layer site monitor for supporting an observatory in its operation. An 8 m class telescope with a GLAO system would benefit from the availability of a real-time ground layer turbulence profile as the performance of the system could be predicted based on the current conditions. Such a system could also be used in a supporting role for a working ELT – a ground layer turbulence profile measured alongside the ELT could provide an estimate of the turbulence within the telescope structure.

The SLOTDAR technique has not yet been demonstrated on sky and so is not proven. If a robust method of retrieving the turbulence profile from the spatial cross-covariance can be demonstrated, the technique may prove to be more appropriate than conventional SLODAR in certain circumstances. Small-telescope SLODAR, while ideal for site monitoring, tends to suffer from a shortage of sufficiently bright binary targets. The SLOTDAR technique may be an ideal replacement as it would continue to operate, with reduced resolution, at times when bright targets were unavailable.

Bibliography

Abahamid, A., Jabiri, A., Vernin, J., Benkhaldoun, Z., Azouit, M., and Agabi, A. (2004a). Optical turbulence modeling in the boundary layer and free atmosphere using instrumented meteorological balloons. *Astron. Astrophys.*, 416:1193–1200.

Abahamid, A., Vernin, J., Benkhaldoun, Z., Jabiri, A., Azouit, M., and Agabi, A. (2004b). Seeing, outer scale of optical turbulence, and coherence outer scale at different astronomical sites using instruments on meteorological balloons. *Astron. Astrophys.*, 422:1123–1127.

Andersen, D. R., Stoesz, J., Morris, S., Lloyd-Hart, M., Crampton, D., Butterley, T., Ellerbroek, B., Jolissaint, L., Milton, N. M., Myers, R., Szeto, K., Tokovinin, A., Véran, J.-P., and Wilson, R. (2006). Performance Modeling of a Wide-Field Ground-Layer Adaptive Optics System. *PASP*, 118:1574–1590.

Angel, R. (2001). Dynamic Refocus for Rayleigh Beacons. In *Science with the Large Binocular Telescope*, pages 21–+.

Assémat, F. (2004). *Apport de la haute résolution angulaire sur l'étude des galaxies lointaines: imagerie, optique adaptative et spectroscopie 3D.* PhD thesis, Observatoire de Paris.

Avila, R. and Chun, M. R. (2004). A method for high-resolution C_N^2 profiling in the first few hundred meters. In *Advancements in Adaptive Optics. Edited by Domenico B. Calia, Brent L. Ellerbroek, and Roberto Ragazzoni. Proceedings of the SPIE, Volume 5490, pp. 742-748 (2004).*

Azouit, M., Borgnino, J., and Vernin, J. (1978). Use of a linear photodiode array in order to estimate in real time the contribution of the lower atmospheric layers in astronomical-image degradation. *Journal of Optics*, 9:291–299.

Baharav, Y., Ribak, E. N., and Shamir, J. (1994). Atmospheric tomography using a fringe pattern in the sodium layer. *Optics Letters*, 19:242–244.

Baharav, Y., Ribak, E. N., and Shamir, J. (1996). Wide-field analysis of turbulence layers using fringes in the mesosphere. *J. Opt. Soc. Am. A*, 13:1083–1093.

Bally, J., Theil, D., Billawalla, Y., Potter, D., Loewenstein, R. F., Mrozek, F., and Lloyd, J. P. (1996). A Hartmann differential image motion monitor (H-DIMM) for atmospheric turbulence characterisation. *Publications of the Astronomical Society of Australia*, 13:22–27.

Baranec, C. J., Bauman, B. J., and Lloyd-Hart, M. (2005). Concept for a laser guide beacon Shack-Hartmann wave-front sensor with dynamically steered subapertures. *Optics Letters*, 30:693–695.

Basden, A. G., Assémat, F., Butterley, T., Geng, D., Saunter, C. D., and Wilson, R. W. (2005). Acceleration of adaptive optics simulations using programmable logic. *Mon. Not. R. Astron. Soc.*, 364:1413–1418.

Basden, A. G., Haniff, C. A., and Mackay, C. D. (2003). Photon counting strategies with low-light-level CCDs. *Mon. Not. R. Astron. Soc.*, 345:985–991.

Beckers, J. M. (1988). Increasing the Size of the Isoplanatic Patch with Multiconjugate Adaptive Optics. In *Very Large Telescopes and their Instrumentation, ESO Conference and Workshop Proceedings, Proceedings of a ESO Conference on Very Large Telescopes and their Instrumentation, held in Garching, March 21-24, 1988, Garching: European Southern Observatory (ESO), 1988, edited by Marie-Helene Ulrich., p.693.*

Benn, C. R., Blanken, M., Bevil, C., Els, S., Goodsell, S., Gregory, T., Jolley, P., Longmore, A. J., Martin, O., Myers, R. M., Ostensen, R., Rees, S., Rutten, R. G. M., Soechting, I., Talbot, G., and Tulloch, S. M. (2004). NAOMI: adaptive optics at the WHT. In *Advancements in Adaptive Optics. Edited by Domenico B. Calia, Brent L. Ellerbroek, and Roberto Ragazzoni. Proceedings of the SPIE, Volume 5490, pp. 79-89 (2004).*

Beran, M. J. and Whitman, A. M. (1988). Scintillation index calculations using an altitude-dependent structure constant. *Applied Optics*, 27:2178–2182.

Bonaccini Calia, D., Myers, R. M., Zappa, F., Love, G. D., Morris, T. J., Hackenberg, W. K. P., Wilson, R. W., and Buscher, D. F. (2004). Cone-effect-free adaptive optics laser guide star development for the ELTs. In *Advancements in Adaptive Optics. Edited by Domenico B. Calia, Brent L. Ellerbroek, and Roberto Ragazzoni. Proceedings of the SPIE, Volume 5490, pp. 1315-1326 (2004).*

Boreman, G. D. and Dainty, C. (1996). Zernike expansions for non-Kolmogorov turbulence. *J. Opt. Soc. Am. A*, 13:517–522.

Buscher, D. F., Love, G. D., and Myers, R. M. (2002). Laser beacon wave-front sensing without focal anisoplanatism. *Optics Letters*, 27:149–151.

Butterley, T., Love, G. D., Wilson, R. W., Myers, R. M., and Morris, T. J. (2006a). A Shack-Hartmann wavefront sensor projected onto the sky with reduced focal anisoplanatism. *Mon. Not. R. Astron. Soc.*, 368:837–843.

Butterley, T., Wilson, R. W., and Sarazin, M. (2006b). Determination of the profile of atmospheric optical turbulence strength from SLODAR data. *Mon. Not. R. Astron. Soc.*, 369:835–845.

Churnside, J. H., Tavis, M. T., Yura, H. T., and Tyler, G. A. (1985). Zernike-polynomial expansion of turbulence-induced centroid anisoplanatism. *Optics Letters*, 10:258–260.

Conan, R., Borgnino, J., Ziad, A., and Martin, F. (2000). Analytical solution for the covariance and for the decorrelation time of the angle of arrival of a wave front corrugated by atmospheric turbulence. *J. Opt. Soc. Am. A*, 17:1807–1818.

Conan, R., Laurent, M. M., Fusco, T., Michau, V., and Rousset, G. (1998). Myopic deconvolution of adaptive optics images by use of object and point-spread function power spectra. *Applied Optics*, 37:4614–4622.

Crescenti, G. H. (1997). A Look Back on Two Decades of Doppler Sodar Comparison Studies. *Bulletin of the American Meteorological Society, vol. 78, Issue 4, pp.651-651*, 78:651–651.

Cubalchini, R. (1979). Modal wave-front estimation from phase derivative measurements. *J. Opt. Soc. Am.*, 69:972–977.

Dainty, J. C. (2000). Optical effects of atmospheric turbulence. In Ageorges, N. and Dainty, C., editors, *Laser Guide Star Adaptive Optics for Astronomy. Kluwer Academic Publishers (Dordrecht), 2000.*

Ellerbroek, B. L. and Cochran, G. M. (2002). A wave optics propagation code for multi-conjugate adaptive optics. In *Adaptive Optics and Technology II. Edited by Robert K. Tyson, Domenico Bonaccini, Michael Roggemann. Proceedings of the SPIE*, volume 4494, pages 104–120.

Flicker, F. C. and Rigaut, F. J. (2005). Anisoplanatic deconvolution of adaptive optics images. *J. Opt. Soc. Am. A*, 22:504–513.

Foy, R. and Labeyrie, A. (1985). Feasibility of adaptive telescope with laser probe. *Astron. Astrophys.*, 152:L29–L31.

Fried, D. L. (1965). Statistics of a Geometric Representation of Wavefront Distortion. *J. Opt. Soc. Am.*, 55:1427–1435.

Fuchs, A., Tallon, M., and Vernin, J. (1998). Focusing on a Turbulent Layer: Principle of the "Generalized SCIDAR". *PASP*, 110:86–91.

Fusco, T., Conan, J.-M., Mugnier, L. M., Michau, V., and Rousset, G. (2000). Characterization of adaptive optics point spread function for anisoplanatic imaging. Application to stellar field deconvolution. *Astron. Astrophys. Suppl. Ser.*, 142:149–156.

Garnier, D., Coburn, D., and Dainty, J. C. (2005). Single star SCIDAR for $C_n^2(h)$ profiling. In *Atmospheric Optical Modeling, Measurement, and Simulation. Edited by Doss-Hammel, Stephen M.; Kohnle, Anton. Proceedings of the SPIE, Volume 5891, pp. 20-26 (2005).*

Goodman, J. W. (1985). *Statistical Optics.* John Wiley & Sons, New York.

Hardy, J. W. (1998). *Adaptive Optics for Astronomical Telescopes.* Oxford University Press, New York, NY, USA.

Hecht, E. (2002). *Optics (4th Edition).* Addison Wesley, San Francisco.

Herriot, G., Morris, S., Roberts, S., Fletcher, J. M., Saddlemyer, L. K., Singh, G., Veran, J.-P., and Richardson, E. H. (1998). Innovations in Gemini adaptive optics system design. In *Proc. SPIE Vol. 3353, p. 488-499, Adaptive Optical System Technologies, Domenico Bonaccini; Robert K. Tyson; Eds.*

Jenkins, C. R. (1998). Fast guiding and small telescopes in the 8-m era. *Mon. Not. R. Astron. Soc.*, 294:69–92.

Kellner, S., Ragazzoni, R., Gässler, W., Diolaiti, E., Farinato, J., Arcidiacono, C., Myers, R. M., Morris, T. J., and Ghedina, A. (2004a). PIGS on sky - dream or reality? In *Emerging Optoelectronic Applications. Edited by Jabbour, Ghassan E.; Rantala, Juha T. Proceedings of the SPIE, Volume 5382, pp. 520-525 (2004).*

Kellner, S., Ragazzoni, R., Gässler, W., Diolaiti, E., Morris, T. J., Saunter, C. D., Meyers, R., Farinato, J., Arcidiacono, C., and Ghedina, A. (2004b). PIGS: first results on sky. In *Advancements in Adaptive Optics. Edited by Domenico B. Calia, Brent L. Ellerbroek, and Roberto Ragazzoni. Proceedings of the SPIE, Volume 5490, pp. 989-997 (2004).*

Klückers, V. A., Wooder, N. J., Nicholls, T. W., Adcock, M. J., Munro, I., and Dainty, J. C. (1998). Profiling of atmospheric turbulence strength and velocity using a generalised SCIDAR technique. *Astron. Astrophys. Suppl. Ser.*, 130:141–155.

Kolmogorov, A. N. (1941). Dissipation of Energy in the Locally Isotropic Turbulence. *Reprinted in Royal Society of London Proceedings Series A (1991)*, 434:15–17.

Lawrence, G. N. (1992). Optical Modeling. *Applied Optics and Optical Engineering*, 11:125–200.

Lawrence, J. S., Ashley, M. C. B., Tokovinin, A., and Travouillon, T. (2004). Exceptional astronomical seeing conditions above Dome C in Antarctica. *Nature*, 431:278–281.

Le Louarn, M. (2002). Multi-Conjugate Adaptive Optics with laser guide stars: performance in the infrared and visible. *Mon. Not. R. Astron. Soc.*, 334:865–874.

Le Louarn, M., Hubin, N., Sarazin, M., and Tokovinin, A. (2000). New challenges for adaptive optics: extremely large telescopes. *Mon. Not. R. Astron. Soc.*, 317:535–544.

Love, G. D., Myers, R. M., Wilson, R. W., Buscher, D. F., Butterley, T., and Morris, T. J. (2004). Sensing the atmosphere on the upward path: LGSs without focal anisoplanatism for ELTs. In *Emerging Optoelectronic Applications. Edited by Jabbour, Ghassan E.; Rantala, Juha T. Proceedings of the SPIE, Volume 5382, pp. 462-467 (2004).*

Maire, J., Ziad, A., Borgnino, J., Martin, F., Jankov, S., Bonneau, D., and Patru, F. (2006). Wavefront outer scale deduced from interferometric dispersed fringes. *Astron. Astrophys.*, 448:1225–1234.

Marchetti, E., Brast, R., Delabre, B., Donaldson, R., Fedrigo, E., Frank, C., Hubin, N. N., Kolb, J., Le Louarn, M., Lizon, J.-L., Oberti, S., Reiss, R., Santos, J., Tordo, S., Ragazzoni, R., Arcidiacono, C., Baruffolo, A., Diolaiti, E., Farinato, J., and Vernet-Viard, E. (2004). MAD status report. In *Advancements in Adaptive Optics. Edited by Domenico B. Calia, Brent L. Ellerbroek, and Roberto Ragazzoni. Proceedings of the SPIE, Volume 5490, pp. 236-247 (2004).*

Marchetti, E., Hubin, N. N., Fedrigo, E., Brynnel, J., Delabre, B., Donaldson, R., Franza, F., Conan, R., Le Louarn, M., Cavadore, C., Balestra, A., Baade, D., Lizon, J.-L., Gilmozzi, R., Monnet, G. J., Ragazzoni, R., Arcidiacono, C., Baruffolo, A., Diolaiti, E., Farinato, J., Vernet-Viard, E., Butler, D. J., Hippler, S., and Amorin, A. (2003). MAD the ESO multi-conjugate adaptive optics demonstrator. In *Adaptive Optical System Technologies II. Edited by Wizinowich, Peter L.; Bonaccini, Domenico. Proceedings of the SPIE, Volume 4839, pp. 317-328 (2003).*

Martin, F., Tokovinin, A., Ziad, A., Conan, R., Borgnino, J., Avila, R., Agabi, A., and Sarazin, M. (1998). First statistical data on wavefront outer scale at La Silla observatory from the GSM instrument. *Astron. Astrophys.*, 336:L49–L52.

McCullough, P. R., Foy, R., Boucher, Y., Fleury, B., Grynberg, G., Migus, A., and Tallon, M. (1992). Tilt Sensing using a Multi-color Laser Beacon. In *Bulletin of the American Astronomical Society*, pages 1219–+.

Morris, T. J. and Myers, R. M. (2006). Wide-field Adaptive Optics correction using a single rotating laser guide star. *Mon. Not. R. Astron. Soc.*, 370:1783–1789.

Mrochen, M., Kaemmerer, M., Mierdel, P., Krinke, H. E., and Seiler, T. (2001). Principles of Tscherning aberrometry. *Journal of Refractive Surgery*, 16:S570–S71.

Nicholls, T. W., Boreman, G. D., and Dainty, J. C. (1995). Use of a Shack-Hartmann wave-front sensor to measure deviations from a Kolmogorov phase spectrum. *Optics Letters*, 20:2460–2463.

Noll, R. J. (1976). Zernike polynomials and atmospheric turbulence. *J. Opt. Soc. Am.*, 66:207–211.

Parenti, R. R. and Sasiela, R. J. (1994). Laser guide-star systems for astronomical applications. *J. Opt. Soc. Am. A*, 11:288–309.

Rao, C., Jiang, W., and Ling, N. (2000). Spatial and temporal characterization of phase fluctuations in non-Kolmogorov atmospheric turbulence. *Journal of Modern Optics*, 47:1111–1126.

Rao, C., Jiang, W., and Ling, N. (2002). Atmospheric characterization with Shack-Hartmann wavefront sensors for non-Kolmogorov turbulence. *Opt. Eng.*, 41:534–541.

Ribak, E. N. and Ragazzoni, R. (2004). Reduction of laser spot elongation in adaptive optics. *Optics Letters*, 29:1351–1353.

Rigaut, F. (2002). Ground-Conjugate Wide Field Adaptive Optics for the ELTs. In *Beyond conventional adaptive optics: a conference devoted to the development of adaptive optics for extremely large telescopes. Proceedings of the Topical Meeting held May 7-10, 2001, Venice, Italy. Edited by E. Vernet, R. Ragazzoni, S. Esposito, and N. Hubin. Garching, Germany: European Southern Observatory, 2002 ESO Conference and Workshop Proceedings, Vol. 58, ISBN 3923524617, p. 281.*

Roggeman, M. and Welsh, B. (1996). *Imaging Through Turbulence.* CRC Press, Boca Raton.

Sandler, D. G., Cuellar, L., Lefebvre, M., Barrett, T., Arnold, R., Johnson, P., Rego, A., Smith, G., Taylor, G., and Spivey, B. (1994). Shearing interferometry for laser-guide-star atmospheric correction at large D/r_0. *J. Opt. Soc. Am. A*, 11:858–873.

Sarazin, M., Butterley, T., Tokovinin, A., Travouillon, T., and Wilson, R. W. (2005). The Tololo SLODAR Campaign, unpublished report.

Sarazin, M. and Roddier, F. (1990). The ESO differential image motion monitor. *Astron. Astrophys.*, 227:294–300.

Schöck, M., Erasmus, D. A., Djorgovski, S. G., Chanan, G. A., and Nelson, J. E. (2003). CELT site testing program. In *Future Giant Telescopes. Edited by Angel, J. Roger P.; Gilmozzi, Roberto. Proceedings of the SPIE, Volume 4840, pp. 541-552 (2003).*

Southwell, W. H. (1980). Wave-front estimation from wave-front slope measurements. *J. Opt. Soc. Am.*, 70:998–1006.

St-Jacques, D., Cox, G. C., Baldwin, J. E., Mackay, C. D., Waldram, E. M., and Wilson, R. W. (1997). The JOSE atmospheric seeing monitor at the William Herschel Telescope. *Mon. Not. R. Astron. Soc.*, 290:66–74.

Stock, J. and Keller, G. (1960). *Astronomical Seeing*, pages 138–+. Telescopes. Stars and Stellar Systems. Edited by Gerard P. Kuiper and Barbara M. Middlehurst. Published by the University of Chicago Press, Chicago IL USA, 1960, 1960, 1969.

Szeto, K., Andersen, D., Crampton, D., Morris, S., Lloyd-Hart, M., Myers, R., Jensen, J. B., Fletcher, M., Gardhouse, W. R., Milton, N. M., Pazder, J., Stoesz, J., Simons, D., and Véran, J.-P. (2006). A proposed implementation of a ground layer adaptive optics system on the Gemini Telescope. In *Ground-based and Airborne Instrumentation for Astronomy. Edited by McLean, Ian S.; Iye, Masanori. Proceedings of the SPIE, Volume 6269, (2006).*

Tallon, M., Foy, R., and Vermin, J. (1992). 3-D Wavefront Sensing for Multi-conjugate Adaptive Optics. In Ulrich, M.-H., editor, *Progress in Telescope and Instrumentation Technologies*, pages 517–+.

Tatarski, V. (1961). *Wave propagation in a turbulent medium.* McGraw-Hill, New York.

Thiébaut, E. and Conan, J.-M. (1995). Strict *a priori* constraints for maximum-likelihood blind deconvolution. *J. Opt. Soc. Am. A*, 12:485–492.

Tokovinin, A. (1998). A new method of measuring atmospheric seeing. *Astronomy Letters*, 24:662–664.

Tokovinin, A. (2002). From Differential Image Motion to Seeing. *PASP*, 114:1156–1166.

Tokovinin, A. (2004). Seeing Improvement with Ground-Layer Adaptive Optics. *PASP*, 116:941–951.

Travouillon, T. (2006). SODAR calibration for turbulence profiling in TMT site testing. In *Ground-based and Airborne Telescopes. Edited by Stepp, Larry M.. Proceedings of the SPIE, Volume 6267, pp. (2006).*

Tscherning, M. (1894). Die monochromatischen Aberrationen des menshlichen Auges. *Ztschr f Psychol u Physiol d Sinnesorg*, 6:456–71.

Vernin, J. and Muñoz-Tuñón, C. (1992). Optical seeing at La Palma Observatory. I. General guidelines and preliminary results at the Nordic Optical Telescope. *Astron. Astrophys.*, 257:811–816.

Vernin, J. and Muñoz-Tuñón, C. (1994). Optical seeing at La Palma Observatory. II. Intensive site testing campaign at the Nordic Optical Telescope. *Astron. Astrophys.*, 284:311–318.

von Kármàn, T. (1948). Progress in the Statistical Theory of Turbulence. *Proc Natl Acad Sci*, 34:530–539.

Welsh, B. M. (1992). Sensing refractive-turbulence profiles (C_n^2) using wave front phase measurements from multiple reference sources. *Applied Optics*, 31:7283–7291.

Wilson, R. and Saunter, C. (2003). SLODAR: Profiling Atmospheric Turbulence at the WHT. *The Newsletter of the Isaac Newton Group of Telescopes (ING Newsl.), issue no. 7, p. 19.*, 7:19–+.

Wilson, R. W. (2002). SLODAR: measuring optical turbulence altitude with a Shack-Hartmann wavefront sensor. *Mon. Not. R. Astron. Soc.*, 337:103–108.

Wilson, R. W. (2005). Private communication.

Wilson, R. W., Bate, J., Guerra, J. C., Hubin, N. N., Sarazin, M., and Saunter, C. D. (2004a). Development of a portable SLODAR turbulence profiler. In *Advancements in Adaptive Optics. Edited by Domenico B. Calia, Brent L. Ellerbroek, and Roberto Ragazzoni. Proceedings of the SPIE, Volume 5490, pp. 758-765 (2004).*

Wilson, R. W. and Jenkins, C. R. (1996). Adaptive optics for astronomy: theoretical performance and limitations. *Mon. Not. R. Astron. Soc.*, 278:39–61.

Wilson, R. W., O'Mahony, N., Packham, C., and Azzaro, M. (1999). The seeing at the William Herschel Telescope. *Mon. Not. R. Astron. Soc.*, 309:379–387.

Wilson, R. W., Saunter, C. D., and Guerra, J. C. (2004b). SLODAR turbulence characterization for ELTs. In *Second Backaskog Workshop on Extremely Large Telescopes. Edited by Ardeberg, Arne L.; Andersen, Torben. Proceedings of the SPIE, Volume 5382, pp. 661-667 (2004).*

Wilson, R. W., Wooder, N. J., Rigal, F., and Dainty, J. C. (2003). Estimation of anisoplanatism in adaptive optics by generalized SCIDAR profiling. *Mon. Not. R. Astron. Soc.*, 339:491–494.

Winker, D. M. (1991). Effect of a finite outer scale on the Zernike decomposition of atmospheric optical turbulence. *J. Opt. Soc. Am. A*, 8:1568–1573.

Yura, H. T. and Tavis, M. T. (1985). Centroid anisoplanatism. *J. Opt. Soc. Am. A*, 2:765–773.

Ziad, A., Borgnino, J., Martin, F., Maire, J., and Mourard, D. (2004). Towards the monitoring of atmospheric turbulence model. *Astron. Astrophys.*, 414:L33–L36.